DEVELOPMENT OF NANOMATERIAL BASED SENSORS FOR THE DETECTION OF EXPLOSIVES

WILLIAM J. R. PEVELER

University College London

Department of Security and Crime Science

A thesis submitted in partial fulfilment of the requirements for the degree of Doctor of Philosophy, 2015

DECLARATION

I, William J. R. Peveler, declare that this thesis is my own original work and that all source material used has been clearly identified and acknowledged.

Word Count: 32789 including captions, excluding front matter and appendices.

William J. R. Peveler
October 7, 2015

ABSTRACT

Detection of low levels of illicit materials, such as explosives, is a key challenge for security and environmental monitoring. Recent advances in highly sensitive molecular-recognition techniques utilising nanomaterials may provide a wealth of useful tools for this purpose.

In this thesis two classes of nanomaterials are applied to explosives sensing. The first is a range of novel gold nanoparticles, produced *via* the facile reduction of chloroauric acid with mono- and di-ketones. The mechanism of this reaction and the resultant particles are characterised with spectroscopy and tunnelling electron microscopy. Several different sizes of gold colloid were created, but most interesting was the creation of gold nanostars, which have potential as a substrate for surface-enhanced Raman spectroscopy.

The second nanomaterial-based sensor is a quantum dot array featuring supramolecular receptors for small-molecule explosive detection. By combining array elements into a single, multichannel platform; faster results can be obtained from smaller amounts of sample. The ability of quantum dots to act as luminescent probes in a multichannel array, due to their sharp, variable emissions from a single excitation wavelength, was exploited to detect five explosives - 2,4-dinitrotoluene (DNT), 2,4,6-trinitrotoluene (TNT), tetryl (2,4,6-trinitrophenylmethylnitramine), cyclotrimethylenetrinitramine (RDX) and pentaerythritol tetranitrate (PETN). To create the array, each different colour quantum dot was functionalised with a different cavitand, aromatic or nucleophilic-heteroatom based receptor *via* a facile photoligation process. These receptors undergo supramolecular interactions with the explosives, inducing variable fluorescence quenching of the quantum dots. Pattern analysis of the fluorescence quenching data allowed for explosive detection and identification with limits-of-detection of < 1 part-per-million.

Finally, the development of the quantum dot based sensors from solution phase to solid phase is examined, with the aim of creating point-of-test devices for use in the field. A key outcome was the development of supramolecular organogel/nanoparticle hybrid "smart" materials for sensing applications.

" . . . Such developments in molecular and supramolecular design and engineering open perspectives towards the realization of molecular photonic, electronic, and ionic devices that would perform highly selective recognition, reaction, and transfer operations for signal and information processing at the molecular level."

— Jean-Marie Lehn.[1]

ACKNOWLEDGMENTS

There are many people I must acknowledge and thank for their help and contribution to this thesis. Most importantly, Professor Ivan Parkin and Dr Ruth Morgan for their careful supervision, insightful comments and helpful feedback on the project and thesis. I must also thank Dr Michael Porter for access to lab space and guidance on aspects of the synthetic work, Professor Stephen Hailes for guidance on machine learning tools, and Dr Oren Scherman for hosting me in Cambridge to work on the synthesis of cucurbiturils. Dr Abil Aliev assisted with advanced NMR experiments, such as DOSY spectroscopy, Dr Kersti Karu ran mass spectrometry experiments, Dr Paul Southern provided SQUID measurements, Emily Glover assisted with XPS, and Prof Tony Kenyon provided access to and assistance with fluorescence lifetime analysis. Dr Steve Firth provided expert insight and training on the Raman spectrometer and electron microscopes, as well as useful discussion on many matters from spectroscopy to microscopy. Dr Nathan Hollingsworth and Dr Alberto Roldan assisted with the surface modelling of the quantum dot system, and Dr Joseph Bear generously provided a sample of InP quantum dots for comparative work.

My fellow PhDs have made the last four years a lot of fun. Emma, Ralph, Joe, Nick, Emily, Gwyn, Michael, Monika and Sacha and everyone in Office 320 provided invaluable discussion and a lot of laughs in Chemistry, along with Matt, Reka, Nick and all the SECReT'ers past and present. Thank you for a great time.

Huge personal thanks go to Dr Martin Grossel for starting me down this road, his guidance on both work and life, and his generosity in all things, especially Mahler.

Finally, a massive thanks to my family for their unwavering love and support, without whom I would not have got this far, and to Gemma, for everything.

CONTENTS

1 INTRODUCTION
- 1.1 The need for explosives detection . . . 1
- 1.2 Aim of this work . . . 3
- 1.3 Structure of this thesis . . . 4

2 LITERATURE REVIEW
- 2.1 Explosive materials . . . 5
- 2.2 Sensing . . . 6
- 2.3 Nanomaterials for sensing . . . 10
- 2.4 Summary . . . 25

3 GOLD NANOPARTICLES
- 3.1 Rationale . . . 27
- 3.2 Gold nanoparticle synthesis . . . 29
- 3.3 AuNP characterisation and discussion . . . 30
- 3.4 SERS sensing . . . 42
- 3.5 Conclusions . . . 45

4 QUANTUM DOT SYNTHESIS
- 4.1 Rationale . . . 47
- 4.2 System synthesis and characterisation . . . 51
- 4.3 Photophysical characterisation and testing . . . 63
- 4.4 Conclusions . . . 72

5 EXPLOSIVES SENSING
- 5.1 Rationale . . . 75
- 5.2 Solution sensing protocol . . . 80
- 5.3 Results and Discussion . . . 82
- 5.4 Conclusions . . . 93

6 SENSOR IMMOBILISATION
- 6.1 Rationale . . . 95
- 6.2 Paper test strips . . . 96
- 6.3 Supramolecular gel vehicle . . . 97
- 6.4 Conclusions . . . 103

7 CONCLUSIONS AND FUTURE WORK
- 7.1 Conclusions . . . 105
- 7.2 Future work . . . 107

8 MATERIALS AND METHODS
- 8.1 General methods and materials . . . 109
- 8.2 Characterisation table . . . 111
- 8.3 Nanoparticle ligand syntheses . . . 113
- 8.4 Gelator synthesis . . . 134
- 8.5 Nanoparticle syntheses . . . 134

BIBLIOGRAPHY 141

APPENDIX

A PUBLISHED PAPERS 161

B COMPUTATIONAL DETAILS 163

LIST OF FIGURES

Figure 1.1 Examples of explosive analytes . . . 1
Figure 2.1 Scheme of a sensor system . . . 7
Figure 2.2 Schematic of 0D - 3D nanomaterials . . . 10
Figure 2.3 LaMer model of particle growth . . . 12
Figure 2.4 Surface ligands for nanoparticles . . . 13
Figure 2.5 Raman mode schematic . . . 18
Figure 2.6 Band alteration in a quantum dot . . . 20
Figure 2.7 Relationship between quantum dot size and bandgap 22
Figure 2.8 Jablonski diagram including photoinduced electron transfer . . . 23
Figure 3.1 Representative TEM micrographs of standard AuNPs 28
Figure 3.2 Ketones applied in AuNP synthesis . . . 30
Figure 3.3 Images of AuNP reactions from six ketones . . . 31
Figure 3.4 UVVis monitoring of cyclopentanone and cycloheptanone AuNP reactions . . . 32
Figure 3.5 UVVis monitoring of 1,3 and 1,4 cyclohexanedione in chloroauric acid . . . 33
Figure 3.6 UVVis spectra from each ketone generated AuNP . . 34
Figure 3.7 TEM micrographs of AuNPs from cyclopentanone . . 35
Figure 3.8 TEM micrographs of AuNPs from cycloheptanone . . 35
Figure 3.9 TEM micrographs of AuNPs from 1,3 and 1,4-cyclohexanedione . . . 36
Figure 3.10 XPS spectra from AuNPs synthesised with various ketones . . . 38
Figure 3.11 IR spectra for a range of AuNPs produced with different ketones . . . 39
Figure 3.12 Relationship between reaction time and ketone pK_E . 41
Figure 3.13 TEM micrograph of gold nanostar tips . . . 43
Figure 3.14 Attempted SERS with gold nanostars . . . 44
Figure 4.1 Cavitand structures and shapes . . . 48
Figure 4.2 Mass spectrum of attempted synthesis of fCB[6] . . . 57
Figure 4.3 HMBC NMR of the attempted coupling of a dopamine based receptor . . . 59
Figure 4.4 UV illumination of QD samples . . . 60
Figure 4.5 TEM, EDX and spectrscopy of the QDs . . . 64
Figure 4.6 Absorption, emission and excitation spectra for **OMe**$_{544}$ and the original TOPO capped QDs. . . . 65
Figure 4.7 Stretched exponential fluorescence decays for three TOPO capped QDs . . . 67
Figure 4.8 Comparison of quenching with PEG and TEG functionalised quantum dots . . . 71
Figure 4.9 Comparison of InP and CdSe quantum dots . . . 72
Figure 5.1 Explosives used in array study . . . 75
Figure 5.2 Approximate quantum dot and explosive band energies 76
Figure 5.3 Non-specific array-based sensing . . . 77
Figure 5.4 Results of single channel sensing with 7 red, green and blue QDs . . . 83
Figure 5.5 Modelling quantum dot surface interactions . . . 85
Figure 5.6 Molecules in position on a ZnS surface . . . 87
Figure 5.7 Canonical plot for LDA analysis of the single channel Stern-Volmer data . . . 88

Figure 5.8 Results of multichannel sensing . . . 90
Figure 5.9 Canonical plot for LDA analysis of multichannel Stern-Volmer data . . . 91
Figure 5.10 Effect of contaminants on the quantum dot array . . 93
Figure 6.1 Quantum dot test strips for explosive detection by eye 97
Figure 6.2 Nanoparticulate containing gels . . . 99
Figure 6.3 TEM of nanoparticle gels . . . 99
Figure 6.4 Further TEM of nanoparticle gels . . . 100
Figure 6.5 Functional properties of nanoparticle gels . . . 102
Figure 6.6 Recovery of nanoparticles from the gel . . . 103
Figure 8.1 Histograms of measured QD size by TEM . . . 136

LIST OF TABLES

Table 2.1 Some vapour pressures of explosives and related materials . . . 5
Table 3.1 Summary of AuNP and ketone properties . . . 40
Table 4.1 Cavitand and analyte dimensions . . . 50
Table 4.2 Double exponential fluorescence lifetime fit of TOPO capped QDs . . . 66
Table 4.3 Stretched exponential fluorescence lifetime fit of TOPO capped QDs . . . 68
Table 4.4 Stretched exponential fluorescence lifetime fit for functionalised QDs . . . 68
Table 4.5 Triple exponential fluorescence lifetime fit for functionalised QDs . . . 69
Table 4.6 Quantum yield results for several quantum dot samples 70
Table 5.1 Conversion table of ppm and molar values . . . 81
Table 5.2 LOD values for single channel array elements . . . 82
Table 5.3 Summary of ab initio parameters . . . 85
Table 5.4 Confusion matricies for single channel SVM analysis 89
Table 5.5 LOD values for multichannel array wavelengths . . . 90
Table 5.6 Confusion matricies for mutilchannel SVM analysis . 91
Table 5.7 Jacknifed analysis on the multichannel array . . . 92
Table 8.1 Characterisation table . . . 112
Table B.1 Summary of computed bulk material properties . . . 164

LIST OF SCHEMES

Scheme 2.1 A Meisenheimer complex . . . 14
Scheme 3.1 Generic reaction mechanism for AuNP formation . . 41
Scheme 4.1 Scheme of ligand design . . . 51
Scheme 4.2 Synthesis of functional PEGs . . . 52
Scheme 4.3 Synthesis of functional TEGs . . . 53
Scheme 4.4 Synthesis of monopropargyl calix[4]arene . . . 54
Scheme 4.5 Synthesis of monopropargyl cyclodextrin . . . 55
Scheme 4.6 Synthesis of cucurbituril derivatives . . . 56
Scheme 4.7 Synthesis of dopamine derivatives . . . 58
Scheme 4.8 Synthesis of propargyl naphthalene . . . 60
Scheme 4.9 Click coupling scheme . . . 62
Scheme 6.1 Scheme of gelator synthesis . . . 98

ACRONYMS

AN	ammonium nitrate
ANN	artificial neural network
AuNP	gold nanoparticle
DCC	N,N′-dicyclohexyl-carbodiimide
DDT	dodecanethiol
DMDNB	2,3-dimethyl-2,3-dinitrobutane
DMAP	4-dimethylaminopyridine
DMF	dimethylformamide
DNT	dinitrotoulene
EDX	energy-dispersive X-ray spectroscopy
HMTD	hexamethylene triperoxide diamine
HOMO	highest occupied molecular orbital
IED	improvised explosive device
IMS	ion mobility spectrometry
IR	infrared spectroscopy
LA	lipoic acid
LDA	linear discriminant analysis
LMWO	low molecular weight organogelator
LUMO	lowest unoccupied molecular orbital
MeOH	methanol
MOF	metal organic framework
MS	mass spectrometry
MIP	molecularly imprinted polymer
MWCNT	multiwall carbon nanotube
NP	nanoparticle
ODE	octadec-1-ene
PCA	principal component analysis
PEG	polyethylene glycol
PET	photoinduced electron transfer
PETN	pentaerythritol tetranitrate
ppb	parts per billion
ppm	parts per million
ppt	parts per trillion
QD	quantum dot
RDX	research department explosive
RT	room temperature
SERS	surface-enhanced Raman spectroscopy
SPR	surface plasmon resonance
SVM	support vector machine
TATP	tri-acetone peroxide
TCSPC	time-correlated single photon counting
TEG	triethylene glycol
TEM	transmission electron microscopy
TNT	trinitrotoluene
TOAB	tetraoctylammonium bromide
TOP	trioctylphosphine
TOPO	trioctylphosphine oxide
UVVis	UV-visible absorption spectroscopy
VOC	volatile organic compound
XPS	X-ray photoelectron spectroscopy

1

INTRODUCTION

1.1 THE NEED FOR EXPLOSIVES DETECTION

In the field of security science, a major research theme is development of technology for threat detection. It is desirable to have the capability to detect illicit materials in a whole range of scenarios, but these materials are often in low concentrations, hidden, or masked to avoid detection, and thus there is a 'detection challenge'.[2–4]

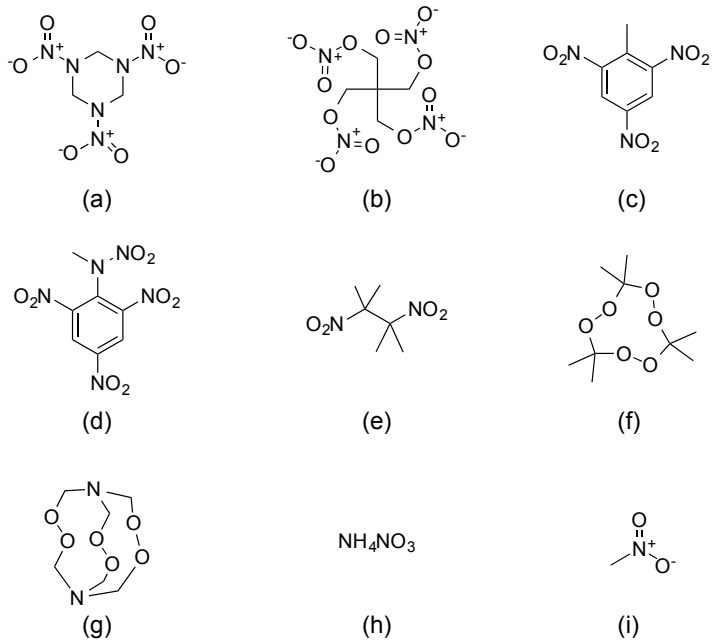

Figure 1.1: *Examples of explosive analytes: (a) RDX (b) PETN (c) TNT (d) tetryl (e) DMDNB (f) TATP (g) HMTD (h) AN (i) nitromethane. (a)-(d) are examples of nitro-high explosives. (e) is a commonly used taggant for high explosives. (f) and (g) are examples of home-made peroxide explosives. (h) is an inorganic industrial blasting explosive and (i) is a fuel commonly added to make IEDs from AN.*

Focussing on the example of explosives detection; it is necessary to be able to reliably detect several kinds of explosive material, such as those in Fig. 1.1, at low concentrations, in many different environments. The explosive that needs detecting might be an improvised explosive device (IED) in the Iraqi

desert, consisting of several kinds of home-made and military grade explosives such as research department explosive (RDX) or tri-acetone peroxide (TATP). Alternatively, it might be a truck bomb, constructed from industrial mining explosives (e.g Oklahoma 1995 used ammonium nitrate (AN) and nitromethane), or the military might simply want to measure the environmental presence of pollutant high-explosives, such as trinitrotoluene (TNT), in soil and ground water on testing ranges.[5]

1.1.1 *Securing against an explosive attack*

The most obvious reason to detect explosives is to prevent an undesirable explosion at a vulnerable location, for example a military convoy or civilian travel hub. Such targets may be attacked with a static explosive device, such as an IED, or a suicide device carried on a person. As an example of the scale of the challenge, in the period 2007-2013, IEDs were consistently responsible for over 40% (1401 in total) of coalition deaths in Operation Enduring Freedom, Afghanistan, with a peak in 2009 of 61%.[6]

The standard way to screen against such attacks on a target is with the use of explosive sniffer dogs, or in more recent years, hand held machines that screen for (sniff out) explosives. Other techniques include x-ray monitoring of baggage or packages. However no one system is robust by itself, so they are best applied in conjunction.

In the case of securing these targets, explosives might need to be detected on a range of materials via swabbing surfaces, or in the air (the vapour phase). The explosive material itself will be concealed, so very small amounts of residue will need to be detected.

1.1.2 *Environmental monitoring*

A second area where the detection of explosives is needed is in the broader environment. This can be used to prevent a terrorist attack before the bomb is even completed, by monitoring explosives in the air, or in particular in waste water and sewage in towns and cities, to discover bomb factories.[7]

An example is the holistic approach taken in Sweden, deploying a network of sensors in the sewers to detect and localise threats early (The FP7 funded EMPHASIS project).[8]

Environmental monitoring of explosives is also valuable because of their toxic and polluting nature.[9] Explosives can enter the environment through manufacturing waste from munitions factories, through dumped surplus munitions and through abandoned arms, such as unexploded ordnance or land mines on test ranges or in conflict zones.[10] This places highly toxic high explosives such as TNT or RDX in to the natural environment, leading to the loss of plant and animal life as well as contamination of drinking water. To combat this, soils and water from at-risk sites are tested to quantify how much explosive remains in the environment, and how rapidly it is being degraded or removed.[11, 12] For example, the US Environmental Protection Agency set stringent controls on the amount of explosive that can be present in drinking water, $< 0.1\ \mu g/mL$ of dinitrotoulene (DNT), TNT or RDX.[13]

1.2 AIM OF THIS WORK

The aim of this project is to develop new materials for explosives detection based on nanotechnology. On the basis of the two cases above, the aim is to create a simple, reliable and low cost detection method for a range of explosive analytes with two key traits: high *sensitivity* and *specificity*. It must be able to detect low concentrations of the analyte, and it must differentiate between the analyte and other materials present. In addition it would be useful if the test is easily re-configurable for emerging new analytes. It must be considered whether the sensor is designed to detect water-borne explosives for more general environmental monitoring, or vapour phase explosives for direct threat detection.

Sensitivity: the probability of a positive result in the presence of the target analyte. Specificity: the probability of a negative result in the absense of analyte

1.3 STRUCTURE OF THIS THESIS

This thesis documents my work on developing nanomaterials for explosive sensing and detection. The first section, Chapter 2, is a broad review of chemical sensing, nanomaterial synthesis, and the role that nanomaterials can play in sensing. Each work chapter then starts with a more focussed short review of the relevant literature. Chapter 3 details initial work that sought to apply a new synthesis of gold nanoparticles to the sensing of explosives with plasmonically enhanced Raman spectroscopy, and discusses the issues encountered. Attention then turns to the development of a quantum-dot based sensor, which is detailed in Chapter 4. The potential to take this solution phase detection system and apply it as a multichannel sensing array is described in Chapter 5, and attempts to immobilise the system and make it applicable to vapour phase chemical detection are discussed in Chapter 6. Finally the conclusions and ideas for future work are discussed in Chapter 7, and the detailed synthetic procedures are presented in Chapter 8.

A complete list of published material is included in Appendix A. Additional information, regarding the computational experiments featured in Chapter 5, is presented in Appendix B.

2

LITERATURE REVIEW

2.1 EXPLOSIVE MATERIALS

Explosives can be broadly split into two categories, conventional or military explosives and improvised explosives. The former category rely on the production of nitrogen to drive their explosive power, so contain nitro or nitrate groups on a carbon skeleton. Examples include TNT, RDX, PETN or AN. The latter category tend to contain peroxides, and can be synthesised from a range of household goods such as nail polish remover (acetone), hair bleach (hydrogen peroxide) and camping fuel (hexamine). Examples are TATP and HMTD. Structures for these examples are given in Fig. 1.1 in Chapter 1.

As discussed in Chapter 1, one way to detect explosives is in the vapour phase. This allows for remote screening of crowded environments, to detect concealed material. However a major impediment to this is the low volatility of many explosives, in particular the conventional nitro-explosives (Table 2.1).

Table 2.1: *Some vapour pressures of explosives and related materials. Data adapted from Marshall & Oxley.[2, p. 24]*

Material	Vapour Pressure (Pa, 25 °C)	Part Volume @ 1 atm
RDX	6.3×10^{-7}	6 ppt
PETN	1.9×10^{-6}	19 ppt
TNT	9.9×10^{-4}	10 ppb
DMDNB	0.28	3 ppm
TATP	5.6	55 ppm
nitromethane	4.9×10^{3}	37×10^{3} ppm

The usual tool employed for the vapour detection is the explosives sniffer dog.[14] These are highly trained dogs capable of detecting certain com-

pounds such as DMDNB, a plastic explosives taggant, at the sub parts per billion (ppb) level, as well as other materials of interest. However, it is very hard to know what the animal is actually detecting. Although they can alert their handler to a threat, the handler cannot tell what that threat might be.[15, 16] In addition, dogs must be extensively trained on samples of the explosives they are to detect, and thus cannot respond to new threats quickly. Dogs also tire rapidly, and can only work for short periods before needing a break.[17]

To counter these issues, much work has gone into the replacement, or at least supplementation, of explosive sniffer dogs with development of machines for sniffing explosives that utilise physicochemical methods for sensing. This work is supported by the development of techniques for the classification and quantification of explosives in water and soils for environmental monitoring purposes.

This chapter will describe the basis of a chemical sensing system, and some existing techniques for explosives detection. The advantages of incorporating nanomaterials into chemical sensors will then be described and some examples discussed.

2.2 SENSING

2.2.1 *A sensor system*

A sensor is a system that gives a measurable response in the presence of a target analyte. Herein a sensor will be defined as a combination of a sampling system, a transducer and a signal processing and output system (Fig. 2.1).

The sampler is a device for taking in an environmental sample and processing it for passing to the transducer. Examples range from the simplest fan to draw air over the sensor, to devices that heat swabs to desorb analytes picked up on their surface, or other solid samples, to liquid injection systems with pre-concentration and chromatographic capabilities.

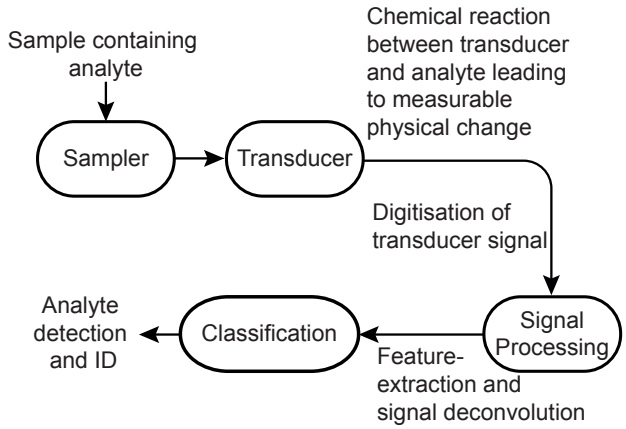

Figure 2.1: *Scheme of a sensor featuring sampling system, transducer, and signal analysis and ID components.*

2.2.2 *Transducers - instruments and techniques*

The transducer is the element of a sensor that produces a signal in the presence of an analyte, and could be one of two types. A physical transducer measures a physical property of molecules passing through the system, for example their absorbance of light, or mass (e.g. absorption spectroscopy or mass spectrometry). A chemical transducer interacts directly, or reacts with the sample and changes its properties (colour, fluorescence, solubility *etc.*) on interaction with the analyte. The measurement of this change is the sensing signal.

The latter can be very sensitive, relying on highly specific interactions between small amounts of analyte passing over the transducer element. These small changes can be massively amplified by careful design.[18] It is possible to design the transducer element to only produce a signal in the presence of the desired analytes - this introduces specificity.

More than one transducer can be included in a sensor, and the group of transducers is referred to as an 'array'.

2.2.3 *Recognition and identification*

The signal produced by the transducing element must be interpreted. If the transducer produces a simple colour change (for example a lateral flow test such as a pregnancy test) then this analysis can be done quickly by the user.

However if a sensor is designed to detect multiple analytes at once, or the signal is not easily visible to the naked eye, then an electronic reader may be required.

An area of great interest is the chemical nose/tongue approach, which uses an array of chemical transducers to create a unique pattern for each analyte with which they interact. This pattern can then be processed by a computer to output a match, based on a library of known possibilities. The interactions between receptor and analyte do not have to be 100% specific, so that a small number of sensors can detect a large number of analytes. This mimics the mechanism of the mammalian nose and tongue, giving rise to the name.[19]

For this technique to work, pattern recognition software is required to analyse the signals generated and compare them to a stored library of signals that have been pre-determined. This utilises a branch of statistics called 'machine learning'. Techniques include support vector machine (SVM) analysis, principal component analysis (PCA), artificial neural network (ANN) analysis, linear discriminant analysis (LDA) and many more.[20–24] Although the mathematics behind each of these techniques is different (and complex), the overall workflow is the same. The various signals, created by interaction between the array and the analyte, are gathered, with each signal containing one or more dimensions to create the multidimensional dataset. This dataset is then treated by the mathematical formulae of the technique to reduce it in complexity and compare it to a library of known analytes. A match (or not) is then presented, possibly with a certainty value, indicating the confidence of the match.

More detail and examples of this chemical nose/tongue technique are presented in Chapter 5.

2.2.4 *Explosives sensing - existing techniques*

The bulk of existing instrumental techniques for detecting explosives can be summarised into mass spectrometry, ion mobility spectrometry (IMS), fluorescence techniques, and electrochemical techniques.

Mass spectrometry is a gold-standard technique that is well researched for laboratory-based explosives analysis, and coupled with liquid chromatography, is a powerful tool for quantitative trace explosive analysis even in complex mixtures.[10, 25] However mass spectrometry is of limited use in the field, or for point-of-threat sampling, due to the expensive and fragile high-vacuum equipment that is required.

A similar, but importantly non-vacuum, technique which has been extensively developed for explosives detection is IMS. It detects air-born particulates and vapours from explosives by sampling the local environment either with a fan to draw in air or by heating an inserted swab and sampling any volatile materials that are given off. This sample is then ionised using a radiation source or latterly with an electro-spray technique, and passed along a charged drift tube.[26] The time it takes the different charged fragments or molecules to reach the detector at the end gives a signature for that molecule, indicative of its mass and charge, and can be used to identify explosives.[27, 28] This technique is currently widely used in airports and by the military in the field.

The most recent commercial tool for explosives detection utilises fluorescence quenching by explosives. In particular it centres around the quenching of fluorescent polymers. Swager *et al.* have achieved very high sensitivity towards nitroaromatic explosives with conjugated fluorescent materials, that operate on a 'christmas lights' effect, one molecule binding quenches a whole polymer chain, greatly enhancing the signal.[29–32] Other fluorophores are now being investigated widely for explosives detection,[33] such as small molecules,[34–37] and ordered hierarchical structures like metal organic frameworks (MOFs).[38–41]

A final popular method utilises tools that detect explosives by their electrochemical signature. These are often simple robust systems that can operate in solution, measuring explosive levels in bodies of water or in waste water.[42, 43] They have also been applied to vapour phase detection - in particular using metal oxide semiconductor (MOS) sensors to detect analytes in a flow of air.[21, 44, 45] A drawback to these systems is the requirement for high operating temperature and sensitivity to operating temperatures and humidity.

2.3 NANOMATERIALS FOR SENSING

An area of interest for chemical sensing is the application of nanomaterials as the transducing element in a sensing architecture. This section very briefly reviews nanomaterials, and gives two specific examples of nanomaterial sensors, and their mechanism of transduction.

2.3.1 *Nanomaterials and their synthesis*

A nanomaterial is traditionally classed as any substance that contains a structural dimension of less than 100 nm. Although broad, this definition can then be used to subdivide nanomaterials into four classes based on their dimensions: 0D, 1D, 2D and 3D (Fig. 2.2).

A particle of material such as a sphere with diameter less than 100 nm is referred to as a 0D nanomaterial. A (nano)wire with diameter less than 100 nm, but a greater length, is 1D, and a structure with thickness of less than 100 nm is a 2D nanomaterial. Finally an object with all external dimensions greater than 100 nm, but that contains a nanoscale component, such as pores or protrusions is called a 3D nanomaterial.[46]

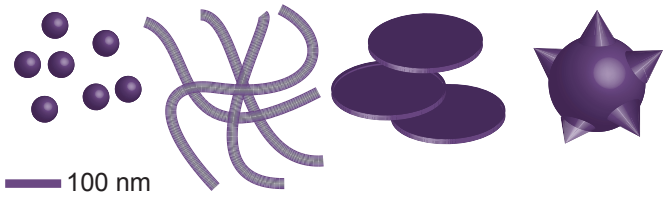

Figure 2.2: *Schematic of (from L to R) 0D, 1D, 2D and 3D nanomaterials containing features at the nanoscale. The 3D material has pointed structures of less than 100 nm, but porous materials might also be included in this catagory.*

The small size of such components dramatically increases the surface-area-to-volume ratio of the material, meaning that, in effect, to study nanomaterials is to study surface phenomenon rather than bulk properties. This high surface area greatly increases opportunities for analytes to bind and effect a chemical change in the system, so there is the potential for high sensitivity. The small size of nanomaterials also means that many display

so-called 'quantum effects', giving them novel and often highly useful electromagnetic properties that can be utilised in detection systems.

Nanomaterials can be created by a huge variety of processes, but these are broadly categorised as top-down or bottom-up. A top-down approach involves breaking up bulk material into smaller pieces, *via* grinding or ablation for example. Bottom-up synthesis grows particles *via* self assembly of atoms in solution, or *via* controlled atomic deposition in a vacuum system, such as molecular beam epitaxy.

The work in this thesis centres around the growth of 0D nanomaterials, so-called nanoparticles, *via* solution phase bottom-up synthesis. These are referred to as colloidal suspensions. The small size of the resultant nanoparticles leads to optoelectronic properties that then can be applied to chemical sensing.

The particle synthesis is achieved by creation of a small nucleus of pure material by local concentration (to the point of super-saturation) of a solution-phase precursor, followed by growth of this nucleus. To group a set of precursor atoms into a particle nucleus an energy barrier must be overcome. The free energy of particle growth is approximated as:

$$\Delta G = -\frac{4}{3}\pi r^3 \Delta G_v + 4\pi r^2 \gamma \tag{2.1}$$

The change in Gibbs free energy is composed of the linear combination of the energy of particle lattice growth and the change in particle surface energy. The arrangement of atoms into a bulk lattice lowers the free-energy, but there is an energy cost of breaking the solvation shell around each atom, and any surface bonds of the existing nucleus. ΔG_v is the change in free-energy per unit volume resulting from the lattice growth, and is dependant on the concentration of the precursor in solution. γ is the surface energy per unit area for the particle. When ΔG is plotted against r (Fig. 2.3a), initially the surface energy term dominates, creating an energy barrier, until a critical radius (r^*) is reached. From this point, the volume term takes over, and particle growth starts to lower the free energy. This energy barrier must be overcome to trigger nanoparticle formation.[47]

If particle nuclei are formed in a single initial burst, and then grow at a uniform rate, the final nanoparticles will be very homogeneous in size and shape, giving a monodisperse particle population. If the nucleation is not rapid, different nuclei, formed at different times, will grow at a variety of rates, leading to polydisperse particles. As the particles grow, the precursor concentration falls away sharply, so that the final stage of growth is diffusion limited. This is the LaMer model of particle growth (Fig. 2.3b).[48] After the precursor is consumed, the particles may continue to change size *via* Ostwald ripening, whereby material is exchanged between particles to reach a more homogeneous size population, often leading to larger particles growing at the expense of smaller ones.[49]

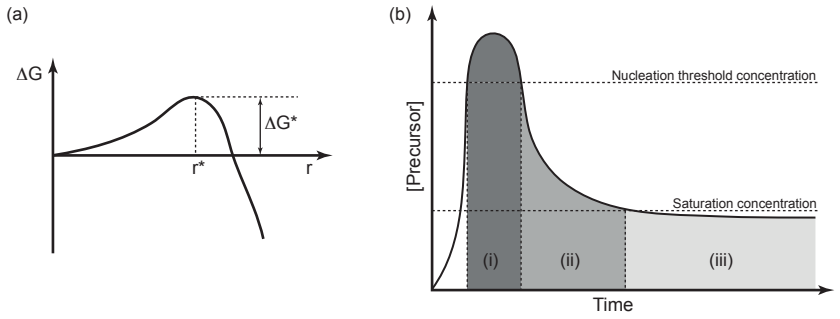

Figure 2.3: *(a) Change in the Gibbs free energy on particle formation and growth. r* is the critial particle radius, ΔG* is the energy barrier to particle formation. (b) Schematic of the LaMer model of particle growth as a factor of concentration. The initial super-saturation (i) causes nucleation of particles, followed by rapid growth (ii), leading to a sharp drop in concentration of the precursor, so that the final growth step (iii) is diffusion controlled - ripening.*

To induce the desired single, sharp nucleation point, several methods can be used - one example is the rapid reduction of a precursor with a powerful reducing agent, as in the Brust-Schiffrin gold nanoparticle (AuNP) synthesis (see Section 3.1.1 for more details). A second method is fast injection of a cold precursor into a very hot solution, causing instant super-saturation of the precursors, leading to rapid nucleation, followed by a temperature reduction, preventing any secondary nucleation events.

To passivate the final nanoparticles, an overgrowth of some other material can be achieved to create a core@shell structure. This can prevent chemical modification (e. g. oxidation) of the particles, and also post-synthetic growth processes, such as ripening. It may also improve the desired properties of the

final particles, for example improving catalytic behaviour or optoelectronic properties.[50]

To further control the nanoparticle growth, surfactants - ligands that bind to the outside of the nanoparticle - are introduced to induce size and shape control, *via* blocking growth of particular crystal facets, and modify the solubility properties.

The surface ligands on a nanoparticle can vary as widely as the materials used to create the particles, and can be attached covalently (e.g. thiols), by utilising electrostatic interaction or by hydrophilic/hydrophobic interactions (e.g. biomolecules such as proteins or polymers). Fig. 2.4 demonstrates some examples on a core@shell QD surface, but similar thiols to (b)-(e) also work well on gold and silver surfaces.[51–54] The ligands attached to nanoparticles do more than simply passivate the surface; the distal end of the surfactant can be modified to introduce surface functionality to the nanoparticle, allowing for targeted binding to molecules of interest/analytes.

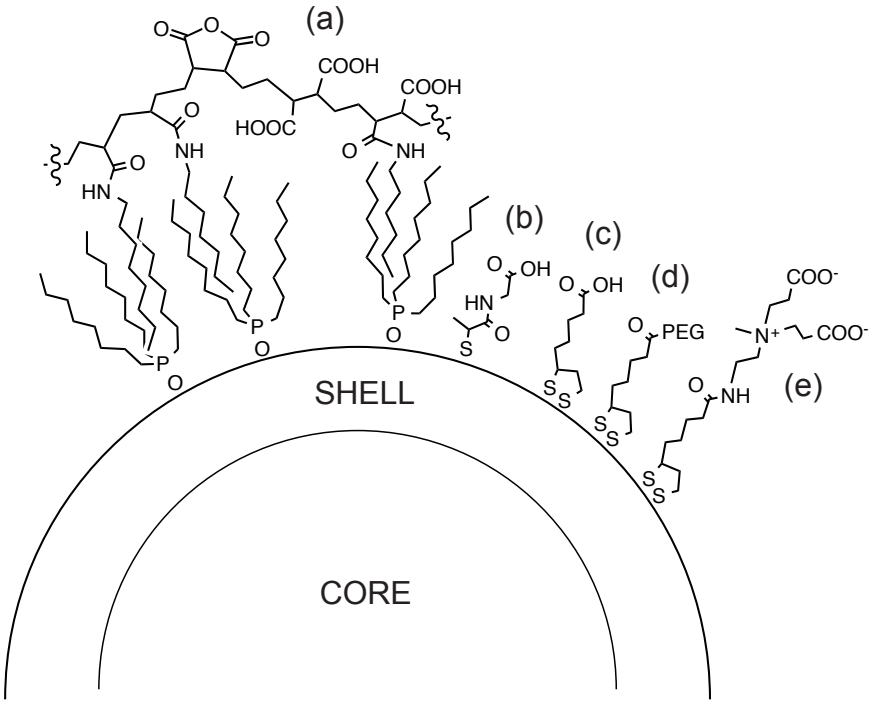

Figure 2.4: *Examples of surface ligands attached to a core@shell QD, demonstrating (a) a hydrophobic/philic polymer coating interacting with TOP, decorated with anhydride moities for attachment; (b) tiopronin, a mono-thiol; (c) lipoic acid, a dithiol; (d) PEG functionalised lipoic acid for added hydrophilicity; and (e) a zwitterionic lipoic acid.*

2.3.2 *Targetting nanoparticles towards explosives*

Binding between the surface ligand and target analyte can be achieved in several ways using conventional chemical interactions: Van de Waals forces, electrostatic binding, such as permanent dipole interactions or π-stacking, or covalent binding.

In the application of nanoparticles to the detection of explosives, there have been three main ways that (partially) specific binding and recognition have been achieved; Meisenheimer complexes, molecularly imprinted polymers (MIPs) and antibody binding.

Meisenheimer complexes are covalent adducts that have been incredibly widely used as the basis for the detection of materials such as TNT and tetryl. For these molecules, the three nitro-groups on a benzene ring create a highly electron deficient arene, which will react with primary amines and other good nucleophiles. If the nucleophiles are bound to the surface of a nanoparticle, then signal transduction from the nanoparticle can be achieved.[55–60] It should be noted that this binding may be weaker for tetryl due to the slightly electron donating nature of the nitroamine group destabilising the complex shown in Scheme 2.1. It has been shown that DNT does not form strong Meisenheimer complexes due to lack of electron withdrawing groups.[61] Where Meisenheimer complexes have been used to bring about a spectral (absorbtion or fluorescence) change, there is also some debate as to whether the result is caused by formation of a complex, or simply an acid-base interaction.[62]

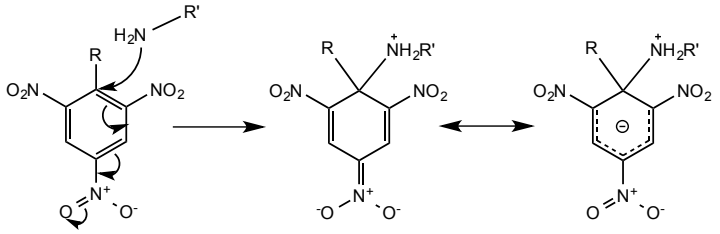

Scheme 2.1: *Formation of a Meisenheimer complex between a nitroaromatic and a primary amine. For TNT, R=CH_3 and for tetryl R=$N(CH_3)(NO_2)$.*

Although this method can discriminate a little between nitroaromatics, there are problems of low specificity as other electron deficient arenes, or indeed other types of molecule, that are not explosives can bind to the strong

nucleophiles used to form the complexes. In addition this method cannot detect non-aromatic explosives such as RDX or PETN.

MIPs are polymer matrices containing analyte specific voids. These are made by polymerising a material around a template for the analyte (similar to, or the analyte itself) and in addition, incorporate a transducer such as a fluorophore nanoparticle into the matrix. The template is then removed leaving the receptor site ready for detection. When the analyte binds to the site, it is brought into proximity of the nanoparticle, and a response is affected. These have been successfully used to detect TNT and DNT.[63–65] Similar systems using the polymerisation of nanoparticles directly with cross-linking of surface groups have also been applied to the problem.[66, 67]

These types of systems have better specificity than Meisenheimer complexes due to the use of a template, and are in theory not limited to nitroaromatics alone, with Riskin and Willner designing a system for the detection of RDX.[67] However not all materials can be easily templated, and once polymerisation is complete it may be difficult to achieve full template removal. In addition, lack of control over positioning between the analyte and signal transducer can lower the system's sensitivity.

The third method of targeting nanoparticles to detect explosives is via the attachment of antibodies to the nanoparticle surface. Antibodies can be created *in-vitro* to be highly specific receptors to a single explosive analyte, and then harvested. Once purified they can be attached to nanoparticle surfaces to act as receptors.[68–71] However, antibodies are expensive, and have a long lead time to creation of new antibodies specific to new materials.

In addition to the three methods above, there are other chemical recognition strategies that exploit some of the quite unusual properties of explosive materials. High explosives are particularly nitro-rich and highly electron deficient, meaning they can form strong donor-acceptor complexes, and as TNT and related materials are aromatic, π-stacking can be induced.[72, 73] Peroxide based explosives such as TATP are strongly oxidising so their presence can be probed by redox active ligands.[74] However problems naturally arise as other molecules may share some of the properties targeted.

Nanoparticle-ligand systems can be targeted to specific analytes to effect a change in the properties of the nanoparticles. We will examine two examples here, in which the electromagnetic properties of the nanoparticles (arising from their small size) are altered by analyte binding, and can be applied as a transducer in a chemical sensing system for explosive analytes. The first property reviewed is the surface plasmon resonance (SPR) band of colloidal AuNPs, and the second, the fluorescence of colloidal semiconductors.

Sensors based on these nanoparticle properties have the potential to detect picomolar or lower concentrations of explosive analytes, and can operate for both solution phase and gas phase detection.[4] In addition, measurement of the signal produced by the nanoparticle transducer uses standard scientific instrumentation, making it easier to build complete detection systems from standard components - an important consideration.[75]

2.3.3 *Nanoparticle transduction for sensing*

Two areas that are of interest to sensing are the plasmonic properties of gold nanoparticles (AuNPs), and the fluorescence properties of semiconductor nanoparticles - quantum dots (QDs).

2.3.4 *Example - Gold Nanoparticles*

In gold nanoparticles (AuNPs) the free electrons of the metal surface interact strongly with light to cause large oscillations in the surface electromagnetic field. The particles therefore absorb light strongly at the particular resonant frequencies of these electrons, giving rise to surface plasmon resonance (SPR) bands.

The position of these absorbance bands give rise to the strong colour of gold colloids and they are easily measured by UV-visible absorption spectroscopy (UVVis). The frequency of the electron oscillations, and therefore the position of the SPR bands, is very surface sensitive, and can be altered by changing the size and shape of the nanoparticle, by changing the surface

charge distribution with ligands, or by bringing several particles into close proximity.[76]

This SPR property has been exploited to detect various explosives, particularly through application of Meisenheimer complexes. Induced aggregation of AuNPs by reactions of surface amine groups with TNT or other nitroaromatic explosives causes a red shift in the SPR band that is easily detectable by eye.[59] In addition SPR band changes have been used as transduction mechanisms in MIPs as previously described, as well as antibody-based assays.[69]

A second and quite different method to exploit the SPR band of AuNPs is by measuring a surface-enhanced Raman spectroscopy (SERS) effect. A Raman spectrum is a powerful way to fingerprint a molecule, using incident light to excite Raman active vibrational modes (shown in Fig. 2.5a), causing inelastic scattering of the photons, and giving rise to a unique spectrum that provides information on molecular shape and connectivity. The spectrum obtained from an unknown analyte can be compared to a library of known spectra and used to identify a threat. However, Raman scattering is very weak, and so to detect low levels of analyte, enhancement is required.

If a molecule is bound (chemi- or physisorbed) to a metal surface, incident light (usually a monochromated laser pulse) excites the surface plasmons, inducing polarisation in the bound molecules, increasing the amount inelastic scattered light from the Raman vibrational modes (Fig. 2.5b). This leads to a signal enhancement of up to E^4, where E is the electric-field magnitude. The enhancement factor on a single molecule (EF) is given by the equation:

$$EF = \frac{\mid E_{\mathrm{Loc}}(\omega_{\mathrm{L}})E_{\mathrm{Loc}}(\omega_{\mathrm{R}}) \mid^2}{\mid E_{\mathrm{Inc}} \mid^4} \approx \frac{\mid E_{\mathrm{Loc}}(\omega_{\mathrm{L}}) \mid^4}{\mid E_{\mathrm{Inc}} \mid^4} \tag{2.2}$$

Where E_{Loc} is the local field for the excitation wavelength (ω_{L}) or Raman scattering wavelength (ω_{R}), and E_{Inc} the incident field. The local fields for the incident and scattering wavelengths can be approximated to be equal at small Stokes shifts.

The intensity of the SERS effect is largely attributed to the monolayer of molecules absorbed to the nanoparticles, and is highly dependant on the form (and hence plasmonic field) of the nanoparticles. This adsorption

onto the substrate also creates new vibrational selection rules, and surface-complex formation can lead to altered electronic properties of the absorbed molecule.[77]

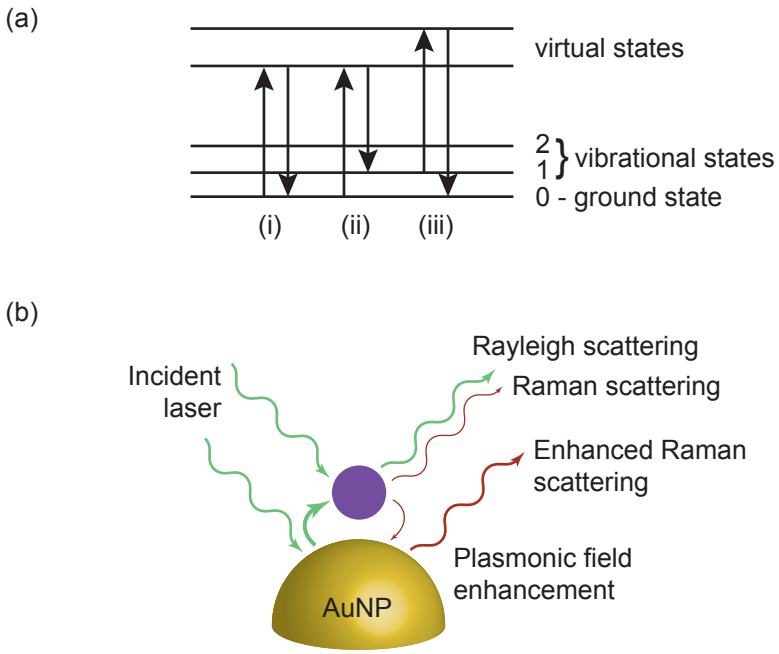

Figure 2.5: *(a) Basic inelastic scattering modes that give rise to Raman spectra. (i) Rayleigh scattering - elastic scattering that is discarded from the spectrum. (ii) Stokes Raman scattering, where the change in wavelength of the emitted photon gives the Raman signal. (iii) Anti-Stokes Raman scattering - much weaker than the Stokes equivalent. (b) Electromagnetic enhancement of Raman scattering for a physisorbed analyte on an AuNP surface. Both incident laser light and outgoing Raman light are enhanced by the particle plasmonic field. Adapted from Guerrini & Graham.[77]*

The best SERS enhancement is achieved by having strong localised plasmons, that fall within the excitation wavelength of the laser excitation. For this reason gold and silver are often chosen as their SPR bands are typically within 400 - 800 nm, which is easy to access with a visible laser.[78] In addition they are chemically inert and thus stable against air, and strong oxidising or reducing agents. Other materials have been successfully applied as SERS substrates, such as other noble metals (Pt and Pd) and even transition metals and semiconductors.[79, 80]

Strong plasmon hotspots created in-between individual particles can improve the SERS enhancement effect. This can be achieved through aggregation of the particles, either in solution by trapping at an interface or chemical aggregation with linking molecules, or by solvent removal.[81–84]

Another way to create SERS hotspots on particles is by modification of the shape of the particles. Although typical AuNPs are spheroidal, it is possible to produce rods, cubes, prisms, and more complex star and flower like shapes.[85–88] The latter two, especially, show highly enhanced SERS effects due to localisation of the plasmon electromagnetic fields at edges and tips of their complex shapes.[89] Nanostars are larger nanoparticles with various sized protuberances, and a generally more lumpy shape, also known as nanodendrites (as shown later in Fig. 3.1c).[88, 90, 91] Nanoflowers are 3D nanostructures, with micro-scaled particle sizes, but highly complex structured ridges and planes at the nanoscale, to create the desirable edge or tip enhancements.[86] These more complex shapes are often produced from spherical gold seed particles, that then undergo preferential growth along particular crystal planes, guided by introduced dopant atoms (e.g. Ag) or surfactants.

In recent years SERS on nanoparticulate colloids has been heavily applied to the detection of illicit materials, such as explosives.[58, 92] The technique has been shown to be capable of detecting a range of high explosives, with good detection limits (into the nanomolar region or below), even with raw colloidal solutions of Au and AgNPs such as those applied by the group of Hernández-Rivera.[93, 94]. By aggregating AuNPs at an interface, Cecchini *et al*. created a regular monolayer array, which showed enhanced sensitivity to a range of compounds, including some explosives.[81]

A more targeted approach has been taken by utilising NPs functionalised with cysteine to form Mesienheimer complexes with nitroaromatics.[95, 96] Xu *et al*. demonstrated enhanced detection of DNT by using cyclodextrin coated triangular nanoprisms of gold.[97] SERS also extends beyond the nitroaromatics, for example it has been shown that RDX can be detected at concentrations as low as 0.15 mg/L in ground water samples.[98] This illustrates a key benefit of SERS, that it is label free, requiring no special binding groups to target particular analytes, but that it can become more targeted with designed substrates.

SERS is a potentially very useful technique for detection of explosives and can detect solution or vapour phase materials at very low concentrations. The individual Raman fingerprint of each different molecule makes speci-

ficity high, however in complex mixtures, deconvolution can be a challenge.[23] A second problem is the dependence of the Raman signal on the SERS substrate. Particular vibrational modes in the Raman spectrum can be enhanced or suppressed depending on the binding mode of the analyte, and if the substrate (e.g. AuNP concentration and aggregation amount) is not identical in every instance then the fingerprints may differ slightly, causing loss of specificity. Therefore, a key requirement is the development of cheap, identical SERS substrates, that exhibit powerful enhancement, ensuring strong and repeatable spectral fingerprints can be obtained on each use.

2.3.5 *Example - Quantum Dots*

Quantum dots (QDs) are semiconducting nanoparticles which are small enough to confine a generated hole-electron pair (exciton) within all 3 spacial dimensions (that is, they are smaller than the exciton Bohr radius for the material), leading to quantisation of the energy levels. This causes the electronic structure of the material to sit between a classical semiconductor, and a molecular material (Fig. 2.6).

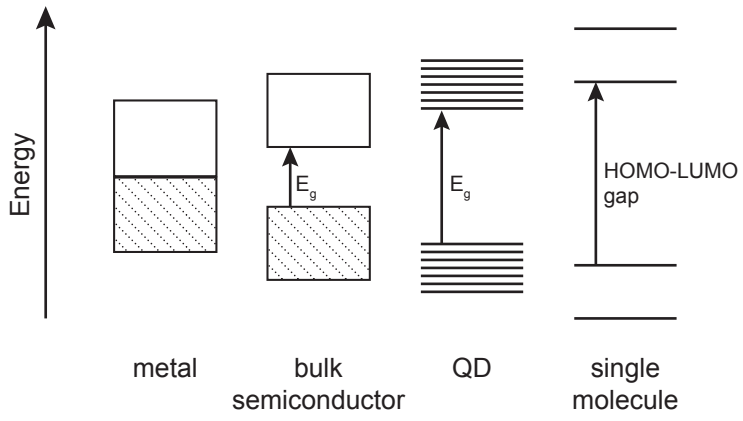

Figure 2.6: *Schematic of band structures of metals, semiconductors, quantum dots (QD) and single molecules, showing the increase in band gap (E_g) as confinement is increased. At the single molecule scale the energy bands become completely discrete, and the QD sits between this system and the band model of semiconductors.*

The result of this quantisation of states is that the nanoparticles display sharp photon absorption and emission bands, and the band gap is closely related to the size of the nanoparticle.

The fluorescence arises from photoexcitation of the nanoparticles, causing excition formation. Recombination of this excition will then occur through radiative (fluorescence) or non-radiative (trap-states, oxidation, energy transfer) pathways, as detailed in a Jablonski diagram (Fig. 2.8). The fluorescence from QDs is easily tuned to the visible or near-IR region of the spectrum, by choice of semiconductor material and particle size, making QDs useful fluorophores.

The size of the QD is linked to the particle band gap by the Brus equation, Eqn. 2.3. This models the band gap (E_g) as a function of the bulk semiconductor band gap (E_g^{bulk}), the confinement energy (based on the particle in a box model) and a modified coulombic attraction between the electron and hole:

$$E_g = E_g^{bulk} + E_{confinement} + E_{exciton} \tag{2.3}$$

$$= E_g^{bulk} + \frac{h^2}{8\mu r^2} - \frac{1.8e^2}{\epsilon r} \tag{2.4}$$

Where r is the particle radius, μ the reduced mass of the exciton pair and ϵ the permittivity.[99, 100]

The physical outcome of this relationship is that, as the size of a QD decreases from the exciton Bohr radius, the band gap increases from that of the bulk material, blue-shifting the photoluminescence of the QDs (Fig. 2.7a).

QDs were first demonstrated in 1981 by Ekimov & Onushchenko,[101] and Brus *et al*. first developed colloidal syntheses in 1985, that were refined by Bawendi *et al.* in later years.[99, 100, 102]

Typical materials for QD synthesis are II/VI semiconductor pairs such as CdSe, CdTe and ZnO, or III/V materials such as InP or InAs. An excellent overview of the effect of different materials on the photoluminescence properties of QDs is provided by Michalet *et al.*[103] These nanoparticles are typically synthesised *via* the hot-injection method discussed in Section 2.3.1, and can then be shelled with an inert capping material to protect, modify and even enhance the optoelectronic properties. Other methods to synthesise QDs have included sonochemical and mechanochemical methods as well as harnessing natural biochemical processes.[104–106]

QDs can also be constructed from materials that are not semiconductors in their bulk state, such as gold or carbon, and confinement has a similar effect on their band structure.

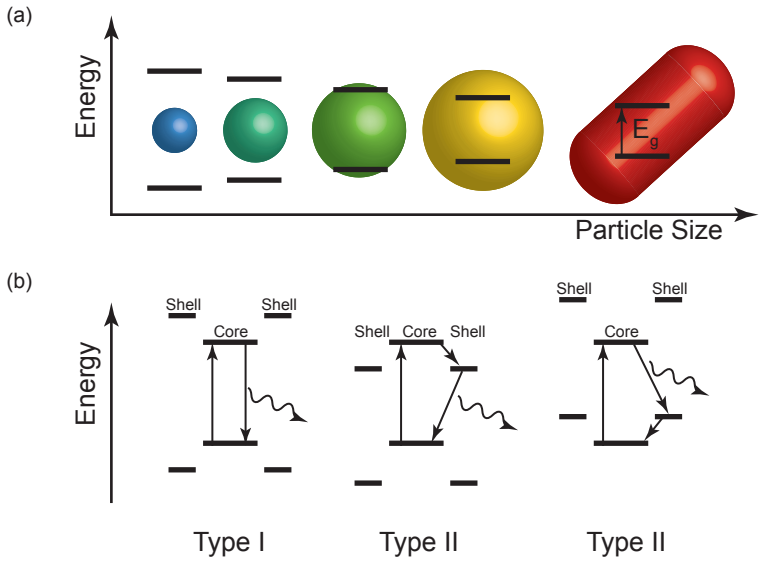

Figure 2.7: *Graphic illustrating (a) the change in QD band gap and photoluminescence emission wavelength with increasing particle size, and (b) Type I or Type II shelling schemes.*

The relationship between the band gap of the quantum dot core and that of the capping material defines the particles as one of either Type I or Type II (Fig. 2.7b).

Type I shelling occurs when the shell has a larger band gap than the core and encompasses it. This leads to very little change in the fluorescence pathway, although due to some surface defect elimination and slight exciton leakage (partial tunnelling) into the shell, a small red shift often occurs along with an improvement in quantum yield.[107] An example is CdSe@ZnS.

Type II shelling creates a staggered band gap system, leading to a large redshift in the band gap, and a longer recombination pathway, leading to longer photoluminescent lifetimes. An example is CdTe@CdSe.[108]

Just as changing the shell around the QD core can alter the fluorescence recombination pathway, altering the environment of the quantum dot can effect the final outcome of electron-hole recombination.

In a perfect system, the photo-excitation of a QD results in the creation of an exciton which then recombines to emit a photon, as portrayed by the Jablonski diagram, Fig. 2.8. Trap states in the band gap, caused by surface or interfacial defects, can alter the wavelength of the emitted photon, or

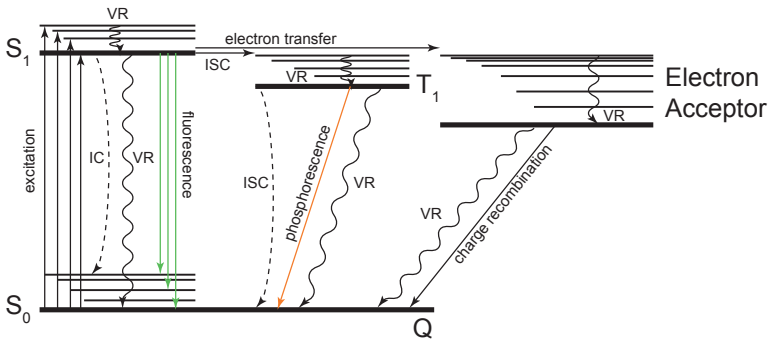

Figure 2.8: *Jablonski diagram showing various radiative and non-radiative processes for recombination of an exciton in a QD. Of particular interest is photoinduced electron transfer to another chemical moiety, leading to fluorescence quenching. VR is vibrational relaxation, IC is internal conversion of S_1 to S_0, ISC is intersystem crossing of S_1 to T_1 or T_1 to S_0. Radiative processes are coloured. Q is the configuration coordinate. Adapted from Williams.[109]*

prevent recombination of the exciton altogether by promoting internal conversion or other processes.

Introducing molecules around the surface of the QD will affect the rate of recombination of the exciton, and may also disrupt it's recombination. In particular the conduction band electron may be lost to a local species in a process termed photoinduced electron transfer (PET).

In PET the loss of the excited electron to the acceptor results in the prevention of recombination, and thus the loss of fluorescence. The acceptor becomes a radical anion which can then lose its electron back to the donor *via* a non radiative path.

The more efficient this process, the larger the fluorescence quenching of the system. Efficiency can be improved by making the acceptor more electron deficient, and by shortening the distance the electron must be transferred over.

This electron transfer mechanism has been used extensively to transduce the presence of analytes in proximity to a QD, and thus form the sensor element in a chemical sensor.[110–112] The surface of the QD can be targeted to certain analytes by the placement of receptors on the surface that preferentially bind the analyte and bring it into close proximity with the QD, facilitating the PET mechanism, and quenching the observed fluorescence.[113] This has been used for both biomedical and security sensing applications.[53]

A secondary, and equally important process that can occur is Förster resonance energy transfer (FRET), the movement of a virtual photon from an excited donor to an acceptor with suitable spectral overlap, and in close enough proximity. This process is less important in this thesis and so will not be discussed at length here, but it should be noted that Cyriac et al. have recently used this mechanism for sensing of RDX and PETN.[114]

Biomedical sensing often utilises antibody targeted analyte binding, for example, the sensing of *E.coli* with QDs.[115, 116]. However, other types of sensors have been explored, for example, QDs with redox active capping ligands that alter the PET pathway on changes to pH.[117, 118] Other examples include sensors for bio-thiols (based on displacement of a TiO_2 nanoparticle (NP) PET quencher),[119] glucose,[120] or cancerous cells (both based on AuNP PET quenchers),[121] or nitric oxide.[122]

In the security domain, QDs have been used extensively for sensing toxic metal ions in water.[123, 124] Of more importance to this thesis, they have also been used for approximately 10 years as a fledgling sensor for explosives. Due to explosives' (particularly nitro/conventional explosives') electron deficient nature, they make excellent PET quenchers.[125] Initially antibody targeting of explosives was used, but this is expensive and complicated due to the procedures required to obtain, purify and conjugate the antibodies.[70, 71] A cheaper and simpler targeting approach has been the formation of Meisenheimer complexes, as with AuNPs, using surface amines to bind nitroaromatics, such as TNT or picric acid.[126–131] This system can be highly specific towards nitroaromatic materials, but is very difficult to apply more widely to other explosives (even DNT).

A novel donor/acceptor system for the sensing of explosives beyond TNT has been pioneered by Willner *et al.* They have utilised both a redox couple based on NAD^+/NADH and a donor/acceptor scheme, based on surface bound dopamine derivatives, to sense a range of explosives, including RDX.[132, 133]

Beyond these popular methods, there has been some research into the formation of supramolecular complexes on the surface of quantum dots using macromolecules or cavitands. Macromolecules such as polymers and dendrimers can encapsulate the QD, trapping explosives near the surface.[134–136] Examples of cavitands include cyclodextrins, which have been used to detect small aromatic hydrocarbons, but not explosives, using either surface bound cyclodextrins that bind a guest, causing change in QD fluorescence, or other surface bound states that bring a free cyclodextrin into proximity of the QD.[137–139] Similarly, QD surface bound calixarenes have been used to

detect molecular species such as pesticides or buckminster fullerenes (C_{60}), but not as yet explosives.[140–145]

These two particular macrocyclic systems will be discussed at more length in Chapter 4.

A final example of explosives sensing with QDs, is one that instead of tailoring the surface ligands to bind to explosives, removes them altogether, to achieve good sensitivity to certain metal ions, or picric acid.[146]

QDs, therefore, have many properties of interest to chemical sensing - they exhibit high fluorescence quantum yields, are resistant to photobleaching, and have broad absorption giving rise to narrow emission bands. This means they lend themselves well to a multiplexed or multichannel fluorophore system, with a single excitation wavelength causing emission from many different species of varying colour. The surface of the particles is easily modified with targeting ligands to allow specific and sensitive fluorescence enhancement or quenching on association with an analyte *via* a PET mechanism.

2.4 SUMMARY

The properties of nanomaterials make them a good tool for the creation of a transduction element in a chemical sensor. By varying these properties, altering their aspect, size, material and surface coating, it is possible to achieve a range of functional materials that might be applied to explosives sensing. Nanoparticles will be focussed on, due to their simple and highly controllable synthesis, and in-particular, new gold and semiconductor nanoparticles will be tested for their explosives sensing capabilities.

3

GOLD NANOPARTICLES

3.1 RATIONALE

As discussed in Section 2.3.4, gold nanoparticles (AuNPs) are a powerful tool for molecular detection through application of SERS or colorimetrics. The aim of this part of the project was to further understanding of a novel synthesis of various types of AuNPs that has been recently discovered, and then investigate their application to chemical detection.

3.1.1 *Typical AuNP syntheses*

There have been many formulations of colloidal gold developed since Faraday described his production of AuNPs with phosphorus and chloroauric acid ($HAuCl_4$).[147] The most utilised syntheses applied in recent literature are the Turkevich/Frens,[148–150] and Brust-Schiffrin syntheses.[151] The former employs boiling aqueous sodium citrate solution as both the reducing agent of the gold (III) precursor and also the capping agent. The process produces reasonably uniform particles of 10-25 nm, with a rich red colour indicating an SPR band of approximately 520 nm (Fig. 3.1). The reaction proceeds *via* an Au(I) - citrate intermediate that rapidly decomposes to gold nuclei [152]. These nuclei are suggested to be about 5 nm in diameter and proceed to agglomerate first into nanowires, then into larger spherical particles.[49, 153, 154]

The Brust-Schiffrin synthesis has several key differences to the Turkevich/Frens methodology. It does not utilise heating, and relies on the more powerful reductant of sodium borohydride. Particle size is controlled with thiol capping agents (for example dodecanethiol (DDT)) in an organic solvent. The gold precursor is transferred from water to toluene by formation

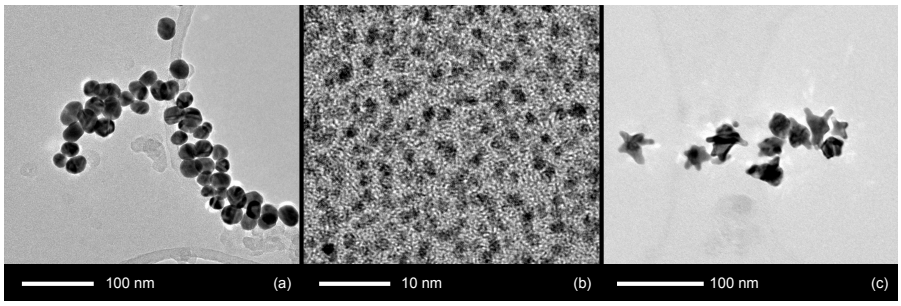

Figure 3.1: *Representative TEM micrographs of AuNPs produced with the (a) Turkevich and (b) Brust-Schiffrin methods, illustrating the relative scale of the particles produced. In (b) lattice planes are visible. (c) Gold nanostars prepared with the method of Xie et al.[155]*

of a complex with tetraoctylammonium bromide (TOAB), then reduced with borohydride to form a brown solution of 1.5 - 3 nm particles. The particles remain small because they are immediately capped with the thiol, and due to the great strength of the sulphur-gold bond, the particles are highly stable against further growth. This allows them to be easily handled, precipitated and used for further reactions.[151, 156]

There has also been a race to the bottom where AuNPs are concerned with attempts to create reproducible syntheses for stable metal clusters of as few as 11 gold atoms.[157–161] These clusters often display quantum dot like properties of fluorescence, making them of interest for the sensing of explosives.[162–164]

Countless variations on both the above syntheses have been reported in recent years, with a particular emphasis on controlling size and dispersity.[165, 166] However, it has also been discovered that the capping ligand can greatly vary the shape of the particles formed. Of relevance here is the growth of so-called 'nanostars', which have narrow gold tips protruding from the particle surface. These are often grown by further reduction of gold on to pre-formed gold seeds in the presence of poly(vinylpyrrolidone) (PVP) in dimethylformamide (DMF).[88, 90] A more simple, aqueous synthesis of particular interest is the reduction of chloroauric acid in HEPES buffer solution to give 30-50 nm star shaped particles.[155]

In an attempt to find alternate aqueous AuNPs syntheses without the need for the protracted boiling step of the Turkevich synthesis, researchers have experimented with various facile reduction methodologies, whilst trying to maintain control over particle size and shape. In 2004 a first demonstration of the controlled formation of AuNPs by the β-diketone acetylacetone was presented by Kundu *et al.*[167] This was contemporaneous to the discovery of 'green' AuNP synthesis; the application of various plant extracts to $HAuCl_4$ to produce a range of nanoparticles and nano-plates (large

2D structures several 100 nm in side length but only a few nm thick). The reduction mechanism in such reactions has not been definitively determined, but suggested examples highlight the importance of ketone groups and amides contained in the plant extracts.[168–174]

In 2013 Uppal *et al*. described the use of a cyclic mono-ketone, cyclohexanone, to produce nanoparticles and nanoplates.[175] This built on the work by Kundu *et al*., presenting suggestions for a reduction mechanism for the gold, *via* formation of an enol and C−Cl bond, and providing gas phase IR evidence of the expected reaction products. The work described here builds on this new understanding, by applying a range of different ketones to produce AuNPs and probing how a homologous series influences the particles produced. The cyclohexanone and acetlyacetone reactions previously described were re-examined and then seven different, but related, mono- and diketones were tested and the resulting colloidal suspensions characterised.[91] One of the classes of particles was then tested in a SERS sensing application.

3.2 GOLD NANOPARTICLE SYNTHESIS

3.2.1 *General synthetic methods*

An aqueous chloroauric acid ($HAuCl_4$) stock solution was made up to 6 mM with anhydrous $HAuCl_4$ in water. The colloidal suspensions were synthesised by mixing an excess of each ketone (full details in Section 8.5.2) with water to a total of 10 mL and then injecting the gold stock solution (0.44 mL) rapidly, followed by brief mixing. Nine ketones were used in total, shown in Fig. 3.2.

The reactions were left to stand at room temperature and the colour changes were observed, with a developing red or purple/orange colour indicated the formation of gold colloid. Reaction time was estimated by UVVis monitoring, and from X-ray photoelectron spectroscopy (XPS) data collected after 24 hours. For the latter, portions of each reaction were freeze dried for 120 hours and submitted for XPS on carbon tape, and infrared

spectroscopy (IR) was also performed on this sample. Average particle sizes were calculated from transmission electron microscopy (TEM).

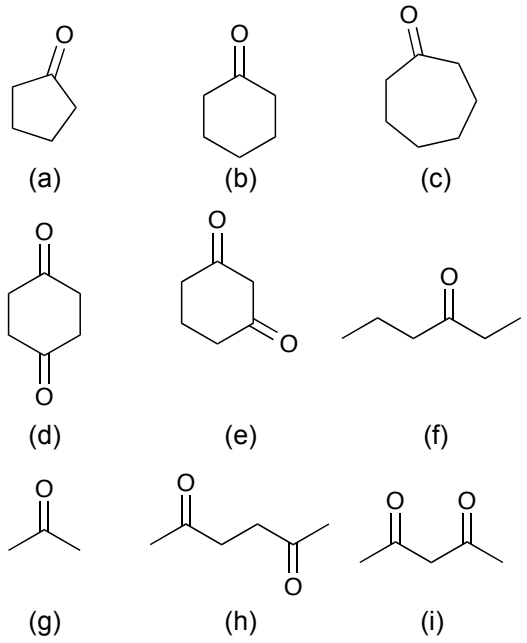

Figure 3.2: *Ketones applied in synthesis of gold colloid: (a) cyclopentanone (b) cyclohexanone (c) cycloheptanone (d) 1,4-cyclohexanedione (e) 1,3-cyclohexanedione (f) 3-hexanone (g) acetone (h) 2,5-hexanediketone (i) acetylacetone.*

The reaction was scalable, and performed on a $1/10$ scale with water (0.95 mL) and $HAuCl_4$ stock solution (0.04 mL, 0.26 μmol), and either cyclohexanone (0.05 mL, 0.48 mmol) or 2,2,6,6-tetramethyl-cyclohexanone (0.07 mL, 0.45 mmol). It was also repeated at various scales under nitrogen, with solvents having been degassed by bubbling with N_2 for an hour. Methanolic mixtures were made with 0.22 mL of a stock 12.7 mM $HAuCl_4$ solution, in 9.5 mL of MeOH. Cyclohexanone or cyclopentanone (0.5 mL) was then added and dissolved in the MeOH.

3.3 AUNP CHARACTERISATION AND DISCUSSION

3.3.1 *Spectrascopic results*

Cyclopentanone, cyclohexanone and cycloheptanone were mixed with dilute $HAuCl_4$, with very different results for each. The latter two went from

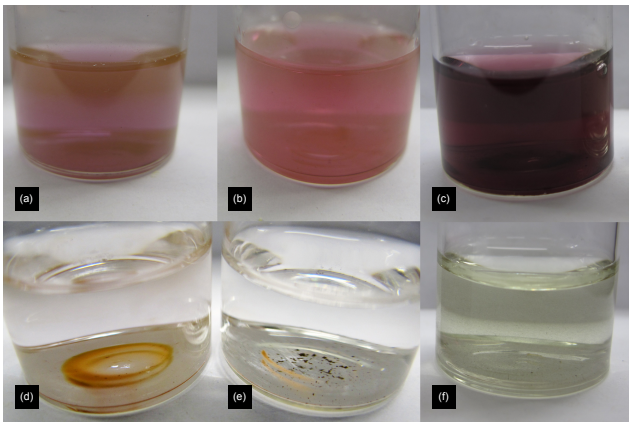

Figure 3.3: *Images of nanoparticles/precipitates at 24 hrs, synthesised with a) cyclopentanone, b) cycloheptanone, c) 1,4-cyclohexanedione, d) 3-hexanone, e) acetone and f) 1,3-cyclohexanedione.*

colourless to a purple/orange colour over the course of one hour, however cyclopentanone took 1.5 hours to start changing colour and then proceeded to darken in colour (by eye) for a further 5 hours. The final colours for cyclopentanone and cycloheptanone are shown in Fig. 3.3a & b. The position and intensity of the SPR band for each reaction was followed by UVVis in-order to estimate reaction time. Samples of the reaction mixture were deposited on TEM grids at various stages throughout the reaction for the purposes of imaging the particle growth and sizing.

It was found that the reaction for cyclopentanone proceeded much more slowly than for any other cyclic ketone used, taking 13 hours to go to completion (Fig. 3.4), with a final SPR position of 570 nm. In contrast cycloheptanone reacted slightly more quickly than cyclohexanone, taking 50 minutes, instead of 1 hour, with a final SPR position of 541 nm. The low solubility of cycloheptanone in water meant that an oily, gold-coloured film formed on the surface of the reaction. Unfortunately, the low optical transmittance of the inhomogeneous mixture meant that UVVis data were harder to collect, due to a moving baseline, making it harder to clarify the exact end point.

The next pair of ketones to be investigated were diketone versions of cyclohexanone - 1,4- and 1,3-cyclohexanedione (Fig. 3.2d & e). These diketones gave very different results in comparison to cyclohexanone. Both were more water soluble, and on mixing with $HAuCl_4$, 1,4-cyclohexanediktone formed a straw colour solution that rapidly darkened to a rich purple colour

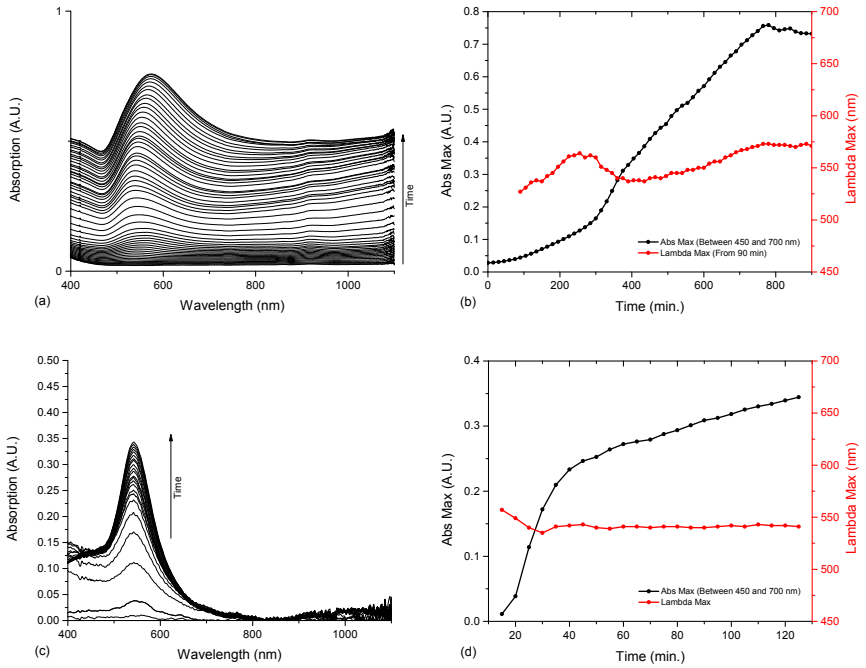

Figure 3.4: *UVVis spectroscopy and analysis of the reactions between $HAuCl_4$ and cyclopentanone and cycloheptanone. (a) UVVis absorption of cyclopentanone AuNPs between 0 and 810 minutes, at 15 minute intervals. (b) Development of SPR band in UVVis spectrum of cyclopentanone AuNPs. Maximum absorption (Abs Max) is measured between 450 and 700 nm, and the position of the SPR band maximum from its appearance at 90 minutes. (c) UVVis absorption of cycloheptanone AuNPs, with baseline corrected to zero at 850 nm, and data smoothed with moving average. These modifications remove the natural increase in baseline observed but correct for the inhomogeneity of the solution. (d) Development of SPR band in UVVis spectrum of cycloheptanone AuNPs. Abs Max is measured between 450 and 700 nm. Data plotted from 15 minutes.*

(Fig. 3.3c). Following the reaction by UVVis implied that it was complete in under 30 minutes (Fig. 3.5) with a final SPR maximum at 536 nm.

The diketone 1,3-cyclohexanedione produced an even more unusual result - after less than a minute the colourless solution had turned grey/yellow, and did not change again (Fig. 3.3f). Following the reaction by UVVis showed growth of an SPR band at 800 nm (Fig. 3.5) implying large, or at least anisotropic, particle growth.

As cyclic ketones produced such interesting results, linear equivalents were also explored. Acetone was experimented with as the simplest ketone, but very little production of AuNPs was observed (Fig. 3.3e), and no UVVis or TEM data could be obtained. 3-hexanone was employed as a linear equivalent to cyclohexanone, and some orange precipitate was formed after 24 hours (Fig. 3.3d) but no particle suspension was formed. It is suggested that

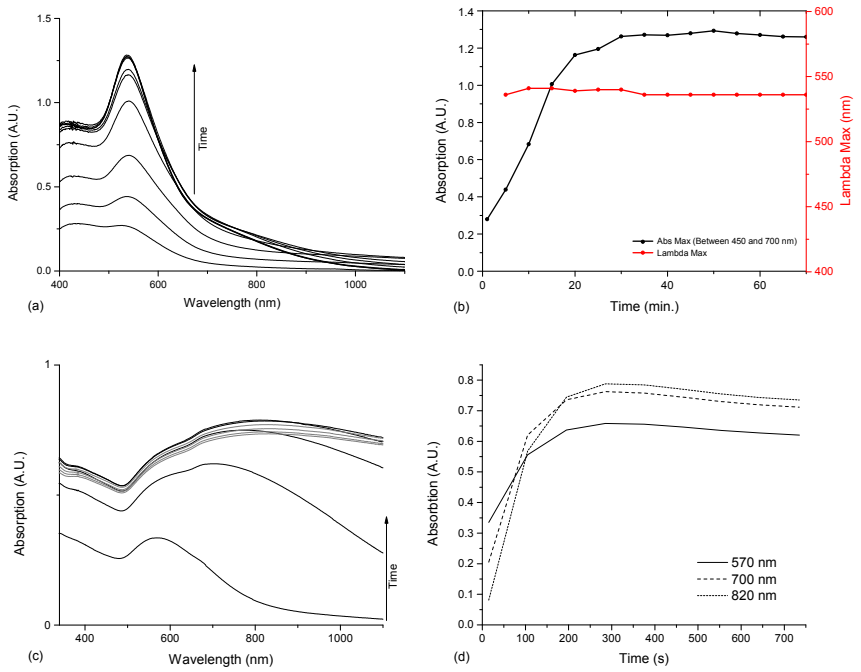

Figure 3.5: *UVVis spectroscopy and analysis of the reactions between $HAuCl_4$ and 1,4-cyclohexanedione and 1,3-cyclohexanedione. (a) UVVis absorption of 1,4-cyclohexanedione AuNPs between 0 and 45 minutes, at 5 minute intervals. (b) Development of SPR band in UVVis spectrum of 1,4-cyclohexanedione AuNPs. Maximum absorption (Abs Max) is measured between 450 and 700 nm, and the position of the SPR band maximum from its appearance at 5 minutes. (c) UVVis absorption of 1,3-cyclohexanedione AuNPs between increasing between 15 and 375 seconds (black) and decreasing from 375 to 735 seconds (grey) (d) Development of 570, 700 and 800 nm absorptions in UVVis spectrum of 1,3-cyclohexanedione AuNPs.*

although reduction to gold was taking place, these ketones proved to be poor surfactants, preventing the formation of a stable colloidal suspension.

Two linear di-ketones were used as analogues to the cyclic hexanediones. 2,5-hexanediketone was an analogue for 1,4-cyclohexanedione, but reacted much more slowly, and produced a dark purple precipitate after 12 hours, with a weak SPR maximum of 555 nm (Fig. 3.6). However several peaks were visible in the UVVis. A linear analogue for 1,3-cyclohexanedione chosen was acetylacetone (as in Kundu *et al.*). On mixing with $HAuCl_4$ a bright red colour immediately developed, darkening for approximately 3 minutes, then reaching equilibrium. This reaction was too fast to follow by UVVis satisfactorily, but did confirm that the SPR peak did not grow after 5 minutes, settling at 526 nm (Fig. 3.6).

Results from all the ketones, along with some key data, are summarised in Table 3.1, and this is presented in Section 3.3.4 on page 40.

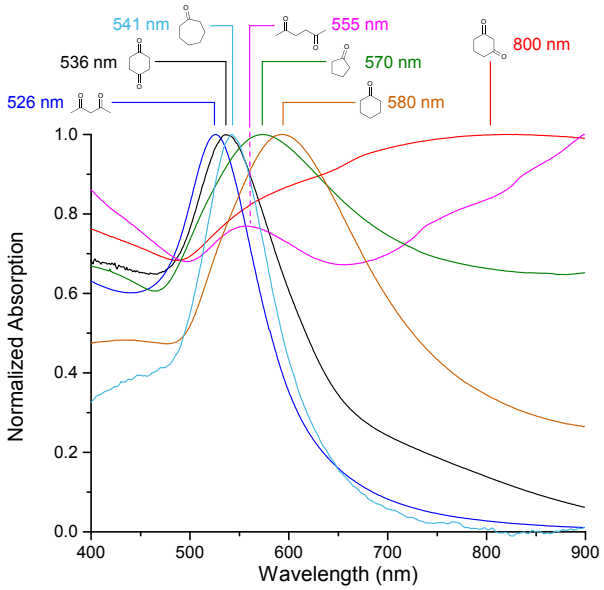

Figure 3.6: *Summary of the position and shape of the SPR bands from the colloidal suspension of AuNPs produced with each ketone.*

3.3.2 *Particle morphologies*

TEM microscopy was performed on all samples to examine the final morphologies.

The slow formation of particles in the cyclopentanone reaction could also be followed over several hours (Fig. 3.7). Initially clusters of small seed particles form, so called 'nano-pompoms', which then grow and split to eventually give a reasonably monodisperse colloid, approximately 21 nm in diameter. Cyclohexanone is described by Uppal *et al*. as having a similar growth pathway, and produced larger AuNPs, on average around 43 nm in diameter, however this mixture contained a greater number of nanoplates than observed for cyclopentanone. Cycloheptanone produced a highly amorphous mixture of structures, as shown in Fig. 3.8, with an average size of 21 nm, but a massive standard deviation of 27 nm.

The stability of the AuNPs produced from cyclic ketones was investigated by re-imaging the samples after 3-4 months. Both cyclopentanone and cyclohexanone showed a dramatic increase in the number of thin triangular plates (Fig. 3.7f), suggesting that the surface of the AuNPs is not well passivated by the ketones. Interestingly very little shift was seen in the SPR maximum, but it was reduced in intensity.

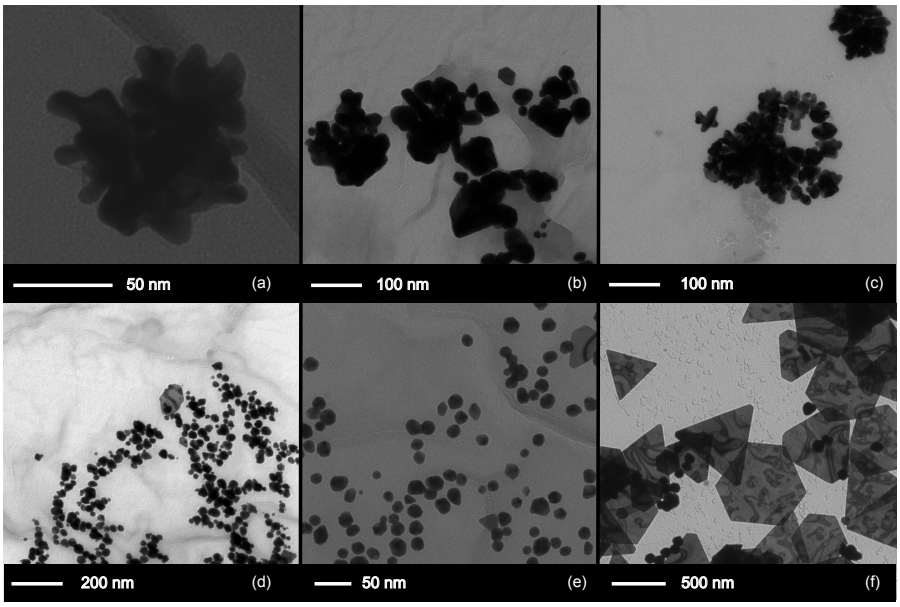

Figure 3.7: *TEM micrographs of particle growth in a mixture of cyclopentanone and $HAuCl_4$. Samples were collected at a) 10 minutes, b) 90 minutes, c) 180 minutes, d) 240 minutes, e) 24 hours and f) 3 months.*

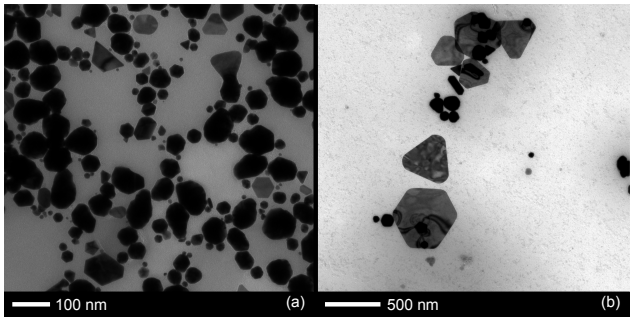

Figure 3.8: *TEM micrographs of particle growth in a mixture of cycloheptanone and $HAuCl_4$. Samples were collected after around 2.5 hours of particle growth and show a) a large variety of different particle sizes and b) several types of thin plate.*

TEM of the 1,4-cyclohexanedione particles showed monodisperse 20 nm particles with no nanoplates (Fig. 3.9a), and it became apparent that 1,3-cyclohexanedione unusually formed large (*ca.* 250 nm) pointed nanostars - Fig. 3.9b, explaining the broad, redshifted UVVis spectrum.

For the linear ketones, no particles were imaged for acetone, but for 3-hexanone a few particles could be imaged, proving to be very large; on average 139 nm.

The particles formed with 2,5-hexanediketone were a mixture of small particles of about 22 nm diameter, and amorphous plates, and the red acetylacetone solution contained a mixture of small amorphous and more con-

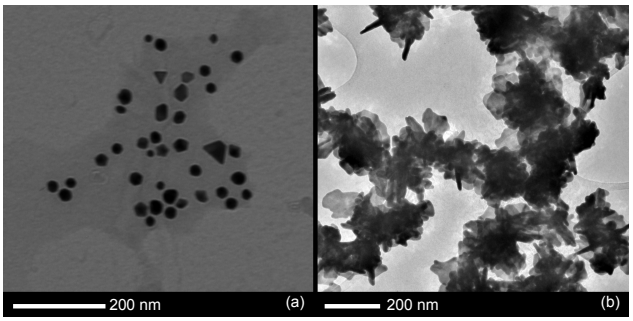

Figure 3.9: *TEM micrographs of particle growth in a mixture of a) 1,4-cyclohexanedione or b) 1,3-cycloehexanedione and $HAuCl_4$.*

ventional particles, with an average diameter of 13 nm, which is similar to the 10 nm particles reported by Kundu *et al*.[167]

3.3.3 *XPS and IR characterisation*

The AuNPs produced were freeze dried to remove the solvents and examined with XPS and IR. XPS measurements of the Au $4f_{7/2}$ and $4f_{5/2}$ peaks are given in Fig. 3.10 on page 38. For samples produced with cyclohexanone, cycloheptanone and the cyclohexanediones there was good agreement between the $4f_{7/2}$ and $4f_{5/2}$ peaks with expected values (83.9 and 87.7 eV). Similarly the linear ketones, acetone and 3-hexanone had a good match to the expected Au^0 and Au^{3+} peaks, however the acetone residue contained a far larger proportion of Au^{3+} than the 3-hexanone sample, implying an incomplete reaction after 24 hours.

Cyclopentanone produced AuNPs, showing $4f_{7/2}$ and $4f_{5/2}$ peaks similar to those samples containing Au^{3+}. The peaks were also very broad. As the reaction time for this ketone was so long (13 hours) it is likely that there was still trace Au^{3+} present and this lead to the shift and the broadened peaks. A similar pattern was observed for acetylacetone, in this case suggesting that the particles formed so quickly that perhaps Au^{3+} was trapped in the material.

Data for 2,5-hexanediketone implied that it also contained a mixture of Au^{3+} and Au^0, in a similar fashion to cyclopentanone, however the quality of the spectrum was poor , so this may account for the shifting of the signals.

IR data are shown in Fig. 3.11 on page 39 with indications of the usual ranges for ketone C=O and C−Cl stretches. Many of the samples show shifts to their expected carbonyl stretches, implying binding to the Au surface, and some samples show the presence of C−Cl stretches, although these are often weak.

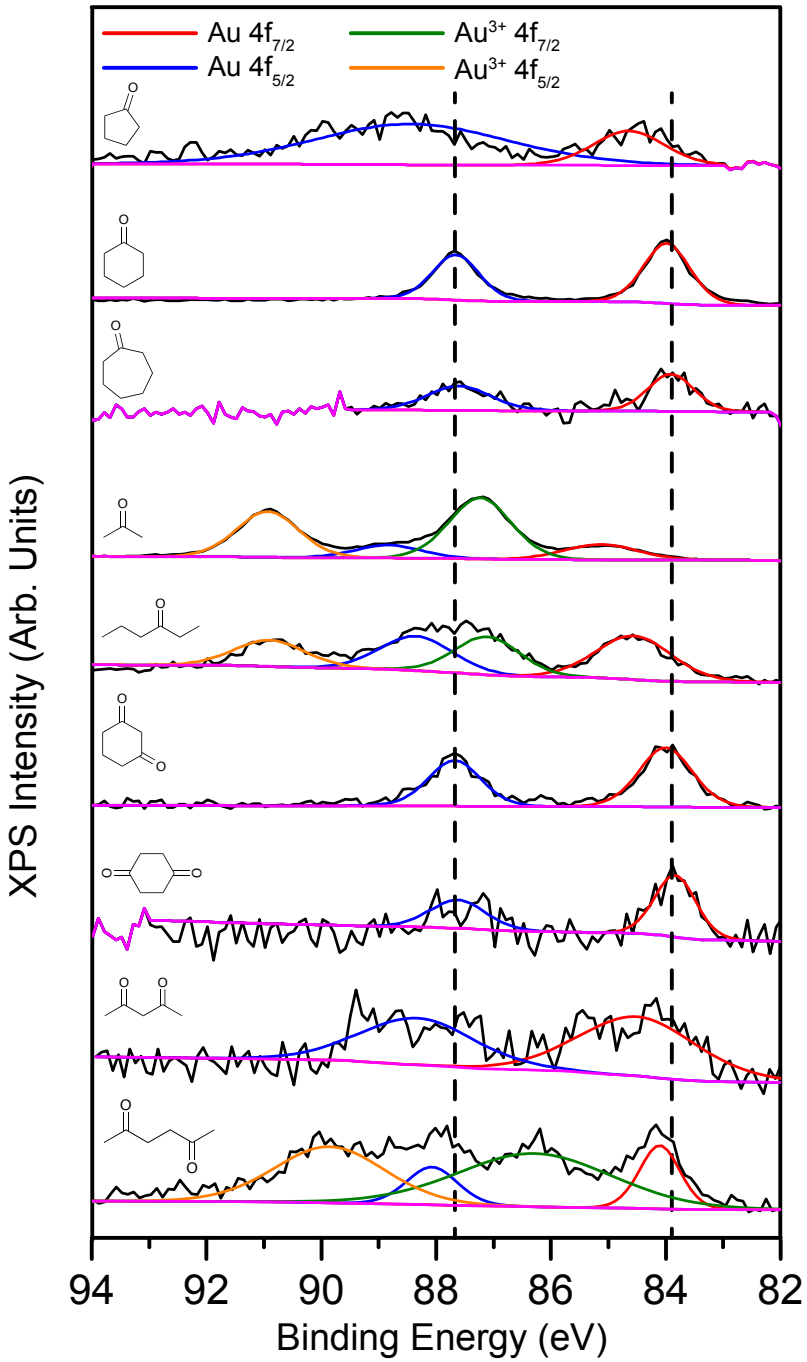

Figure 3.10: *XPS data collected for the 4f Au peaks of AuNPs generated from reaction with the ketones shown. Dashed lines show the positions of the ideal $4f_{7/2}$ and $4f_{5/2}$ peaks for Au^0.*

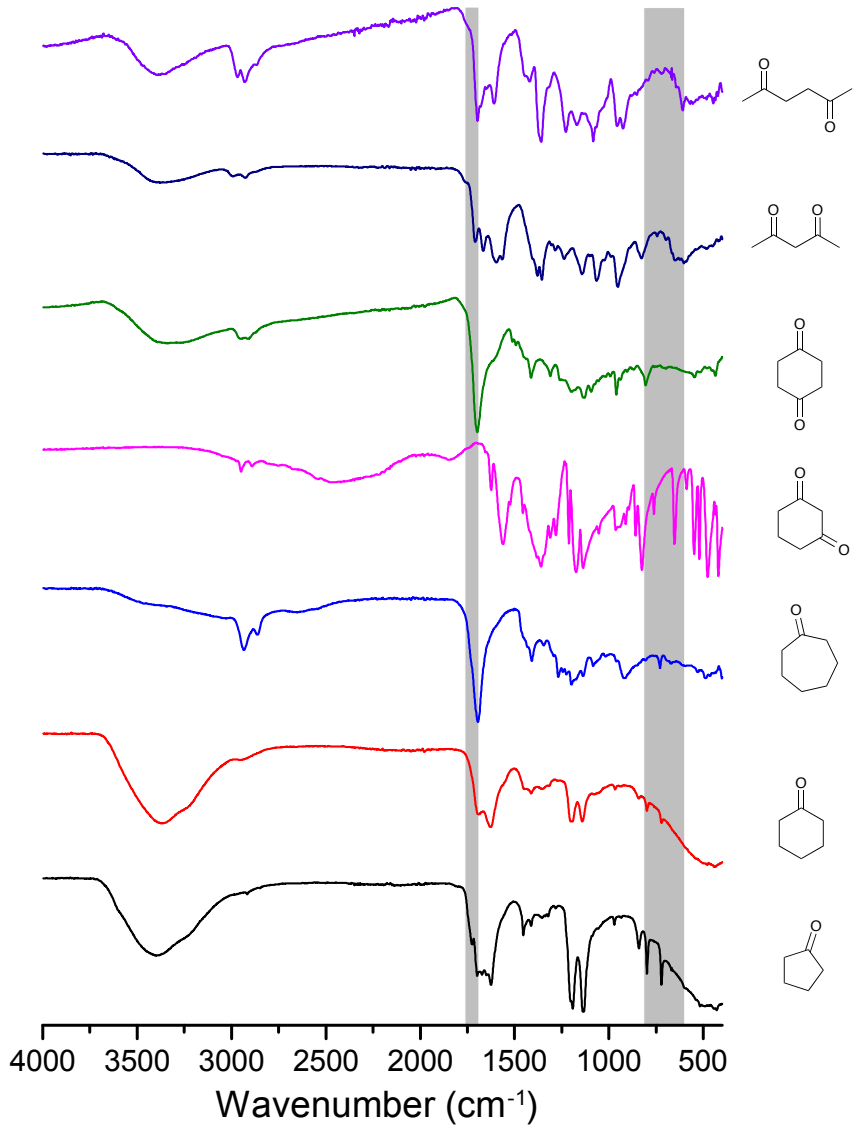

Figure 3.11: *IR data for a selection of ketone-produced AuNPs, indicated by each line. The grey bars are the usual wavenumber ranges for ketone carbonyl stretches (1700-1750 cm^{-1}) and C-Cl stretches (600-800 cm^{-1}). Data for acetone and 3-hexanone were of too low quality to plot.*

3.3.4 *Discussion of Mechanism*

There were several trends in the series of ketones studied. Cyclic ketones proved to be far better at producing and stabilising the AuNPs in solution, whereas linear ketones often gave poor results. Diketones however were far better in both cyclic and linear forms at stabilising the nanoparticles, and reacted far more quickly. This increase in rate is attributable to both an increased number of reactive ketone sites, and in the case of β-diketones, the highly reactive α-proton between the two ketones creating a larger proportion of the enol form, tallying with the suggest mechanism of Uppal *et al.*[175]

Table 3.1: *Summary of growth rate and morphology control exerted by various ketones related to their solubility and enol content. Enol content is expressed as pK_E and data are extracted from Keeffe et al.[176]*

Ketone	Solubility (mg ml^{-1})	pK_E	Reaction Time	Average Particle Size (nm±SD)
Acetylacetone	160	0.64	$<$ 5 min	13±9
1,3-Cyclohexanedione	soluble	5.26	∼5 min	nanostars (∼250)
1,4-Cyclohexanedione	soluble	$<$6.38	30 min	20±5
Cyclohexanone	90	6.38[176]	1 hour	43±7
2,5-Hexanediketone	100	7.51	12 hrs	22±7
Cyclopentanone	9	7.94[176]	13 hrs	21±7
3-Hexanone	15	∼7.43	$>$ 24 hrs	139±12
Cycloheptanone	$<$1	8.00[176]	50 min	21±27
Acetone	miscible	8.33[176]	$>$ 24 hrs	-

The relationship between the enol content of each ketone (given as $pK_E = -log_{10}(\frac{[enol]}{[ketone]})$) and the rate of reaction and AuNPs produced was of great mechanistic interest. It can be seen in the log-log plot Fig. 3.12 that there is a good linear trend, especially when allowing for estimates in reaction time for the slower reactions.

These data correspond very well with the suggested mechanism, given in Scheme 3.1, whereby the gold is reduced via reaction of $HAuCl_4$ with the enol form of the ketone under acidic conditions to give Au(I). This then disproportionates to give Au(0) and Au(III) again. The greater the availabil-

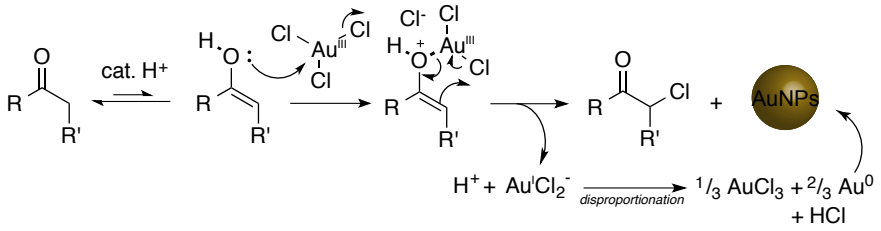

Scheme 3.1: *Suggested reaction mechanism for the production of AuNPs with a ketone moiety and chloroauric acid. The acid catalyses tautomerism to the enol form, followed by a chloride transfer to promote reduction of Au^{3+} to Au^{+} as $AuCl_2^-$. This then undergoes a disproportionation, catalysed by any native gold present, to a mixture of Au(0) and Au(III), nucleating the gold nanoparticles. R and R' can be connected or different (e.g cyclopentanone R-R' = -$CH_2CH_2CH_2$-, or acetone R=CH_3, R'=H)*

ity of the enol, the faster the reaction will proceed. Other evidence includes the incomplete reaction after 24 hrs of acetone, in keeping with its larger pK_E, and some tentative IR evidence suggesting $-$Cl insertion next to the carbonyl as suggested by the mechanism (Scheme 3.1).

There are, however, two clear outliers in Fig. 3.12. The first is acetylacetone, with it's very small pK_E and unreliably measured short reaction time. The second is cycloheptanone. The latter's fast reaction time in comparison to it's large pK_E is attributed to poor solubility of cycloheptanone in water, causing several different nucleation and ripening processes to occur in droplets of cycloheptanone, or at the cycloheptanone-water interface. This would also account for the erratic particle formation.

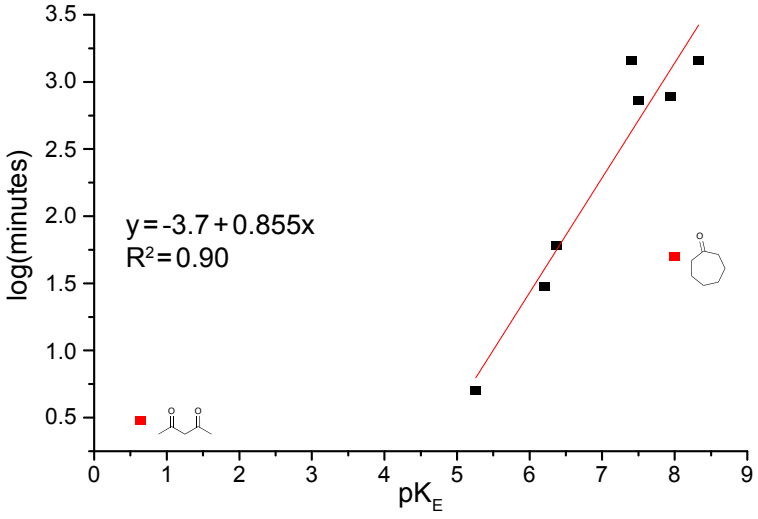

Figure 3.12: *Graph of log(reaction time) against pK_E showing a linear trend with two clear outliers (in red).*

Two other reactions were carried out in addition to those described above to test this mechanistic theory. Firstly the reactions with cyclohexanone and cyclopentanone were carried out in methanol rather than water. This should have greatly lowered enolization of the ketone, *via* reduction in the number of acidic protons in solution, and as expected no reaction was observed over a period of a week. The second experiment used 2,2,5,5-tetramethylcyclohexanone (synthesised in house using the method of Lissel,[177] and purchased from Sigma Aldrich) - this ketone is fully blocked at the α-positions, and thus should not be able to form an enol in water. On mixing, the reaction did eventually take on a pink colour, however it took much longer than the usual hour to attain this colour. A suggestion as to why a reaction still occurred is that it was due to trace amounts of tri and di-methyl ketone mixed with the tetra-methyl, due to the difficulties in synthesis and fractional distillation of the molecule. These then allowed some enol formation and thus some reduction of the Au^{3+} occurred.

An interesting anomaly was the formation of nanostars with 1,3-cyclohexanedione compared to the small particles produced with comparable molecules acetylacetone or 1,4-cyclohexanedione. This is attributed to the lack of conformational flexibility in the cyclic β-diketone, when compared to acetylacetone, resulting in very different ligation properties to the surface of the formed nanoparticles. This might alter the surface growth pattern. The 1,4-cyclic-diketone has its ketone groups spread so far apart that it is highly unlikely that it could act as a bidentate ligand on the surface, like acetylacetone or 1,3-cyclohexanedione. However it may act as a bridging monodentate ligand, bringing smaller Au seed particles together to rapidly form the colloid observed. The Au nanostars produced with 1,3-cyclohexanedione also appear to possibly be polycrystalline in the TEM images, and this should be further investigated.

3.4 SERS SENSING

The next challenge was to apply the synthesised nanoparticles to sensing. As discussed in Section 2.3.4, gold nanoparticles can be applied in Raman

sensing to enhance the signals through plasmonic resonance interactions of surface bound species - SERS. The aim was to measure SERS enhancement of a nitroaliphatic compound (explosive taggant DMDNB) using the nanostructures fabricated. In particular the nanostars are of great interest, due to the supposed high enhancement effect of sharp tips (Fig. 3.13).

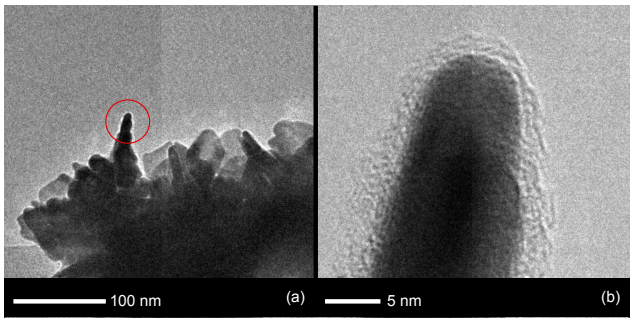

Figure 3.13: *TEM micrograph of partial gold nanostar (a) and close up of one tip (b) with approximate diameter of 5 nm.*

3.4.1 *Raman setup*

Raman spectra were collected with a Renishaw multi-line Raman microscope with excitation at 785 nm. A 50× optic was used to collect data. Samples were prepared either in solution, with focus set at the top of the solution, or by depositing small drops ($\sim$ 5 μL) of the AuNP solutions onto glass substrates. The dropped solutions were either pre-mixed with the analyte of choice, or deposited and then over-coated with analyte.

The Raman microscope can, in theory, be used to measure Raman spectra of solutions or solid samples, and both were attempted. The advantages of solution measurements are the ease of concentration control and rapid sample preparation. However, it was found that without an immersible optic, obtaining good focus on the surface of the solution was impossible as the laser evaporated the water faster than a scan could be completed. Drop casting and co-drying the nanoparticles onto a surface with an analyte was then tested on glass substrates. Analyte introduction was either with premixing (to give a final analyte concentration of either 0.5 mM or 0.1 mM) and then depositing a 5 μL drop of the mixture; or by depositing a 50 μL drop of

nanoparticles, drying and then over coating with a 5 μL drop of analyte (1 mM).

The Au nanostars synthesised with 1,3-cyclohexanedione were irradiated with 785 nm light, in order to stimulate the samples' plasmon resonance.

3.4.2 *Results*

When solutions of the Au nanostars were drop-cast with DMDNB, no obvious SERS signal was observed - Fig. 3.14. What was seen, was a very strong signal for the 1,3-diketone, and examination with SEM showed that enough of the starting material was in solution to crystallise with the nanoparticles, and cause this strong signal. There were some alterations from the pure starting material spectrum, implying some preferential orientation of the diketone. This may possibly indicate SERS enhancement of certain resonances of the nanoparticle capping molecules, locked in position on the particle surface, but is hard to prove categorically, and the effect may just be due to recrystallisation of the excess starting material into a different phase. The carbonyl stretching band at *ca.* 1500 cm^{-1} was sought to further investigate this observation, but was obscured by glass fluorescence.

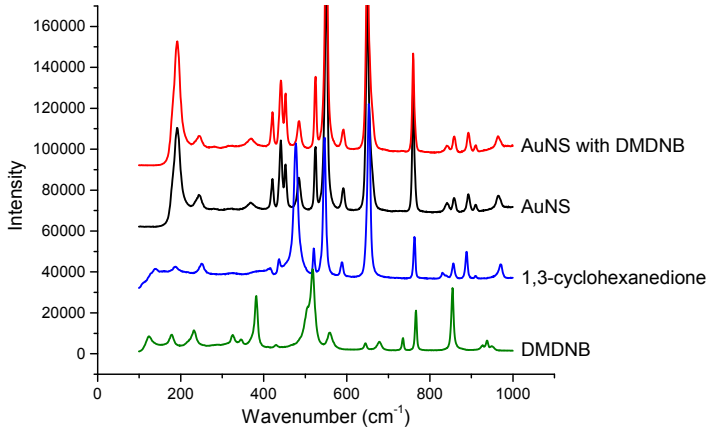

Figure 3.14: *Raman spectra of dropcast gold nanostars (AuNS) from 1,3-cyclohexanedione (5 µL) with final concentration of DMDNB at 0.5 mM. Reference spectra of pure DMDNB and 1,3-cyclohexanedione given.*

In an attempt to purify the nanostars, ultracentrifugation was applied, but no pellet could be isolated, probably due to the very low concentration of nanostars in solution.

3.5 CONCLUSIONS

A new selection of gold nanomaterials have been synthesised with a room-temperature, self-initiating process, utilising ketones as the reducing agent. A suggested mechanism has been probed by spectroscopy, electron micrcoscopy, and experimental design, and tied to the availability of the α-proton of the ketone. The different ketones offered the potential to create interesting particle morphologies, and one of these samples, the gold nanostars, was applied to attempt plasmon enhanced Raman spectroscopy, with sadly limited results.

New ways of cleaning the gold nanostars whilst maintaining their sharp features must now be found, so that better SERS data can be obtained. Kinetic analysis of the reaction would also be of interest to determine the order of the process. In the meantime, a separate project was initiated to study the fluorescence sensing of explosives utilising quantum dot (QD) nanoparticles.

4

QUANTUM DOT SYNTHESIS

4.1 RATIONALE

4.1.1 *System design*

The aim of this work was to develop a solution phase fluorescent sensor based on quantum dots (QDs). This will differ from existing sensors for explosives using quantum dots, because the surface receptors will be designed around a variety of macrocyclic and linear electron donors to capture the analytes, and most importantly a multicoloured array will be created, utilising the narrow fluorescence emission bands QDs to create a multichannel sensor array (demonstrated in Chapter 5).

These surface receptors are designed to bring the explosive close to the QD, facilitating a photoinduced electron transfer (PET) process, which will quench the observed fluorescence, as described in Section 2.3.5. This chapter describes the synthesis of ligands and QDs designed for this purpose, the methods of attachment to the surface of the QD, and their characterisation.

4.1.2 *Supramolecular binding*

When trying to construct a chemical sensor system, the interaction between the sensor element and the analyte must be designed to give sensitivity and specificity, but should ideally be reversible (non-covalent). When controlling supramolecular chemical reactions like this, chemists can look to several bonding modes: hydrogen bonding, dispersion forces, electrostatic forces, metal coordination, π-π interactions or hydrophobic/hydrophilic interactions.

Of particular interest in this field are macrocycles - pre-organised, large, cyclic molecules that can bind a guest in their central cavity, without the need for significant rearrangement. This reduces the enthalpic and entropic penalty to molecular association, in particular reducing the negativity of the entropy, ΔS, resulting in a good, negative, ΔG (Eqn. 4.1). In addition to this the internal cavity of macrocycles is often poorly solvated, and thus they have low energy barriers to host binding (a more negative enthalpy, ΔH). Furthermore, the internal and external faces of a macrocycle can have opposite hydrophobicities, creating a driving force (a more negative enthalpy, ΔH) to trap hydrophobic or hydrophilic species in the cavity, dependant on the macrocycle and solvent.

$$\Delta G = \Delta H - T\Delta S \tag{4.1}$$

Conventional military explosives - nitroaromatics or nitroaliphatics - have features that can be targeted to induce supramolecular binding. Both classes are very hydrophobic, and are good electron acceptors and in particular, the nitroaromatics are known to form strong π-π bonds with electron rich aromatic species.[72]

To target these features, three classes of macrocycle will be used, shown in Fig. 4.1, along with simple nucleophilic electron donors and electron rich π systems.

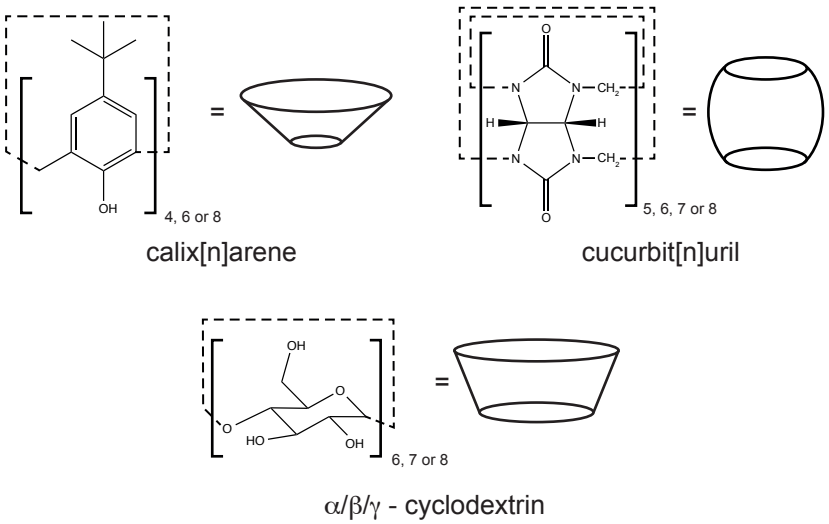

Figure 4.1: *Cavitand structures and shapes for calix[n]arene, cucurbit[n]uril and cyclodextrin.*

Cyclodextrins are cyclic amyloses, that self order into a cone like shape with a larger and smaller portal. All three common sizes - α - 6 membered, β - 7 membered and γ - 8 membered cyclodextrin - have been used as sensor molecules widely and shown to interact favourably with explosives.[178] The smallest, α-cyclodextrin, was applied in the dendrimer based detection system of Algarra *et al.*[134] The larger sizes of cyclodextrin have more favourable cavity sizes for binding small molecule explosives (see Table 4.1) and have been utilised in mass spectrometry (MS) based detection of explosives and for soil extraction.[179, 180] A final example of the use of cyclodextrins for explosives detection is the work of Ponnu *et al*. who used fluorophores or dyes with fluorescence and UV-visible spectroscopy to measure incorporation of explosives (including TNT, RDX and tetryl) into the cavities.[181, 182]

Cucurbituril is a more recently developed cavitand (although first discovered in 1905 it was not characterised until 1981) featuring two symmetrical portals lined with urea carbonyls, surrounding a hydrophobic cavity (for dimensions see Table 4.1).[183] The easiest sizes to access are created from 5-8 unit oligomers of glycoluril.[184, 185] In the last 10 years major advances have been made into the functionalisation of cucurbituril, making it a more useful starting material for synthetic chemists to work with.[186, 187] There have been two ways of doing this. The first involves creating functionalised glycoluril monomers and incorporating them into the cucurbituril ring.[188–191] A second, more direct route, has been to modify preformed cucurbiturils by oxidising them and using the OH group to attach a range of functionality.[192–194] In 2011 Cui *et al*. demonstrated the first attachment of cucurbituril to a QD *via* direct attachment, using a small thiol linker, however they use multiple points of attachment, giving a range of products in their system, with lack of full synthetic control, and used cucurbit[6]uril, whose cavity is too small to bind many analytes of interest.[195] Recently Zhu *et al*. have applied cucurbit[8]uril with great success to explosives detection, showing that it is possible for the cavity to contain a fluorescent probe molecule and explosive analyte, in much the same way as Ponnu's cyclodextrin systems, however they have not yet utilised a QD as the fluorophore.[196, 197]

Calixarenes are slightly smaller cavitands and differ from the above systems in several ways. Some exemplar dimensions are listed in Table 4.1, but cavity volumes are less well defined than for the cavitands described above, and only one portal is open for binding, the other being closed by H-bonded hydroxyl groups. Most importantly they are comprised of cyclised arenes, and thus introduce the possibility of π-π interactions. They have been applied to sensing *via* QD attachment for a range of analytes including pesticides and neurotransmitters.[139–143, 145, 198, 199] However, in each of these cases attachment has been *via* one face of the calixarene cavitand, using small thiolated linkers, closing off one face for binding and limiting the control over the system assembly. One good example of the application of calix[4]arene to explosives detection is described by Lee *et al.*[200] They have modified a basic calixarene with two fluorescent pyrene moieties and shown interaction with a range of nitroaromatics. The small size of calix[4]arene means that it is potentially more suitable for ions rather than small molecules, so it may be necessary to look at calix[6] and [8]arene to achieve good binding with the target analytes. However if binding is not achieved, then calix[4]arene may prove a useful discriminating element in the final array.

Table 4.1: *Some dimensions of three explosive analytes and three classes of cavitand. Explosive sizes from [197], cyclodextrin sizes from [201], cucurbituril sizes from [202] and calixarene sizes from [203].*

Material	Size	Edge or Portal size (Å)	Volume (Å^3)
RDX	-	6.91×6.28×4.74	152.51
PETN	-	8.82×9.14×6.80	244.69
TNT	-	7.91×7.83×2.85	167.75
Cyclodextrin	α	4.7, 5.3	174
	β	6.0, 6.5	262
	γ	7.5, 8.5	427
Cucurbituril	[6]	3.9	164
	[7]	5.4	279
	[8]	6.9	479
Calixarene	[4]	3.0	-
	[6]	7.6	-
	[8]	11.7	-

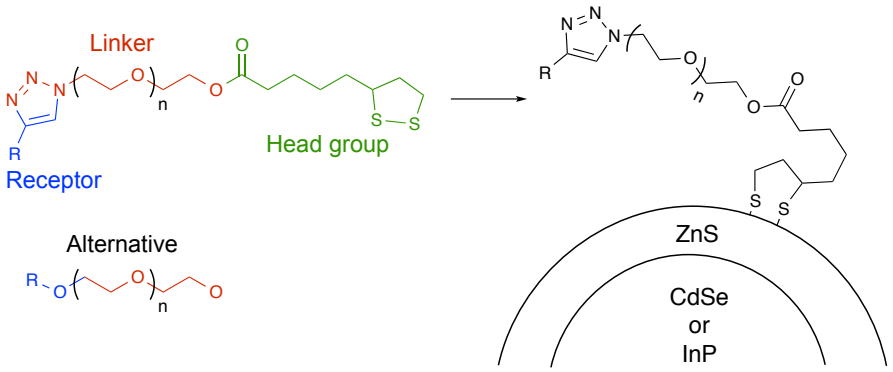

Scheme 4.1: *Scheme of ligand design and applicaton to a QD, featuring the LA headgroup, linker (n= 2, ∼6 or ∼8), and receptor end group (either azide click or nucleophilic addition/substitution).*

4.2 SYSTEM SYNTHESIS AND CHARACTERISATION

A modular approach was taken to the synthesis of receptors for the QD surface, extending the work pioneered by Mattoussi and Meditnz.[204–206] A lipoic acid (LA) head group was attached *via* a solubilising polyethylene glycol linker to a receptor end group. The head group was chosen as it facilitated a simple photoinduced ligation process to functionalise the QDs.[207] The polyethylene glycols ensured solubility in polar solvents such as methanol, ethanol or water. In order to attach the generic head group and linker, either amide, ester or Huisgen azide-alkyne click coupling was used.

The receptors were designed to present a wide variety of supramolecular binding possibilities, using cavitands, aromatic or nucleophilic-heteroatom based interactions to target hydrophobic and strongly electron-accepting explosives. In order to couple each receptor to an azide-terminal linker, synthesis of a monopropargyl version of each was attempted. Where this proved challenging, or other routes were simpler, a carboxylic acid form was synthesised if possible.

Three cavitands (reviewed above) were trialled; calix[4]arene, β-cyclodextrin and cucurbit[6] and [7]uril. Aromatic terminal groups based on naphthalene and dopamine were synthesised, along with simple -OH and -NH_2 terminal functionality

Presented here are the synthetic details for the head group, linkers, and each receptor, along with their assembly onto multicoloured QDs. These materials were then characterised with a range of spectroscopic techniques and applied to the fluorescence sensing of explosives. Full methodological details of all processed, organic and nanoparticle syntheses are presented in Section 8.3.

4.2.1 *PEG linker/TEG linker*

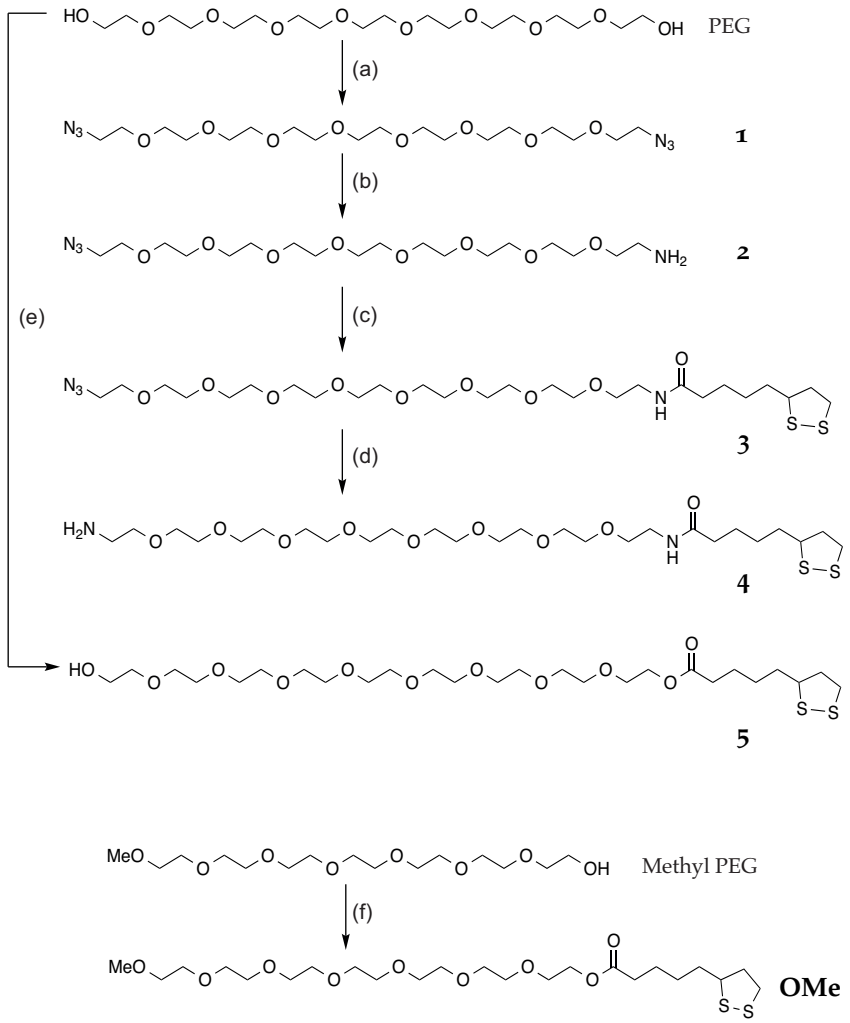

Scheme 4.2: *Scheme for PEG synthesis. (a) MsCl, TEA, THF, RT then NaN_3, H_2O, 100 °C, 74% (b) PPh_3, 1M HCl, EtOAc, RT, 65% (c) lipoic acid, DCC, DMAP, DCM, RT, 97% (d) PPh_3, H_2O, THF, 50% (e) lipoic acid (excess), DCC, DMAP, DCM, RT, 60% (f) as (c), 82%.*

A lipoic acid based linker was synthesised.[204–206] This was terminated with an azido-group to facilitate Huisgen-like cycloadditions for coupling

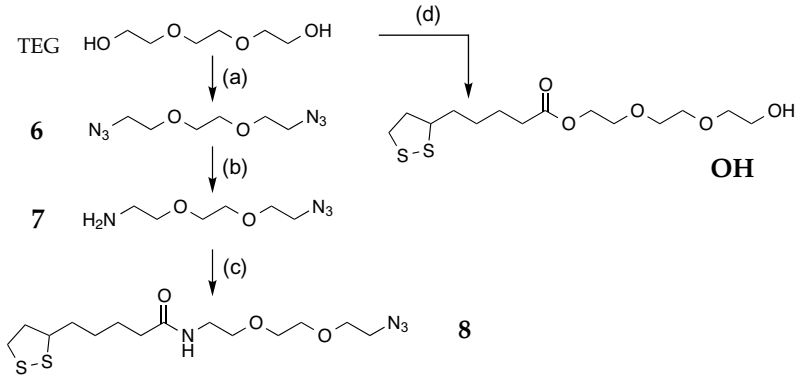

Scheme 4.3: *Scheme for TEG synthesis. (a) Mesyl chloride, triethylamine (TEA), THF, RT, (b) NaN_3, H_2O, 100 °C, then PPh_3, 1M HCl, EtOAc, RT, 65% (c) Lipoic acid (LA), DCC, DMAP, DCM, RT, 97% (d) as (b), 0.1 eq LA, 60%.*

the linker to the receptors. Because solubility was a concern, in the first instance polyethylene glycol (PEG) with an average molecular weight of 400 Da was used (this is represented as PEG, n = 9 in Scheme 4.2, but in reality is a mixture of mostly n = 9, with some polydispersity). Full synthetic procedures for the PEG's are described in Chapter 8.

Firstly a PEG bis-azide was created (**1**) which was then half reduced with a Staudinger reduction in a biphasic system, that minimised over-reduction of the azide to amine (**2**). Lipoic acid was then coupled with a standard Steglich esterification procedure to give generic linker **3**. In order to provide a 'blank' ligand to control the surface concentration of receptors, a shorter 350 Da methyl ether PEG (approximately n = 7) was coupled to lipoic acid to give **OMe**. A shorter length was chosen to try and minimise interference between the OMe-terminated PEG and the receptor cavities. As an alternative functionality to act as coupling points or as receptors themselves -NH_2 (**4**) and -OH (**5**) terminated linkers were also synthesised, as shown in Scheme 4.2. The Staudinger reduction of **3** to **4** was very low yielding in comparison to the reported literature procedure, and despite attempted optimisation, only reached a maximum of 50%.

However, it was noted that the long chain length between receptor and QD might result in poor electron transfer (and hence low quenching - see Section 2.3.5), therefore triethylene glycol (TEG) based linkers were subsequently also synthesised.

TEGs were created in a similar fashion shown in Scheme 4.3, with the same aim of creating either azido (**8**) or hydroxy (**OH**) terminal linkers for further coupling.

4.2.2 *Calixarene*

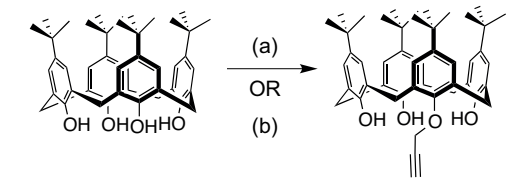

p-*tert*-butyl-calix[4]arene **9**

Scheme 4.4: *Two syntheses of monopropargyl calix[4]arene. (a) K_2CO_3, propargyl bromide, acetone, 56 °C, 24% (b) CsF, propargyl bromide, DMF, 40 °C, 28%.*

Monopropargyl calix[4]arene (**9**) was produced *via* two different methods, presented in Scheme 4.4. Initially a preparation using 0.9 eq. of K_2CO_3 in acetone as a base and an excess of propargyl bromide (2 eq.) was tried.[208] However a literature search uncovered an interesting result from Groenen *et al*. in 1991, that suggested CsF as a better base to effect the mono-deprotonation of calixarene. This is suggested to be caused by a strong F-H hydrogen bond forming, rather than complete deprotonation, limiting over alkylation.[209] They demonstrate the effect with methyl, ethyl and allyl, but not propargyl substituents, so their procedure was attempted with the suggested 10 eq. of propargyl bromide. This procedure also relied on selective precipitation for purification, which was simpler than chromatography, however the use of DMF as the solvent meant extensive washing was required. The use of CsF gave slightly better yields, but the more expensive reagents and larger excesses required may not be justifiable by the moderately increased yield. For larger scale production, K_2CO_3 in acetone was employed, but selective precipitation was used for purification, rather than chromatography.

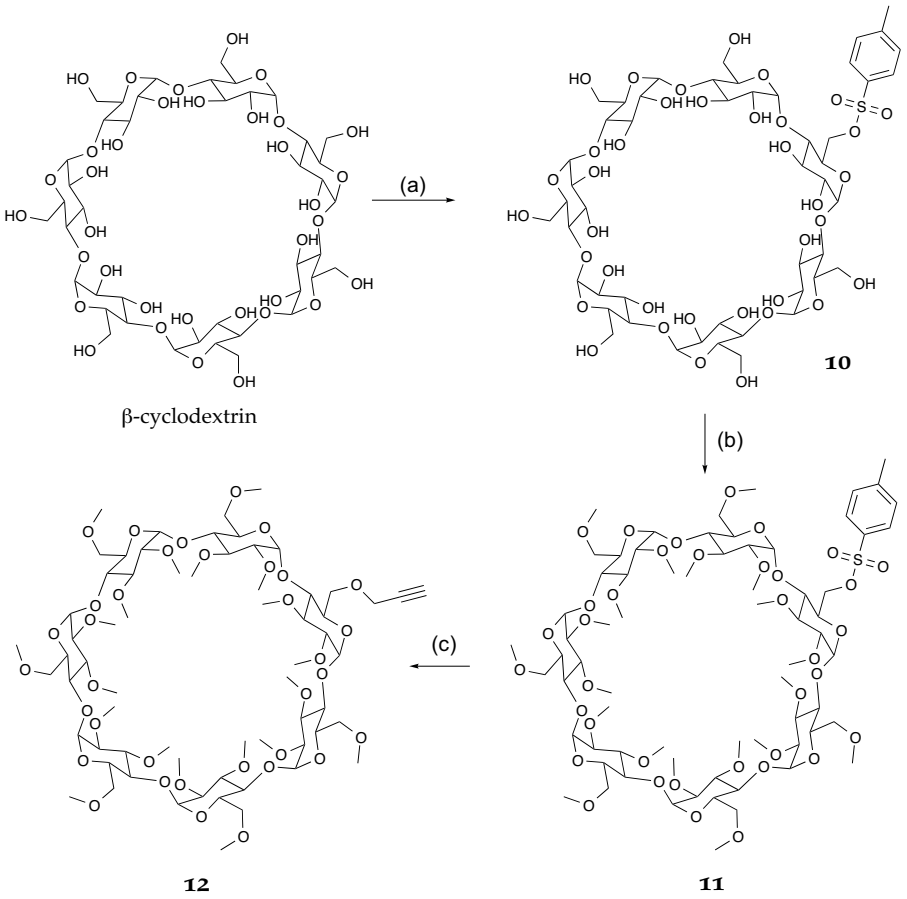

Scheme 4.5: *Synthesis of monopropargyl cyclodextrin. (a) tosyl chloride, NaOH, H_2O/MeCN, RT, 7% (b) NaH, MeI, DMF, unknown yield (c) NaH, propargyl alcohol, DMF, 50% yield by NMR.*

4.2.3 *Cyclodextrin*

Previously cyclodextrin has been attached to a QD by borane chemistry, connecting to two of the -OH groups on the portal edges.[138] However this would not allow the more general reaction scheme that was desirable, so monopropargyl cyclodextrins were desirable. Several syntheses were attempted before settling on the following procedure, modified from Faiz *et al.*[210] This method had the advantage of permethylating the -OH positions of the cyclodextrin, greatly improving solubility. However it must be noted this increase in steric bulk may reduce the cavity size, lowering the chance for binding.

Intermediate **10** was created by reacting β-cyclodextrin with *p*-tosylimidazole, and precipitation from basic solution.[211] It was then permethylated with a large excess of NaH and MeI to block all other reactive -OH positions

to give **11**. Finally the tosyl group was replaced with a propargyl group by substitution with propargyl alcohol to give the desired product **12**.

4.2.4 *Cucurbituril*

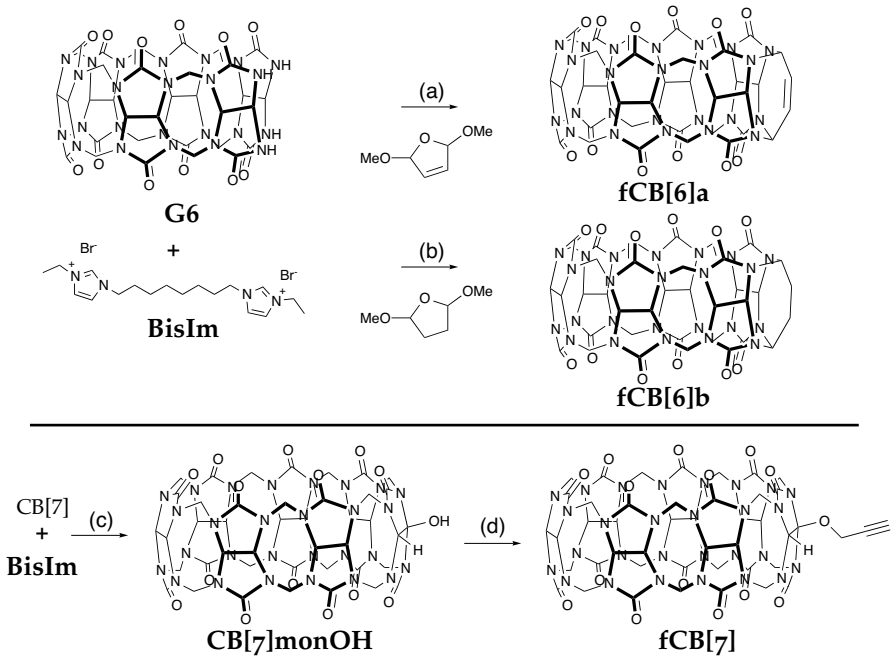

Scheme 4.6: *Synthesis of various cucurbit[6] and [7]uril derivatives. (a) glacial acetic acid, RT, 48 hrs, no reaction (b) 10% HCl, RT, 48 hrs, no reaction (c) ammonium persulfate, H_2O, 85 °C, 7.5% (d) NaH, propargyl bromide, DMSO, RT, 92%.*

The final cavitand to be attempted for use as a receptor was monopropargyl cucurbituril. As the monofunctional cucurbiturils are a relatively unexplored area of synthesis, several different approaches to monofunctional cucurbit[6]uril and cucurbit[7]uril were undertaken, with the aim of producing monopropargyl derivatives.

The first route attempted was to cyclise a linear glycoluril hexamer (**G6**, synthesised from Lucas *et al.*[190]) around a template with a 1,4-dialdehyde to form a cucurbit[6]uril with a single point of functionality for further modification. This has previously been demonstrated with 4-hydroxyphthalaldehyde.[191] In this instance it was decided to attempt to use a non-aromatic species to reduce bulk. For this purpose, 2,5-dimethoxy-2,5-dihydrofuran or 2,5-dimethoxytetrahydrofuran were selected as a protected source of dialdehyde. The former was preferred as it contained a double bond to en-

sure rigidity (helping to promote full cyclisation) and allow further functionalisation.[212] Acidic reaction conditions, either 10% HCl or glacial acetic acid were used (Scheme 4.6) and **G6** was templated around guest **BisIm** to promote cyclisation. Some reaction was observed to occur by colour change of the solution in every instance, however NMR and MS analysis of the resulting products was inconclusive. It is possible some cyclisation did occur of **G6** to CB[6], as implied by MS (Fig. 4.2), although this is more likely a molecular ion species (with Na^+). MS also suggested the possible existence of higher-mass conjugates of **G6** and the dihydrofuran with loss of water, but these peaks were insignificant, and no corroborative NMR evidence could be obtained.

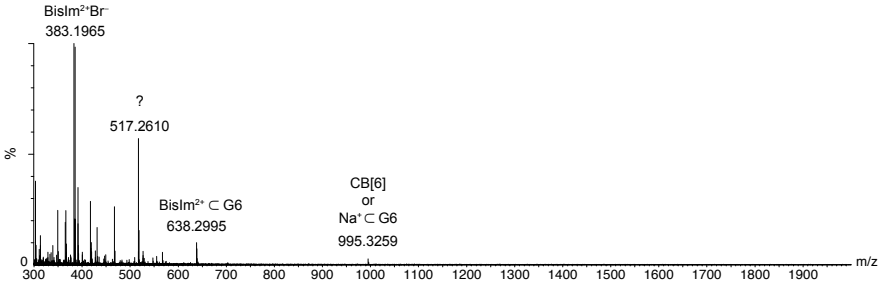

Figure 4.2: *Representative MS (ESI+) of reaction residue from attempted cyclisation of BisIm ⊂ G6 with 2,5-dimethoxy-2,5-dihydrofuran. Peaks are labelled with possible assignments, one major peak remains unassigned. Calculated masses are* $BisIm^{2+}Br^-$ *- 383.1805,* $BisIm^{2+}$ *⊂ G6 - 638.2780,* $CB[6]^+$ *- 995.2866,* Na^+ *⊂ G6 - 995.2837. An occasional, small peak at 1109.3547 was observed which might correspond to* $C_{40}H_{46}N_{24}O_{14}$*+*Na^+*, an adduct of* **G6** *and one 2,5-dimethoxytetrahydrofuran - calc. 1109.3518.*

A second approach to the production of mono-functionalised cucurbiturils was undertaken in conjunction with the Scherman group at the University of Cambridge. This employed the oxidation method developed by Zhao *et al.*, but applied to a larger CB[7] cucurbituril.[193] The CB[7] was first purified from a general cucurbituril synthesis mixture (containing mostly CB[5] and CB[7]),[213] then partially oxidised with ammonium persulfate (1 eq.) in the presence of the **BisIm** guest. The oxidation products were then separated on a resin column using CHP20P MCI GEL resin. The fractions were analysed by ESI-MS and the appropriate portions combined to give **BisIm ⊂ CB[7]monOH**. Any **BisIm ⊂** CB[7] starting material collected was recycled for further oxidations. In order to remove the guest, the product was refluxed with NH_4PF_6 in DCM.

Once collected, the **CB[7]monOH** was then reacted with NaH and propargyl bromide to give monopropargyl **fCB[7]**. These steps were very low yielding, and only a few milligrams of product was finally obtained, from which little convincing characterisation data could be collected.

4.2.5 *Dopamine*

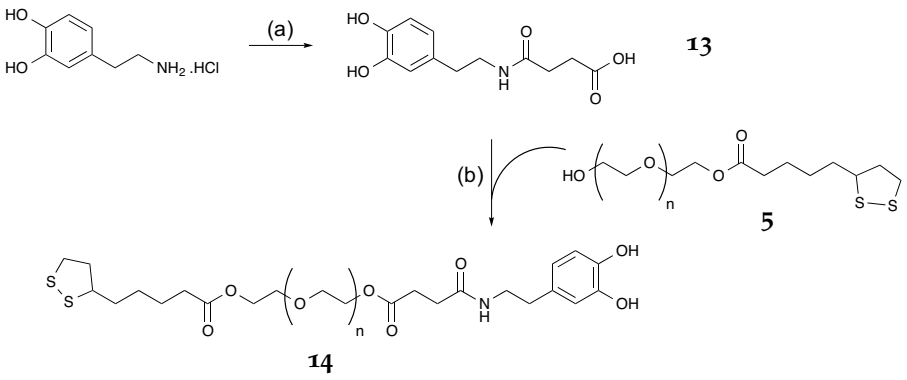

Scheme 4.7: *Synthesis of dopamine derivative* **13** *and attachment to the PEG linker. (a) succinic anhydride, py, RT, 63% (b) DCC, MeCN, RT, unknown yield.*

In order to generate a dopamine based, electron rich π-receptor, similar to the work of Freeman *et al.*,[133] a reaction between dopamine hydrochloride and propargyl bromide was attempted. However the use of K_2CO_3 as a base lead to the decomposition and polymerisation of the starting material. Due to this result, and the difficulty in controlled synthesis of secondary amines to tertiary and quaternary, it was decided to attempt alternates to monopropargyl dopamine. As various other nucleophilic PEG linkers were available, in particular **5**, a dopamine with carboxylic acid functionality seemed like a likely alternative target, shown in Scheme 4.7.

To effect this, dopamine was reacted with succinic anhydride in pyridine, to give the dopamine conjugate **13**. Due to the limited solubility of this material, further coupling with **5** was attempted in MeCN, in the presence of N,N′-dicyclohexylcarbodiimide (DCC). Although limited ^{1}H integral and DOSY NMR evidence suggests that coupling was achieved, HMBC was inconclusive (Fig. 4.3), and the product **14** proved to be more air sensitive than the precursors, decomposing during removal of the N,N′-dicyclohexylurea byproduct on a celite plug.

Due to the air and pH sensitivity of the catechol moiety, it was decided it would not be a useful component in the array.

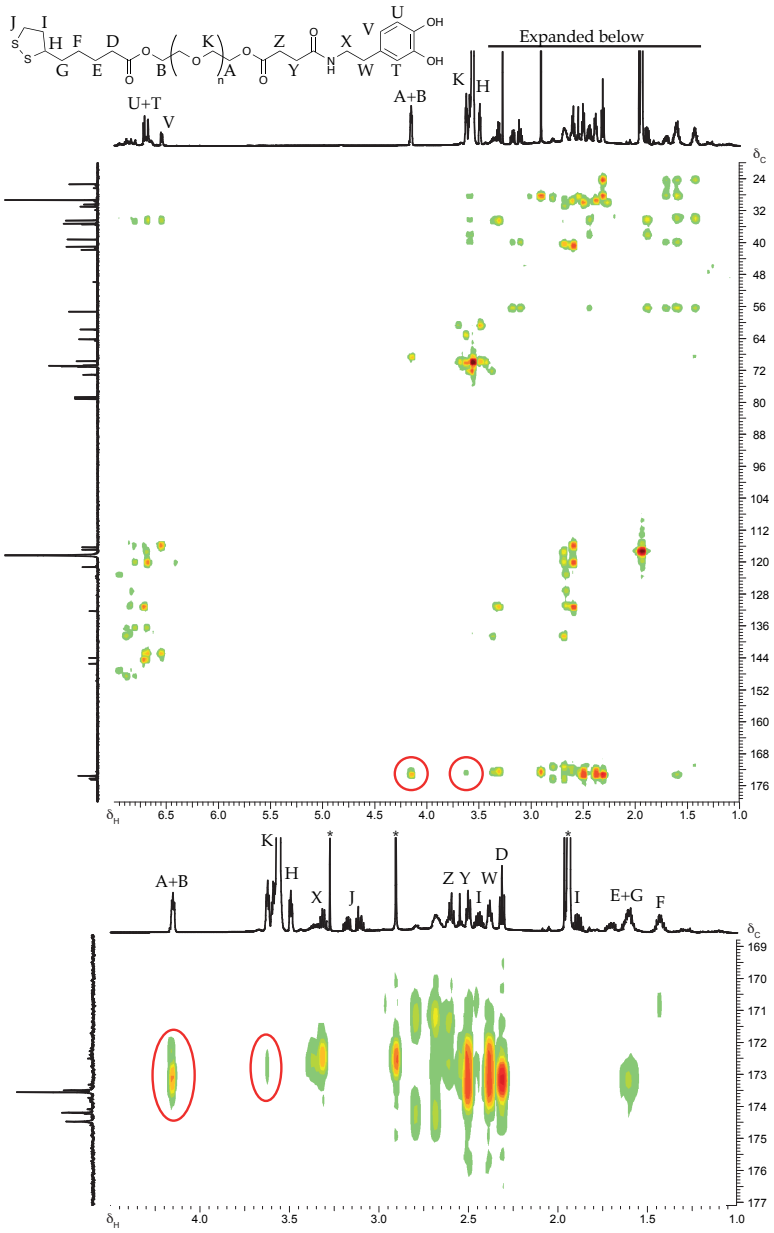

Figure 4.3: *HMBC NMR of* **14** *in d3-MeCN. Axes units are ppm, and *s mark major solvent and impurity peaks. The peak assigned A+B only integrates to 2.7 protons, rather than the expected 4, and only a small amount of interaction between protons A and K and the carbonyl carbon of the ester coupling is present (ringed in red) suggesting an incomplete reaction.*

4.2.6 *Naphthalene*

A naphthalene moiety was synthesised, to create a flat π stacking surface receptor as an alternative to the failed catechol above (Scheme 4.8). A propargyl derivative was easily synthesised by the nucleophilic substitution of 2-naphthol with propargyl bromide to create **15** (Section 8.3). This was then ready to be applied to the click-chemistry coupling scheme described below (Scheme 4.9).

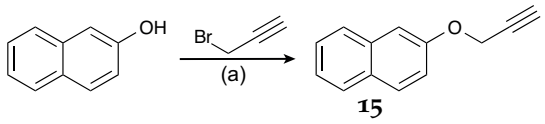

15

Scheme 4.8: *Synthesis of propargyl naphthalene (**15**) from 2-naphthol and propargyl bromide. (a) K_2CO_3, acetone, reflux, 60%.*

4.2.7 *QD Synthesis*

QDs were synthesised by decomposition of CdO and trioctylphosphine-Se at high temperature with varying reaction times, then shelled with ZnS *via* decomposition of Zn-dithiocarbamate onto the surface.[50, 214, 215]

A hot-injection method, followed by growth between 30 s and 10 min at various temperatures allowed for control of the colour (Fig. 4.4), and rapid quenching in boiling water was used to halt the reaction. The full methodology is given in Section 8.5.1.

Figure 4.4: *Several QD samples illuminated with 365 nm light. Samples are (L to R) CdSe@ZnS produced with growth times of 20 s, 30 s, 5 min (low temp.), 10 min (low temp.), InP@ZnS - 20 min, and CdSe@ZnS - 10 min (hi temp.).*

In addition to the above, InP@ZnS QDs were synthesised with a similar method, using indium (III) chloride and tris(trimethylsilyl)phosphine to form the InP cores with a hot injection method. Shelling with ZnS was identical to the method used on the CdSe cores. These particles were synthesised and characterised in collaboration with Dr Joseph Bear.

4.2.8 *QD Assembly*

Green-blue (em. 516 nm), green (em. 544 nm) and red (em. 608 nm) CdSe@ZnS QDs were selected to give maximum spectral variance for multiplexing, and InP@ZnS QDs (em. 560 nm) were selected as a comparison.

To create the final LA based nanoparticle capping ligands, a Huisgen cycloaddition was performed using copper immobilised on carbon, in the presence of base, to form a triazole from azido and alkyne starting materials (Scheme 4.9).[216] This strategy allows for future variation in the library of surface functionalities, potentially enabling attachment of any alkyne functionalised moiety. In this instance the monopropargyl β-cyclodextrin (**12**) and calix[4]arene (**9**) were trialled.

This coupling scheme allowed for easy removal of the copper catalyst afterwards, and dioxane proved a good solvent for all the materials concerned. LA-PEG-CX (**17**) could also be prepared in this way.

An identical scheme was applied to the synthesis of a naphthalene analogue using **15** - to give LA-TEG-naphthalene as compound **16**, however its solubility proved to be very low, so the longer PEG chain analogue, **18**, was produced which gave the desired solubility in methanol.

For the click attachment of monopropargyl cucurbituril (**fCB[7]**) to the TEG linker, aqueous conditions were required for solubility, so the traditional copper (I) chloride with ascorbic acid conditions were applied. However due to the small amount of starting materials (of questionable purity) and low reactivity, no reaction could be detected.

The QD ligand exchange was achieved with 365 nm UV-light acting on the lipoic acid (LA) moiety in a biphasic hexane/MeOH system (Section 8.5.1).[207, 217, 218] The hexane solution of QDs was stirred under an N_2 atmosphere

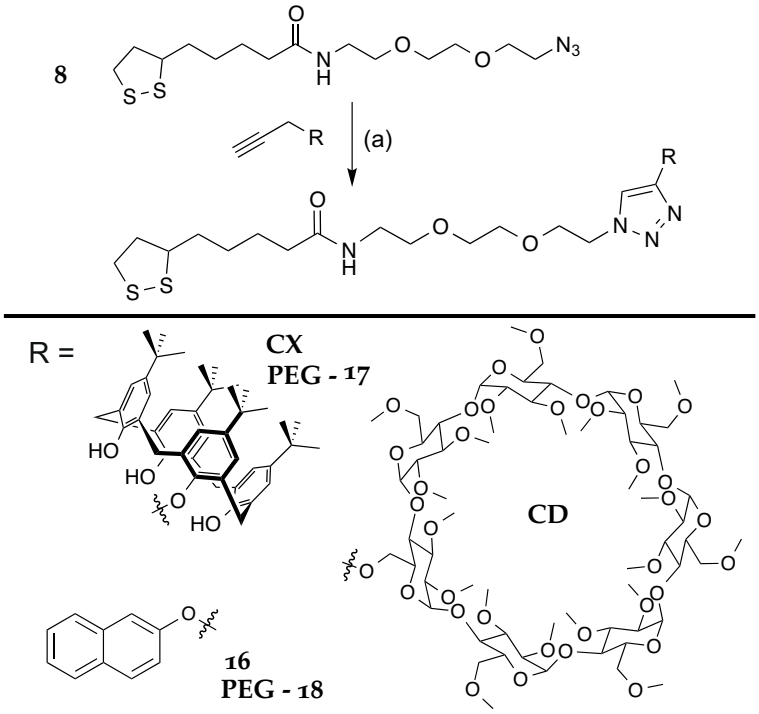

Scheme 4.9: *Scheme of click coupling with* **8** *and monopropargyl derivatives* **9**, **12** *or* **15** *in (a) TEA, dioxane, Cu on Carbon, 72 hrs, 60 °C. Linker* **8** *could be substituted for it's longer PEG analogue* **3** *to give long chain analogues with terminal calix[4]arene -* **17** *and terminal naphthalene -* **18**.

with a methanolic solution of the desired LA terminated ligand(s). A phase transfer catalyst (tetramethylammonium hydroxide) was introduced and the reaction irradiated for 2-3 hours. A visible transfer of fluorescence from the hexane to the methanol layer could be observed. The QDs were then washed *via* precipitation and centrifugation, to remove excess ligands.

This QD functionalisation does not require protected thiols or borohydride salts and gives good control over ratios of different receptors on the surface of the nanoparticle. This proved useful for tailoring solubility of the particles. **CX** capped QDs produced with this method were not fully soluble in MeOH so a 2:3 mix of **CX** to **OMe** was used to give full solubility. The same problem occurred with **18**, but unfortunately even a 1:1 mix of the naphthalene derivative with **OMe** did not give particles that could be re-dispersed after centrifugal washing.

Stable QD suspensions capped with a terminal NH_2 could not be obtained, possibly due to cross linking of the QDs by the terminal amine, or due to triphenylphosphine oxide impurities in the ligand solution (**4**) that could not be removed.

All other particles synthesised, QDs bearing **OH**, **OMe** and **CD**, were composed fully of the named ligand, and were easily redispersed after synthesis and washing steps. It is stated in the literature that particles bear approximately 200 or fewer surface ligands.[219]

Initially each surface ligand (**CD**, **CX**, **OH** and **OMe**) was assembled onto green QDs (em. 544 nm) to create $\mathbf{CD}_{544}$, $\mathbf{CX}_{544}$, $\mathbf{OH}_{544}$ and $\mathbf{OMe}_{544}$. A green PEG analogue was created from **17**, identical to $\mathbf{CX}_{544}$, denoted $\mathbf{CX}^{\mathrm{PEG}}_{544}$. In addition red QDs (em. 608 nm) $\mathbf{CX}_{608}$, $\mathbf{OMe}_{608}$, blue QD (em. 516 nm) $\mathbf{OH}_{516}$, and $\mathbf{OMe}_{\mathrm{InP}}$ were successfully produced and tested. The QDs produced had reduced fluorescence (see below), but were air stable and could be stored in the refrigerator without significant loss (< 10%) of fluorescence for 3 months.

QD samples are named with the surface ligand and the subscript denotes the emission wavelength of the QD core, or material in the case of InP. A superscript is used to denote any additional information e.g. PEG rather than TEG linkers

4.3 PHOTOPHYSICAL CHARACTERISATION AND TESTING

4.3.1 *Spectroscopic properties*

The QDs produced were characterised by UVVis and fluorescence spectroscopy (excitation and emission spectroscopy), as well as TEM and energy-dispersive X-ray spectroscopy (EDX).

TEM showed the core sizes to be approximately 2.5±0.5 nm (n = 70), 3.8±1.1 nm (n = 924) and 9.9±2.4 nm (n=214), respectively for the green-blue, green and red quantum dots. In particular the red cores had a more rod-like aspect with an aspect ratio = 1.6±0.5, arising from a length of 9.9±2.4 and width of 6.5±1.7 nm (See Fig. 8.1 for histograms). EDX on each sample confirmed the presence of Cd, Se, Zn and S (Fig. 4.5a-d). Not shown are the InP@ZnS QDs, which were found to have an average diameter of 3.2 nm by TEM.[50]

The QDs displayed typical absorption and emission behaviour (Fig. 4.5e) with emission slightly stokes-shifted from the first absorption maxima (the band edge). There was a noticeable red-shifting of the band edge on shelling of the QD CdSe core with ZnS, as expected.

On ligation with the LA based surfactants, small changes to the position of the emission maxima were observed, as well as shifts to the absorption

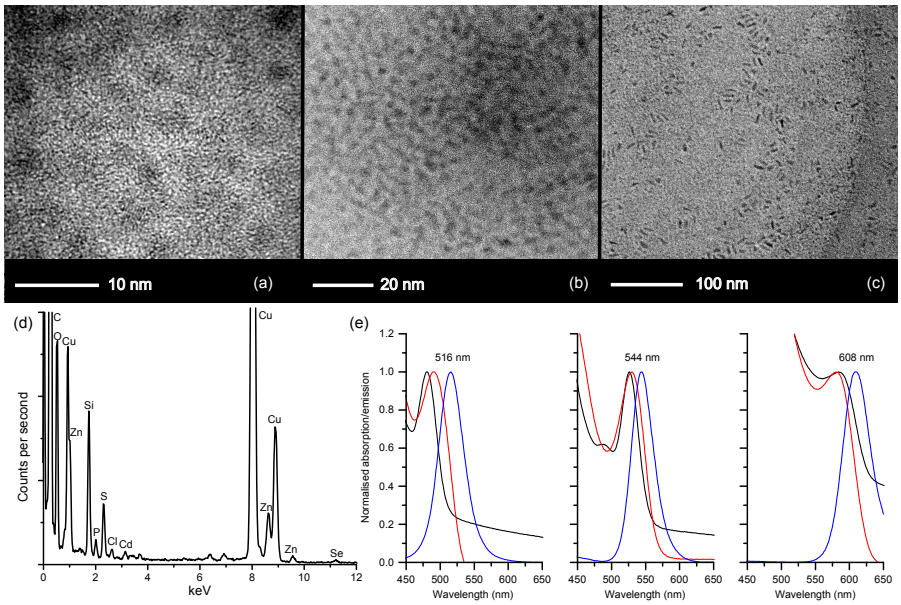

Figure 4.5: *TEM of the 3 QDs (a) em. = 516 nm, (b) em. = 544 nm and (c) em. = 608 nm, showing increasing size and change in aspect ratio. (d) Sample EDS spectrum of 608 nm sample Cu, Si and C from TEM grid. (e) Normalised absorption spectrum for each QD before shelling (black), after shelling (red) and their emission spectrum after ligation (blue).*

spectra. This occurs due to the thiol binding affecting the band gap position slightly, and these changes were typically no more than 10 nm in either direction.

It is reported that this procedure produces a small (0 - 3 nm) red-shift in the emission,[207, 218] however for some samples, a blue-shift was observed (Fig. 4.6). This might be explained as follows: it was noted that ageing of more than a year of the samples before use lead to some noticeable red-shifting (in the order 10 - 15 nm), likely due to some small amount of particle ripening or clustering. This ripening might either be remedied by size focussing and particle separation on photoligation or by removal of larger, less-soluble expanded or clustered QDs during the centrifugal washing stages, causing a blue-shift back towards the original emission value.

The InP@ZnS quantum dots were tested as an alternative to the CdSe. They have several advantages, including comparable or better quantum yield, a reportedly more controllable synthesis, and lower innate toxicity. However it was found that their emission full width at half maximum (FWHM) was very large in comparison to the CdSe materials; 107 nm in comparison to a typical CdSe value of 40 nm. This reduced their utility for

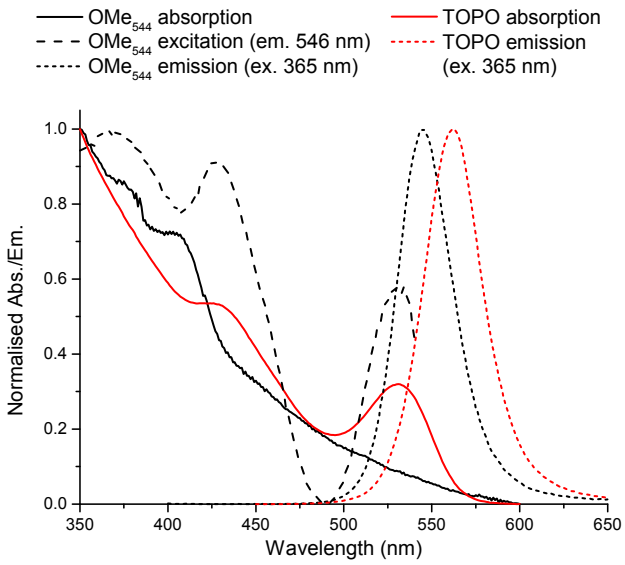

Figure 4.6: *Absorption, emission and excitation spectra for* ***OMe***$_{544}$ *and the original TOPO capped QDs. Excitation spectrum measured at 546 nm and emission spectra excited at 365 nm. All data normalised to improve comparison.*

multiplexing applications, as they would overlap strongly with other colour peaks.

4.3.2 *Fluorescence lifetimes*

Lifetimes of the QDs were measured before and after functionalisation with LA based ligands. Before functionalisation, the lifetimes could be fitted either with a multiple exponential (Eqn. 4.2, $n = 1 - 3$) or with a single stretched exponential (Eqn. 4.3). In these equations, α is a pre-exponential term, t is the time and τ is the lifetime.

$$I(t) = \sum_{i=1}^{n} \alpha_i \exp(-t/\tau_i) \tag{4.2}$$

$$I(t) = I_0 \exp(-t/\tau_i)^{\beta} \tag{4.3}$$

$$f_i = \frac{\alpha_i \tau_i}{\sum_j \alpha_j \tau_j} \tag{4.4}$$

The former implies several modes of radiative decay of the excited state. This model with $n = 2$ is often applied to quantum dots, implying one very fast decay, and another longer, and is typically explained by the presence of trap states within the exciton recombination pathway, leading to a fast,

but poorly emissive alternative.[220] The fractional intensity of each fluorescence decay in the exponential term f can be calculated by Eqn. 4.4.

The stretched exponential (Eqn. 4.3) is a more complex function, assuming only a single fluorescence pathway, but with a dispersion factor accounting for solvent interactions and variability in the nanoparticles. This is represented by β valued between 0 and 1, with $\beta = 1$ equivalent to a normal exponential decay. Typically β is accounted for by inhomogeneities in a sample of QDs, for example slight variations in size, shell thickness or oxidation that might introduce band-gap trap states. The closer β is to one, the less inhomogeneity there is in the QD emission. Stretched exponentials are an attractive alternative fitting method to multiple exponentials, but are not without their issues.[221] It is noted by van Driel *et al.* that it is hard to physically interpret the lifetimes suggested by Eqn. 4.3 and they often differ greatly from values calculated with other methods that may be equally as applicable.

Reduced χ^2 (χ^2_R) indicates the goodness of fit of the function for each decay curve, reduced by the number of channels (here 4096). The closer to 1.0, the better the fit, however this can also be indicative of overfitting, so care must be taken to match the model with explainable physical phenomena.

Lifetimes of trioctylphosphine oxide (TOPO) capped QDs in hexane were measured by time-correlated single photon counting (TCSPC) at their fluorescence intensity maxima and the results fitted with a double exponential or a stretched exponential. The double exponential decay data are given in Table 4.2 and the stretched exponential decays are plotted in Fig. 4.7 and data presented in Table 4.3.

Table 4.2: *Double exponential fit (Eqn. 4.2, $n = 2$) of TOPO capped QDs in hexane, giving the pre-exponential term (α), fractional intensity (f) and lifetime (τ) for each term (i), and the reduced χ^2 for the overall fit*

QD(i)	α_i	f_i	τ_i (ns)	χ^2_R
516 nm (1)	3461.48	7.68	2.74	1.47
(2)	5811.82	92.32	19.58	
544 nm (1)	3325.98	7.16	2.97	1.45
(2)	6111.81	92.84	20.93	
608 nm (1)	4151.30	13.43	4.33	1.45
(2)	5383.50	86.57	21.51	

The fitting of double exponentials (Table 4.2) gave short lifetimes for each QD (< 5 ns) and a longer lifetime (~ 20 ns), which also have a much larger fractional intensity ($> 90\%$). There was not much change between the different sizes of QD. A slight increase in the main lifetime was observed, but this is smaller than experimental error, and indeed much of the literature suggests that lifetime should decrease with increasing particle size (due to a decrease in quantum efficiency).[220]

A slightly worse fit was obtained with Eqn. 4.3, as shown in Table 4.3, and the average lifetime is calculated to be much shorter than with the double exponential fit, as described by van Driel *et al.*[221] However the values obtained do match well to previously obtained literature values for similar systems, and the value for β was consistent between samples.[50] As before there was little variation in lifetime between different QD sizes, with the red QDs showing a slight decrease in lifetime. The advantage to the calculation of an average lifetime with a stretched exponential is ease of comparison to modified samples.

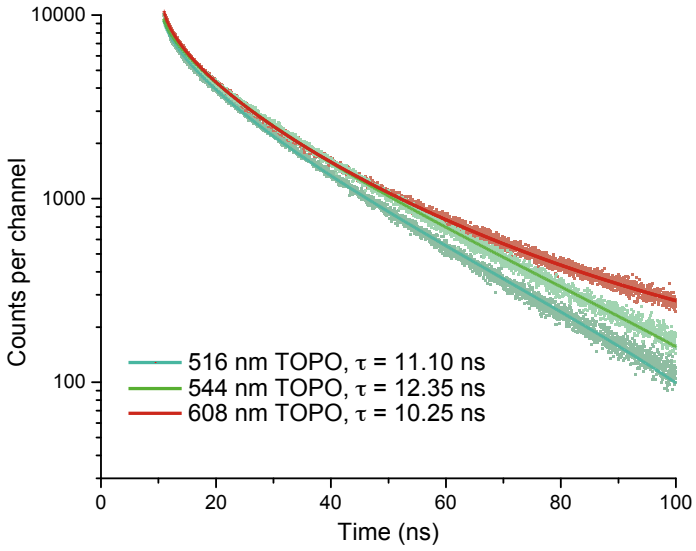

Figure 4.7: *Fluorescence decay data for 3 TOPO capped QDs in hexane of different emission maxima. Decays are fitted with a stretched exponential (Eqn. 4.3) and full data are given in Table 4.3.*

Functionalised 544 nm QDs in methanol (MeOH) were also analysed with TCSPC, after addition of LA-PEG-OMe (**OMe**$_{544}$), LA-TEG-OH (**OH**$_{544}$) and the 2:3 mixture of LA-TEG-CX and LA-PEG-OMe (**CX**$_{544}$). These were compared to the raw TOPO capped 544 nm QDs in hexane. The data from these

Table 4.3: *Stretched exponential fit (Eqn. 4.3) of TOPO capped QDs in hexane, giving the pre-exponential term (α), lifetime (τ), β value, and the reduced χ^2 for the overall fit*

QD	α	τ (ns)	β	χ^2_R
516 nm	9529.61	11.10	0.68	1.65
544 nm	9778.79	12.35	0.68	1.50
608 nm	10608.64	10.25	0.65	1.08

QDs could also be fitted with a single stretched exponential (Eqn. 4.3) as before, and the results are given in Table 4.4. It is clear that there is a marked reduction in average lifetime on conjugation of the thiol terminal ligands to the surface, in addition to a reduction in β, indicating an increase in inhomogeneity between particles. This is explained by S-Zn bonds on the surface creating fluorescent trap states, as well as a change in solvent polarity.[207] Although these QDs are not in aqueous solution, there may be parallels to the work of Hollingsworth *et al.* who state that thiolate species may be responsible for the formation of hole trap states, decreasing fluorescence.[222] The difference between $\mathbf{OMe}_{544}$ and the other samples may be due to a different surface packing density, although this would be unexpected, and the true reason for this disparity remains unclear.

Table 4.4: *Stretched exponential fit (Eqn. 4.3) of TOPO capped 544 nm QDs in hexane and functionalised QDs in MeOH, giving the pre-exponential term (α), lifetime (τ), β value, and the reduced χ^2 for the fit*

QD	α	τ (ns)	β	χ^2_R
TOPO	9778.79	12.35	0.68	1.50
$\mathbf{OMe}_{544}$	10365.50	6.41	0.58	1.23
$\mathbf{OH}_{544}$	10687.46	3.60	0.50	1.33
$\mathbf{CX}_{544}$	10667.31	3.70	0.49	1.26

The decays of these particles could be better fitted with a triple exponential decay (Eqn. 4.2 $n = 3$) - Table 4.5. The issue of the triple exponential decay is one of over fitting - it is hard to conjecture a physical phenomenon that creates the three fluorescence decay pathways suggested. However, although the TOPO capped QDs can be fitted with 2 exponentials, no good fit could be obtained for the thiolated nanoparticles with this model. If assumed to be accurate, one explanation for the ultra fast decay suggested in the triple exponential model ($\sim$ 1 ns) is that it is compensating for a sys-

Table 4.5: *Triple exponential fit (Eqn. 4.2 $n = 3$) of functionalised 544 nm and original TOPO capped QDs in methanol and hexane respectively. The pre-exponential term (α), fractional intensity (f) and lifetime (τ) values are given for each term (i), and the reduced χ^2 for the overall fit*

QD(i)	α_i	f_i	τ_i (ns)	χ^2_R
TOPO (1)	2448.30	2.23	1.30	1.05
(2)	2567.12	14.43	8.01	
(3)	5005.76	83.34	23.73	
OMe$_{544}$ (1)	3172.63	4.14	1.26	1.09
(2)	3514.46	25.44	6.96	
(3)	3110.59	70.42	21.79	
OH$_{544}$ (1)	4016.34	5.16	0.90	1.07
(2)	3185.57	25.59	5.63	
(3)	2405.07	69.25	20.17	
CX$_{544}$ (1)	3903.17	5.12	0.96	1.11
(2)	3224.24	26.62	6.02	
(3)	2303.65	68.26	21.60	

tematic error in the instrument response and fitting parameters. However, the fractional intensity, f, of this ultrashort population does increase after ligand binding, suggesting it is potentially affected by alterations to the fluorophore. There is also a clear move of fluorophore populations from the long decay (*ca.* 20 ns) to the shorter $\sim$6 ns decay on QD ligation with the dithiol, rather than a shortening of the lifetimes.

Ultimately, the conclusion that can be drawn is that ligation with the dithiol reduces the overall fluorescence lifetime of the QDs, likely due to the increase in trap states reducing radiative emission, and this is also borne out by the measurements of the particle quantum yields.

4.3.3 *Quantum yields*

Fluorescence quantum yield (QY or Φ_f) measurements were made on the same subset of QDs, as used above for lifetime measurements. The measurements of Φ_f were made in an integrating sphere attached to a fluorescence spectrometer (see Section 8.1.2 for details). Either a sample or blank of pure solvent was placed in the sphere and excited with monochromatic 365 nm light. The slit widths were set to a fixed value to give optimum fluorescence

intensity, and a neutral density filter was placed in the emission port to prevent damage to the detector when measuring the excitation profile (more details in Section 8.1.2).

The integration over the excitation profile of the empty sphere (containing a blank) - L_a, and on direct sample illumination - L_c are used in conjunction with the integrated luminescence peak of the blank - E_a, and of direct sample illumination - E_c, to calculate Φ_f as photons out divided by photons in:

$$\Phi_f = \frac{E_c - E_a}{L_a - L_c} \tag{4.5}$$

Integration was performed with an Excel based macro provided by Horiba.

It should be noted that the maximum emission peaks in Table 4.6 are for samples over a year old, and thus display significant red-shifting in comparison to their original emission maxima, as discussed in Section 4.3.1

The calculated quantum yields are given in Table 4.6 and demonstrate a sharp drop in Φ_f on ligand exchange with the dithiol moiety. We observe, on average, a 84% decrease. This is in keeping with the literature result, that quotes a 70% decrease.[207]

Table 4.6: *Quantum yield results, Φ_f, as well as position of the maximal emission and size by TEM, for TOPO capped CdSe@ZnS or InP@ZnS in hexane (various sizes) and ligand exchanged CdSe@ZnS (em. 544 nm) in MeOH*

Sample	Max em. (nm)	Φ_f
CdSe@ZnS	532	0.31
CdSe@ZnS	560	0.37
CdSe@ZnS	623	0.27
InP@ZnS	560	0.36
OMe$_{544}$	544	0.08
OH$_{544}$	545	0.05
CX$_{544}$	544	0.05

4.3.4 *Basic testing with explosives*

The QD-receptor conjugates created were then tested against explosive materials, and fluorescence quenching was measured. Dilute solutions of each QD were prepared in MeOH (15 μL/mL) to achieve a fluorescence of approximately 100,000 -200,000 counts per second. This stock was then titrated with fixed amounts of 1 mM DNT, TNT, tetryl, RDX, or PETN, to create

solutions at 15.2, 29.8, 44.1, 58.0, 71.4 and 84.5 μM. Titrations with fixed volumes of MeOH (15 μL) were checked to ensure that additions did not cause appreciable quenching (less than the error on repeat measurement). The fluorescence of each solution was measured multiple times to attain a stable reading. The intensity of the fluorescence peak (I) was used with the initial sample fluorescence (I_0) to measure the Stern-Volmer quenching ($SV = I_0/I$), and %Q (%Quenching) was calculated as $\%Q = 100 \times (1 - \frac{I}{I_0})$.

Initially a proof of concept experiment with TNT was used to test that quenching occurred. For this the QD with a **CX** surface was used - $\mathbf{CX}_{544}$. This quenching was compared to its PEG equivalent $\mathbf{CX}_{544}^{PEG}$, and its red equivalent $\mathbf{CX}_{608}$.

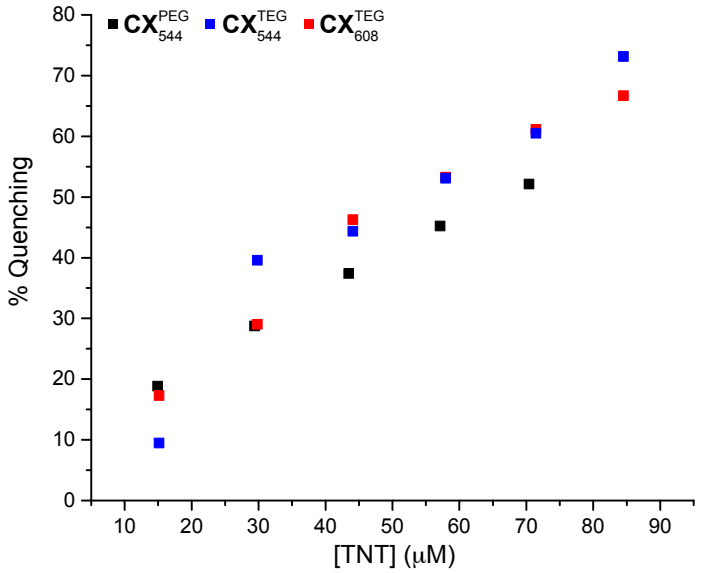

Figure 4.8: *Comparison of %Q for QDs with featuring a calix[4]arene receptor. The linker length is long (black points) or short (blue points) and the colour of the quantum dot is either green (em. = 544 nm - blue points) or red (em. = 608 nm - red points).*

Fig. 4.8 shows no great difference between each of the three systems was observed, other than a slightly lower set of %Q values for the longer PEG linker. This correlates with the idea of greater spacing between receptor and QD reducing quenching efficacy, but on this length scale the difference is apparently small. Changing the colour (and hence size) of the QD appears to cause no change in this instance. In future experiments TEGs were preferred over PEGs because, although the solubility of the TEG coated QDs was slightly lower than that of the PEG coated QDs, the fixed linker length

allowed for easier characterisation (not an average length). They also provided the shorter gap between receptor and QD, as discussed above.

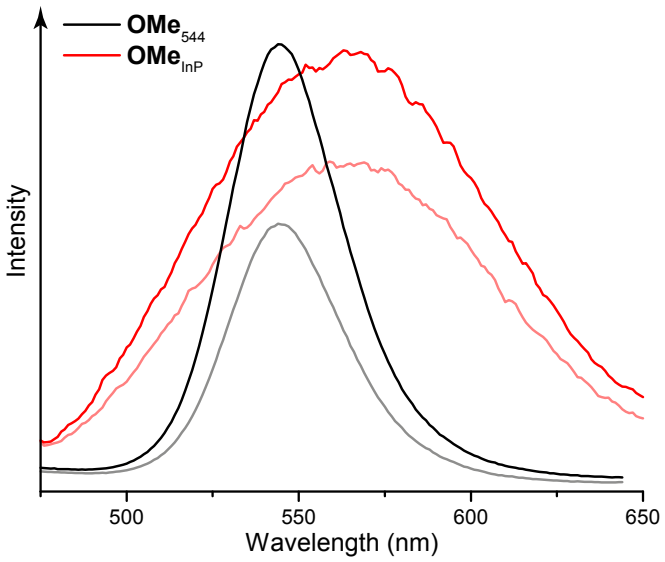

Figure 4.9: *Comparison of quenching of green CdSe QDs (**OMe**$_{544}$, black line) and yellow InP QDs (**OMe**$_{InP}$, red line), both with ZnS shell and* **19** *surface. The faded fluorescence lines are after exposure to ∼ 70 µM of TNT. Spectra normalised to emission maxima for ease of comparison. In each case the spectrometer had an identical set up.*

Fig. 4.9 is a comparison of the quenching of **OMe**$_{544}$ and **OMe**$_{InP}$ with 70 μM TNT, showing a slightly smaller response for the InP@ZnS QDs (25 %Q *vs* 40 %Q). Of particular note here is the broad nature of the InP fluorescence, as discussed in Section 4.3.1, reducing the utility of these QDs in a multiplexed array.

4.4 CONCLUSIONS

This chapter presents the synthesis and characterisation of several novel QD conjugates targeted towards explosive sensing. Although many of the synthetic pathways attempted were either unsuccessful or too low yielding to be of practical use, four key receptor molecules have been synthesised and applied to three different colour CdSe core, ZnS shell QDs. The receptors produced were two cavitands, a calix[4]arene and a β-cyclodextrin, a terminal nucleophile -OH, and a -OMe moiety.

InP cored QDs were tested as an alternative to the more toxic CdSe materials, but deemed to be of low utility in a full array due to their broad fluorescence. The photophysical properties of the QDs produced were characterised, and it was shown that, as expected, replacement of the TOPO capping ligands with thiols lowered the quantum yield, shortening the fluorescence lifetime.

The next step was to apply the QDs in a sensing array, and this is presented in Chapter 5.

5

EXPLOSIVES SENSING

5.1 RATIONALE

It was shown in Chapter 4 that a range of different coloured quantum dots (QDs) could be synthesised with varied surface receptor functionality. The next step was to combine these elements into an array for explosive detection, creating either a single channel or multichannel array. This is the first example of a QD array for explosives detection. The data created from this array was analysed with machine learning tools to differentiate the explosives detected.

The array was tested against five explosives. These explosives were selected on the basis of current threats, and to test a range of different analyte functionalities (structures given in Fig. 5.1). On mixing, the ligand should bind the explosive, and a PET mechanism between the QD and the electron-deficient explosive causes QD fluorescence quenching. This is illustrated by the relative HOMO-LUMO gaps for the explosives and QD band gaps (Fig. 5.2), predicting PET from the excited QD to the LUMO of the explosive. This should occur most favourably for tetryl and least favourably for RDX.

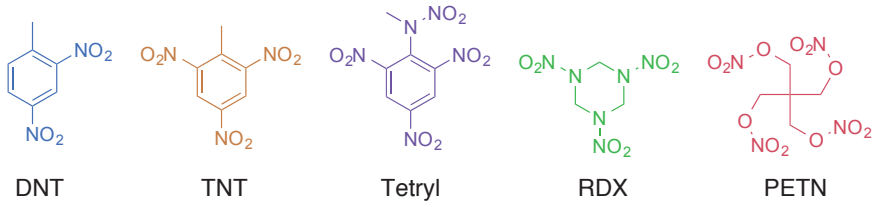

Figure 5.1: *The explosives used in this array study. The colour references are maintained throughout this chapter.*

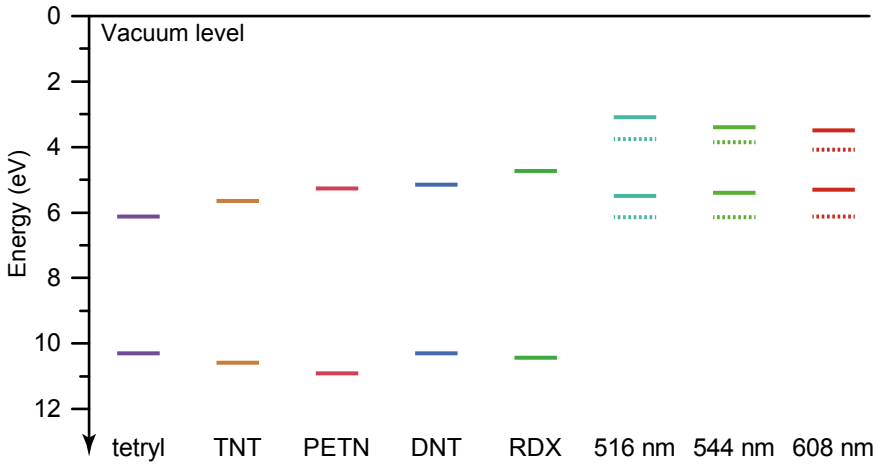

Figure 5.2: *Plot of approximate QD valance bands and conduction bands for 516, 544 and 608 nm QDs and of the HOMOs/LUMOs of explosives used in this study. Explosive HOMO/LUMO energies calculated by density functional theory (DFT) at the B3LYP/6-31G* level from Sanchez* et al.*[223] These have been subsequently modified with a 2.2 eV correction, as suggested by Scanlon* et al.*,[38] to tally the calculated values with measurments from Qasim* et al.*[224] QD band energies are estimated based on two different methods based on measured particle size (solid lines) and XPS literature values,[225] and optical band gap with electochemical literature values (dotted lines).[226]*

5.1.1 *Non-specific or cross-reactive array based sensing*

Array based detection provides a powerful tool for detecting and quantifying a range of analytes in a single test. Samples containing target analytes are introduced to the array, and by measuring the response of individual elements in the array, a picture of the presence (or absence) of each analyte can be built up. Inspiration for this type of system is taken from the biological nose and tongue, and many arrays are indeed referred to as 'chemical noses'.[19]

A hypothetical 'specific' array contains n sensor elements to detect n targets with 100% specificity. This is achievable if the targets are well known and receptors can be created to match them exactly. An example of such an array is ELISA (Enzyme-Linked ImmunoSorbent Assay), which has been used previously to determine and quantify explosives.[68] ELISA is sensitive and widely used; however it is complex, time consuming and expensive. Above all, it requires a detailed prior knowledge of the target analytes to build the antibody assay and in many cases the targets are poorly understood or even unknown. Furthermore, quantitatively detecting small

changes in analyte levels in complex mixtures is challenging with these specific arrays.

To circumvent the problems inherent in a specific array, much recent work has focussed on the development of 'non-specific' or 'non-targeted' arrays.[227] In this case, the array comprises of a range of receptors that are selective rather than specific to target analytes. Each receptor is combined with a reporter. The binding of analyte to receptor, utilising electrostatic, hydrophobic/hydrophilic or hydrogen-bond mediated binding, causes a change in the local reporter, often measured as either colorimetric or fluorescence changes. In particular fluorescence changes are highly desirable as they are easily detectable with sensitive and routine tools. Each analyte tested will interact with each element of the array in a different way, maybe causing an increase or decrease in reporter activity, or maybe no change at all - this is called 'differential binding' (Fig. 5.3).

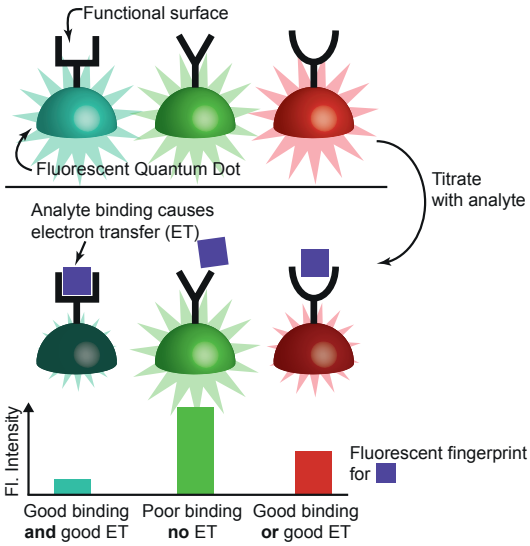

Figure 5.3: *Scheme of a QD sensing mechanism. Differential analyte binding across the multicoloured QD array gives a fluorescent fingerprint for the analyte that can be analysed computationally.*

By recording these responses across the array, a 'fingerprint' for an analyte can be built up - training the array. The array is not limited to detecting single analytes; complex mixtures may also be tested and fingerprinted and these results catalogued in exactly the same way, thus making arrays a powerful tool for detecting small changes within the mixture. This approach can also be applied to detect new materials without the need for the develop-

ment of a whole new sensor element, offering significant advantages over highly specific arrays.

The application of cross-reactive arrays to chemical sensing is a major advance for the detection of explosives. Previous examples have focussed on using electrochemical sensors,[21, 228] colorimetric dyes,[229, 230], or fluorometric dyes,[231–234] coupled with advances in computing power, which allow for application of machine learning techniques to rapidly classify sensing results with a variety of multivariate statistical techniques.[235] The use of nanoparticle-based sensors by Rotello *et al.* for bio-sensing has introduced another powerful tool to array-based chemical sensing, and the new direction of this work focusses on multichannel sensing - combining elements of the cross-reactive array in a single test with multiple measured outputs, for example multiple colour channels. This reduces the sample volume required and increases sample throughput.[22, 236, 237]

As discussed in Section 2.3.5, QDs are well suited to multichannel applications due to their narrow, tailorable emission and broad absorption.[116, 238] Furthermore, exposure of QDs to explosives causes PET-based quenching.[127, 128, 130] If differential binding between different QDs and explosives can be achieved it would give rise to variable fluorescence quenching, allowing a sensing array to be created. Although several simple quantum dot systems have been described for nitroaromatic explosives, such as TNT and picric acid, none have tried to discriminate between multiple types of explosive.[110, 133]

5.1.2 *Statistics in sensing*

The true power of arrays is in their predictive nature. The array creates several pieces of data (such as a fluorescence intensity at each of several wavelengths) associated with one of several classes. The array is trained by modelling this data with a mathematical function, and an unknown sample may then be compared to this function and information gleaned on which class the new data belongs to. These statistical computation techniques for

pattern recognition are termed 'machine-learning'. A widely applied tool for performing this type of computation is linear discriminant analysis (LDA).

LDA seeks to find a linear combination of continuous variables in the data that separates the discrete classes. These linear models can then be compared with new data and the new points classified into a particular 'class' with a confidence interval.[24, 235] This method is widely applied, because of its low computational requirements, good mathematical transparency, and ease of application to multiclass problems, as developed by Rao.[239] A closely related technique to LDA is principal component analysis (PCA). This works in a similar fashion to LDA but does not focus so heavily on the class structure of the data. It has been shown that in certain cases PCA can perform better than LDA, but LDA has been the preferred technique in chemical sensing in recent years.[22, 24, 240]

Another technique that is beginning to be more widely adopted in the field is support vector machine (SVM) classification. It is part of the family of *kernal methods* for data classification. The technique was proposed by Boser *et al.* and separates multidimensional data with a hyperplane that gives the maximum separation between the the hyperplane and the nearest data point of each class it separates - a maximum margin classifier.[241] The generated hyperplane can then be used to classify data of unknown class. The width of the margins on either side of the hyperplane are calculated accounting for two values, a kernel parameter γ and a cost term c that relates to the penalty occurred by a data point too close to the hyperplane.

An SVM is a very powerful and widely applicable technique for classifying many types of data. However it is fundamentally a binary classification algorithm, and so to separate multiclass data, problems must be treated as a series of binary classification problems that are then aggregated, and this adds a degree of complication.[242] Furthermore the algorithms implemented are highly complex, and thus to most researchers this is a 'black-box' technique, making rigorous analysis of the output data difficult. SVMs and LDA are very similar techniques, and it has been shown that in simple cases of an SVM it can be considered equivalent to LDA.[243] However, SVM's more complex approach means it makes fewer assumptions on the data,

and thus can achieve better and more meaningful classification in many cases.

When assessing data classifiers, two approaches may be taken. The first is called 'train-test', whereby a data set is split into two parts, the larger of which is used to train the classifier, and the smaller part used to test the model produced. However for smaller data sets, a preferable option is '*k*-fold cross validation'. Here the data set is split at random as before, but the process is then iterated *k* times, each time using a slightly different training and testing set, to gain an aggregate result of the classifier power.

The statistical techniques detailed here can now be easily implemented by novice researchers in a wide variety of packages such as R, Weka and JMP. Each tool implements the statistical tests discussed here in a slightly different way, with variations in the normalisation and randomisation of data, implementation of *k*-fold cross validation, *etc.*, so it is important to select the package that is capable of performing the required level of analysis but also to compare it to others where possible.

5.2 SOLUTION SENSING PROTOCOL

As described in Section 4.3.4, methanolic solutions of each quantum dot were titrated with one of five explosives of interest; DNT, TNT, tetryl, RDX and PETN, in a single channel fashion - one type of QD per test, and then in a multichannel fashion - three QDs in a single test. The final concentration of explosive in the solution was varied between 15 and 85 μM (approximately 1 - 30 ppm dependant on explosive mass - Table 5.1) with the aim of obtaining a linear quenching regime. Fluorescence of the sample was measured before and after each addition at least three times to ensure a stable reading was obtained. The intensity of the fluorescence peak (I) was used with the initial sample fluorescence (I_0) to measure the Stern-Volmer quenching ($SV = I_0/I$), and %Q (%Quenching) was calculated as $\%Q = 100 \times (1 - \frac{I}{I_0})$.

Limit of detection (LOD) was defined in a basic sense as the mean of a blank measurement plus 2 standard deviations.[244] The standard deviation and mean of the blank were determined from at least triplicate repeat mea-

Table 5.1: *Conversion table of molar, weight/volume and ppm values for each explosive concentration*

Molarity	Explosive - μg/mL (ppm)				
(μM)	DNT	TNT	tetryl	RDX	PETN
15.2	3.4 (4.4)	2.8 (3.5)	4.4 (5.5)	3.4 (4.3)	4.8 (6.1)
29.9	6.8 (8.6)	5.4 (6.9)	8.6 (10.9)	6.6 (8.4)	9.4 (11.9)
44.1	10.0 (12.7)	8.0 (10.2)	12.7 (16.0)	9.8 (12.4)	13.9 (17.7)
58.0	13.2 (16.7)	10.6 (13.4)	16.6 (21.1)	12.9 (16.3)	18.3 (23.2)
71.4	16.2 (20.5)	13.0 (16.5)	20.5 (26.0)	15.9 (20.1)	22.6 (28.6)
84.5	19.2 (24.3)	15.4 (19.5)	24.3 (30.7)	18.8 (23.8)	26.7 (33.8)

surements of I_0. A straight line was then fitted to the linear response portion of the sensor Stern-Volmer response ($\frac{I_0}{I} - 1$) with increasing concentration, using least squares regression. Where linear fit could not be achieved with the fit meeting the origin, no LOD is calculated, as there would be no confidence in the value. Where a LOD value for an analyte over all sensor elements is given, the highest limit is taken.

LDA and SVM analysis were performed on a dataset consisting of measurements of one attribute per QD (e.g. %Q-$\mathbf{CX}_{544}$ or SV-516 nm) and the class. The concentration data was removed to blind the computer model. LOD fitting and LDA analysis was performed in the JMP 11 software package. SVMs were performed using WLSVM in WEKA.[245] For the SVM, a radial basis function (RBF) kernel was applied and an iterative (grid) search was used to optimise the cost c and kernel value γ for each data set, followed by 10-fold cross validation with the optimised values. The grid search was performed using pairs of values $= 2^x$ and x was incremented in 0.5 increments.[21, 246] Other analysis and modelling was performed in OriginPro.

Comparison between statistical models built from the array data are firstly compared by their predictive accuracy. If two models achieve the same accuracy (a maximum of 100%) then the negative log likelihood score, -2log-Likelihood, gives an indication of how well the model is designed. It is defined as the probability of the data given the parameters of the model. The log of the likelihood will always be negative, with values closer to zero indicating a better fitting model, so even if the two models score 100% clas-

sification accuracy this value gives an comparable indicator of goodness between them.

The output from the LDA model is represented as a canonical score plot, showing the data reinterpreted in terms of the classification applied. In this case the LDA calculates linear combinations of features for each instance that explain the most variation between classes. The cannonical plot shows the instances plotted against these linear combinations. Thus the x-axis is the canonical, here the linear combination, that gives the most variation between classes (the percentage is given after the dash), and the y-axis is the canonical that gives the second most variation. Each instance is plotted, and the average of each class is shown, with a 95% confidence interval as a circle around it.

5.3 RESULTS AND DISCUSSION

Fig. 5.4a illustrates the quenching results of each single channel QD for each analyte. Of the green channel QDs, $\mathbf{CX}_{544}$ showed good quenching for TNT and tetryl, and to a lesser extent DNT. For example TNT achieved maximal %Quenching of 73 %Q and had an LOD of < 0.1 μg/mL. Tetryl had a maximal 47 %Q and a LOD = 1.2 μg/mL (Table 5.2). The response of the **CX** surface is justified through π-system interactions between the calixarene and the electron-deficient arene systems of TNT, tetryl and DNT, causing strong binding between analyte and QD, and the relative efficiencies of the PET process between the QD and the analyte. Although PETN was hard to detect, often causing the least quenching of all the analytes, $\mathbf{CD}_{544}$ achieved a greater response to PETN than for DNT. The PETN response from $\mathbf{CD}_{544}$ is small (16% at maximum), implying poor electron transfer between analyte and QD, but the increased response as compared to DNT or RDX gives a good discriminant for this compound. It is possible that the PETN could bind one arm inside the hydrophobic **CD** cavity, due to its greater flexibility compared to the rigid aromatic explosives.[180, 247]

QDs $\mathbf{OH}_{544}$ and $\mathbf{OH}_{516}$ gave a similar response to the five analytes, likewise $\mathbf{CX}_{544}$ and $\mathbf{CX}_{608}$, implying that for the most part, the different colour

Table 5.2: *LOD values in μg/ml for single channel array elements*

Explosive	**CD**$_{544}$	**OMe**$_{544}$	**CX**$_{544}$	**OH**$_{544}$	**OH**$_{516}$	**CX**$_{608}$	**OMe**$_{608}$
DNT	-	0.57	0.51	0.69	-	1.38	0.07
TNT	0.41	0.10	0.01	0.22	0.55	0.11	0.04
Tetryl	0.87	0.74	0.23	0.34	0.61	0.37	0.21
RDX	-	-	0.88	1.22	1.63	1.40	0.55
PETN	-	9.79	0.77	2.39	0.11	2.55	1.23

QDs are interchangeable with the different functional surfaces. However, **OMe**$_{608}$ gave far higher quenching responses than its green counterpart, in particular to TNT and tetryl, achieving maxima of 85 %Q and 77 %Q respectively. This behaviour makes **OMe**$_{608}$ a useful stand-alone sensor for nitroaromatics with a limit of detection of $<$0.21 μg/mL for DNT, TNT and tetryl (Table 5.2), giving rise to the potential for naked-eye detection. This will be realised in Chapter 6.

This deviation from the expected low response could be due to the larger and less spherical (Section 4.3.1) red quantum dots having a lower ligand surface coverage, allowing the more rigid, planar, arene analytes to effectively slip down the gaps between the **OMe** ligands, and interact more closely with the QD surface, thus facilitating a stronger quenching. It has been recently stated that dithiol head-groups, such as dihydrolipoic acid, provide less surface protection than monothiols at low adsorbate concentrations, but are less likely to be displaced, thus ensuring longer term colloidal stability.[248] The larger %Q values are not observed for **CX**$_{608}$ due to the bulky ligand head group, providing more effective surface shielding. To explore this, we modelled how the analytes might interact with the QD surface.

5.3.1 *Surface interaction modelling*

Ab-initio methods (performed by Dr Alberto Roldan), with full details given in Appendix B, were applied to probe whether binding of the analytes to the particle surface was feasible, and to measure the resulting distortion of the electronic structure. Despite the small size of the CdSe@ZnS QD, they are large enough to be modelled as a periodic slab of ZnS. Thus a model

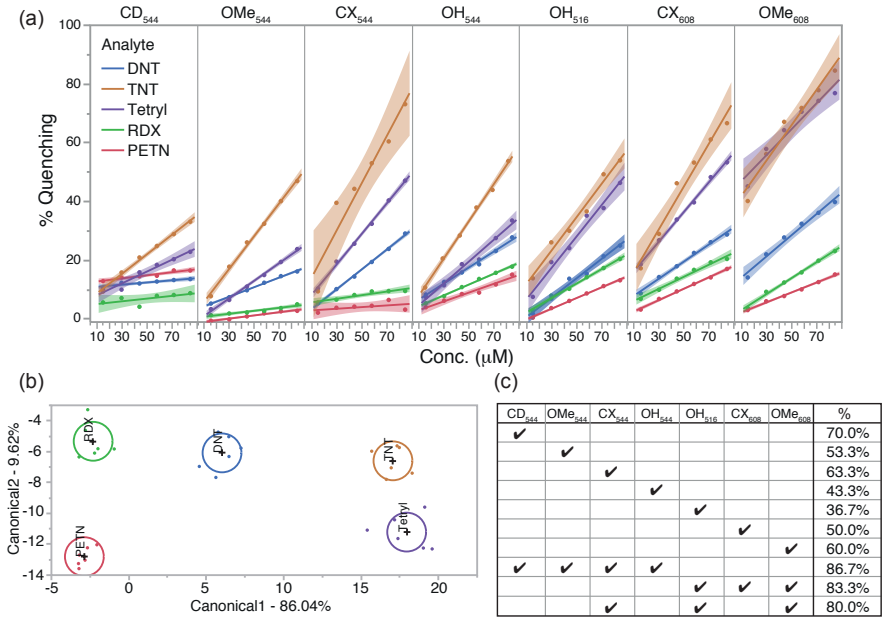

Figure 5.4: *Results of single channel sensing with 7 red, green and blue QDs. (a) % Quenching for each QD for a range of analyte concentrations. Lines indicate best linear fit by least-squares, shading indicates confidence of fit. (b) Canonical plot (LDA) for %Q dataset. Ellipses indicate 95% CI of the mean. Data is classified with 100% accuracy. (c) Jackknifed analysis of same dataset showing correct classification % for several subsets of the array, indicated by ticks, to illucidate the discriminatory power of each QD, indicated by the % of correct classification for each subset.*

of wurzite ZnS (110) was developed with density functional methods.[249] Reduced functional approximations of each of the five analytes were then tested on the surface to measure the extent of the adsorption on the pristine ZnS (110) surface (Fig. 5.5 and Fig. 5.6) as well as charge transfer. The results, summarised in Table 5.3, show that thiols, as expected, form strong surface bonds, and although the analytes can bind to the surface it is unlikely the thiols are displaced. Nitroaromatics showed little interaction through the aromatic ring but did bind to the surface through the nitro-groups. An increase in the number of nitro groups did not significantly increase the binding potential, but did increase the electron withdrawal. Finally nitroaliphatics were modelled and nitrate esters and nitroamines were shown to also bind, however nitroamines bound more favourably.

In the case **OMe**$_{608}$, if each analyte were reaching the surface then we would expect nitroaromatics to affect fluorescence substantially due to reasonable binding and electronic structure modification. However we predict

Table 5.3: *Summary of adsorption parameters : binding energy per site (E_B), charge transfer (Δq), band gap (E_g), and workfunction (ϕ) compared with pristine ZnS(110) surface*

Approximation	E_B/eV	Δq/eV	E_g/eV	ϕ/eV
Single thiol	−0.72	−0.1	2.06	3.5
Dihydrolipoic acid	−0.50	−0.1	2.05	3.5
Benzene	−0.15	0.0	2.06	3.7
Nitrophenol	−0.19	0.0	1.32	4.0
Dinitrophenol	−0.20	0.2	0.63	4.7
Nitrate ester	−0.17	0.8	1.82	3.6
Nitroamine	−0.48	−0.2	2.03	3.4

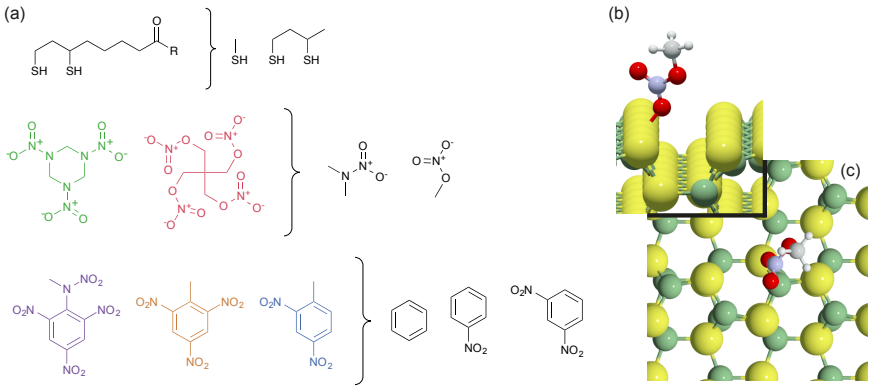

Figure 5.5: *Modelling of surface interactions. (a) First approximations of analytes and surface bound thiol. Example nitrate ester bound to slab in (b) side on and (c) top down profile. Atoms of S are given in yellow, N blue, O red, C grey, H white and Zn green.*

a lower response from nitrate esters due to low binding, despite their good electron withdrawal, and strong binding of nitroamines, but no charge transfer (also supported by the position of RDX in Fig. 5.2). This model is simplified because it does not account for the sterics between molecules and capping ethylene glycol chains or other lateral interactions, or indeed solvents, but allows us to analyse potential trends.

Accounting for the extra NO_2 groups on TNT and tetryl, and the steric bulk of PETN and RDX, the expected series might be tetryl $\simeq$ TNT $>$ DNT $>$ PETN $\simeq$ RDX, which is as-observed. Thus the ordering of the analytes should be similar whether or not they penetrate the ligand surface of the QD. However the greatly enhanced quenching of **OMe**$_{608}$, despite its larger distance between QD surface and distal functionality, and weakly interacting OMe group, suggest that penetration is occurring. The poor quenching of PETN of all the QD systems is interesting, given its strong electron with-

drawing power, as predicted in Fig. 5.2 and Table 5.3. It is likely that weak formation of complexes with either the QD ligands or surfaces is to blame, and so better PETN binding ligands must be sought.

In order to further probe the nature of the QD-explosive interaction, an in-depth study of the changes to the fluorescent lifetimes and electochemical profiles at the binding event will have to be made. This is discussed further in Chapter 7.

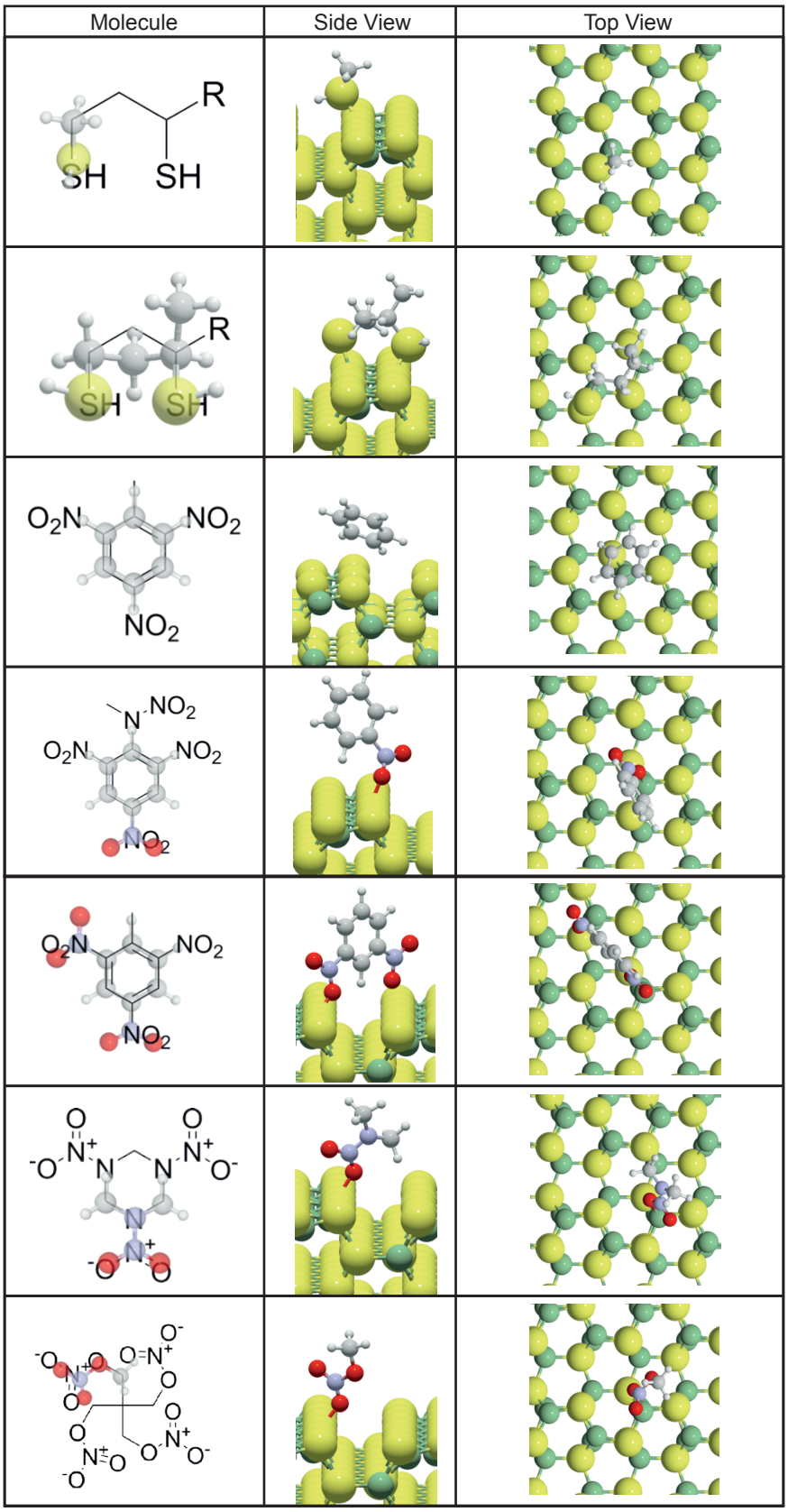

Figure 5.6: *Molecules in position on ZnS surface, with relation to used analytes and ligands.Yellow = S, Green = Zn; Grey = C, White = H, Red = O and Blue = N.*

5.3.2 *Single channel sensing*

The differential quenching of each QD by each analyte was used to build up fingerprints for the analytes in the range of concentrations (as described in Section 5.2). The fluorescence quenching was expressed as either Stern-Volmer quenching (SV) or percentage quenching (%Q). These fingerprints were then analysed with machine learning techniques to investigate the classification accuracy achieved. The models were blind to the concentration data and LDA was employed.

We examined first whether SV or %Q data provided better classification power. LDA analysis of the full dataset attained 100% classification accuracy in each case, but the -2logLikelihood score for the SV data of 0.389, indicated that it performed slightly worse than analysis of %Q data, with -2logLikelihood = 0.001 (see Section 5.2 for a definition of this term). This difference is further illustrated in the canonical plots for each analysis. The %Q plot ellipses (95% confidence limit of the data mean) are all well separated (Fig. 5.4b, page 83) whereas for the SV data (Fig. 5.7) there is close proximity between the TNT and DNT ellipses.

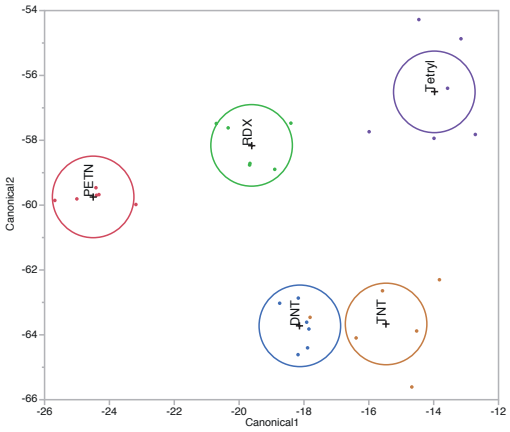

Figure 5.7: *Canonical plot for LDA analysis of the full single channel SV data. Ellipses show 95% CI on the mean.*

As a comparator, an SVM utilising 10-fold cross validation was tested, as discussed in Section 5.2, but returned poorer classification results than the LDA model, with both data sets achieving lower accuracy, and the SV model outperforming the %Q model 96.7% to 93.3% (Table 5.4).

Table 5.4: *Confusion matrices for SVM analysis on the single channel %Q (L) and SV (R) data after 10 fold cross validation. The class of the data points is given on the vertical axis, and their classification by the SVM across the horizontal*

Classification					SVM
DNT	TNT	Tetryl	RDX	PETN	93.3%
6	0	0	0	0	DNT
0	**5**	1	0	0	TNT
0	1	**5**	0	0	Tetryl
0	0	0	**6**	0	RDX
0	0	0	0	**6**	PETN

Classification					SVM
DNT	TNT	Tetryl	RDX	PETN	96.7%
6	0	0	0	0	DNT
0	**5**	0	1	0	TNT
0	0	**6**	0	0	Tetryl
0	0	0	**6**	0	RDX
0	0	0	0	**6**	PETN

To investigate which QDs had the most discriminatory power in the array a jackknifed analysis was conducted, using the %Q dataset, running the LDA multiple times including only a subset of the particles in turn (Fig. 5.4c). As expected, removing quenching information decreased classification accuracy, and indicated that the most powerful discriminating elements were $\mathbf{OMe}_{608}$, due to its large quenching response to aromatics, and $\mathbf{CD}_{544}$ due to its differential response to PETN.

However, using a subset of the seven QDs, good classification accuracy could still be achieved. For example, a single channel array using the four 544 nm QDs could classify the data with 87% accuracy. Thus a *multichannel* (mixed element in a single test) sensor was designed to utilise 3 different coloured QDs, each bearing a different surface functionality. The considerations, beyond variable colour, were selecting the most discriminating elements, and choosing those that gave the largest dynamic response to provide clear peaks in the more complex spectral environment. $\mathbf{OH}_{516}$, $\mathbf{CX}_{544}$ and $\mathbf{OMe}_{608}$ were selected for these reasons, and when modelled as a subset of the single channel data gave a classification accuracy of 80% (Fig. 5.4c, Fig. 5.8a).

5.3.3 *Multichannel sensing*

To create a multichannel sensor for explosives the three QDs ($\mathbf{OH}_{516}$, $\mathbf{CX}_{544}$ and $\mathbf{OMe}_{608}$) were mixed. The final spectrum was confirmed by recombination of individual QD spectra to ensure there were no interaction effects

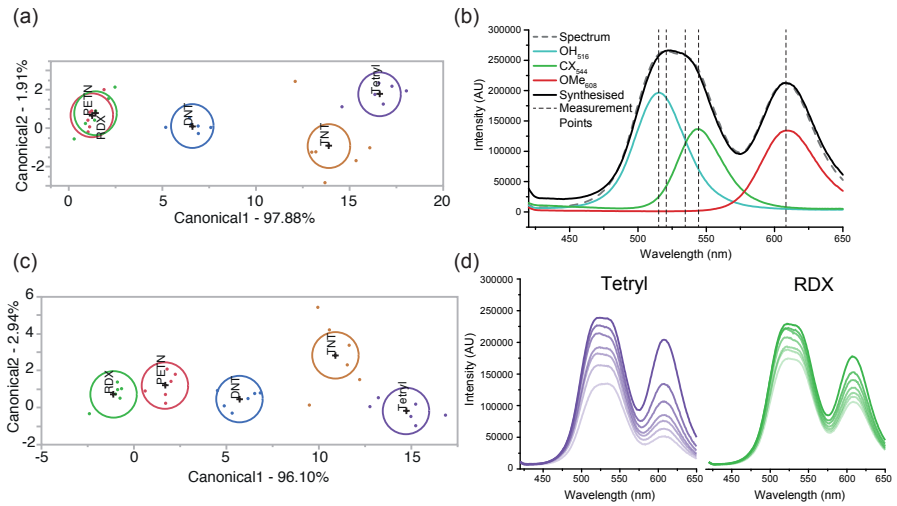

Figure 5.8: *Results of multichannel sensing. (a) Canonical plot for LDA analysis of single channel data approximating the multichannel example with* $\mathbf{OH}_{516}$, $\mathbf{CX}_{544}$ *and* $\mathbf{OMe}_{608}$. *Ellipses show 95% CI on the mean. Classification accuracy is 80%. (b) Calculated fit of the 3 QDs to give composite curve relative to obtained fluorescence spectrum. (c) Canonical plot for multichannel array with %Q data for 516, 520, 533, 544 and 608 nm. Classification accuracy is 100% (d) Sample titration curves for tetryl and RDX against the multichannel system, with increasing concentration decreasing the fluorescence.*

between the individual elements (Fig. 5.8b). On excitation at 365 nm, the analytes were titrated at the same concentrations as before, and the principal QD emission wavelengths were monitored, as well as 2 intermediate wavelengths in the overlap regions between peaks (516, 520, 533, 544 and 608 nm). LOD analysis on the data was hard to perform for RDX and PETN, due to non-linear responses, but for nitroaromatics tetryl and TNT, LODs of less than 1 μg/mL and 0.2 μg/mL were obtained respectively, across the whole array (Table 5.5). These array LODs were higher than they might be, as $\mathbf{OH}_{516}$ did not perform as well as the other two channel QDs, so further improvements would focus on this element.

Table 5.5: *LOD values in µg/ml for multichannel array wavelengths*

Explosive	516 nm	520 nm	533 nm	544 nm	608 nm
DNT	1.84	1.48	0.71	0.12	0.30
TNT	0.10	0.18	0.16	0.20	0.09
Tetryl	0.77	0.71	0.40	0.01	0.11
RDX	-	-	-	2.27	0.51
PETN	-	-	2.88	0.39	0.11

The change in fluorescence at the five points, at different concentrations, was then used to train and test LDA and SVM models with SV and %Q

datasets as before. LDA analysis on the %Q data set performed better than a simple combination of the three individual channels from the single channel dataset (80% accuracy), scoring 100% classification accuracy (-2logLikelihood = 1.51) (Fig. 5.8c). The multichannel setting allows for this improved classification accuracy, by probing the cross-reactivity between the three sensor elements directly in a single test. The SV dataset again performed worse, only scoring 83.3% accuracy (Fig. 5.9).

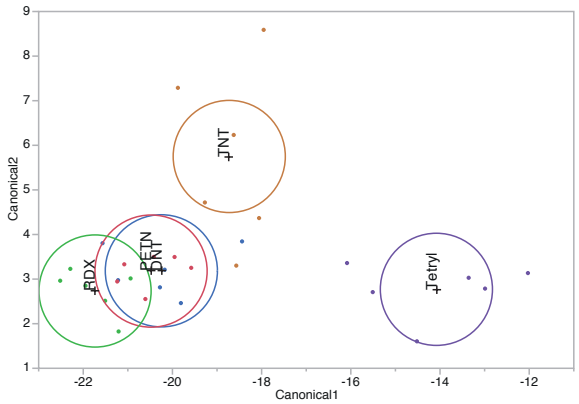

Figure 5.9: *Canonical plot for LDA analysis of full multichannel SV data. Ellipses show 95% CI on the mean*

SVM analysis with the multichannel SV dataset performed better than for LDA, with 90% classification accuracy, and also performed better than SVM analysis of the %Q data (86.7% accuracy), mirroring the results with the single channel dataset (Table 5.6).

Table 5.6: *Confusion matrices for SVM analysis on the multichannel %Q (L) and SV (R) data after 10 fold cross validation.The class of the data points is given on the vertical axis, and their classification by the SVM across the horizontal*

	Classification					SVM
	DNT	TNT	Tetryl	RDX	PETN	86.7%
DNT	**5**	0	0	0	1	DNT
TNT	1	**5**	0	0	0	TNT
Tetryl	0	1	**5**	0	0	Tetryl
RDX	0	0	0	**6**	0	RDX
PETN	0	0	0	1	**5**	PETN

	Classification					SVM
	DNT	TNT	Tetryl	RDX	PETN	90.0%
DNT	**5**	0	0	0	1	DNT
TNT	1	**5**	0	0	0	TNT
Tetryl	1	0	**5**	0	0	Tetryl
RDX	0	0	0	**6**	0	RDX
PETN	0	0	0	0	**6**	PETN

Jackknifed analysis was performed with the most successful (%Q, LDA) model to investigate the classification power of each wavelength (Table 5.7). It was found that no one wavelength particularly contributed to the over-

all predictive power of the array, with most individual QD or intermediate emissions scoring 40% classification accuracy by themselves. Removing the intermediate wavelengths (520 and 533 nm) leaving the 3 principal emission peaks in the dataset did score 100% classification accuracy, but with -2logLikelihood = 7.98, indicating a greater risk of misclassification due to poorer differentiation between the RDX and PETN data. However, the fact that perfect accuracy is achievable with these three wavelengths, in comparison to the 80% achieved by the combination of the three single channel results, highlights the advantages of a multichannel array.

Table 5.7: *Jacknifed analysis on multichannel system with % classification for each model*

516 nm	520 nm	533 nm	544 nm	608 nm	%
✓					40.0
	✓				40.0
		✓			40.0
			✓		40.0
				✓	60.0
			✓	✓	96.7
✓			✓	✓	100
		✓	✓	✓	96.7
✓		✓	✓	✓	96.7
✓	✓	✓	✓	✓	100

5.3.4 *Contaminants*

The multichannel array was dosed with contaminants and then TNT sensing attempted - Fig. 5.10. Each measurement was an injection of 15 μL of material. On addition of MeOH some dilution occurs to the $\mathbf{OMe}_{608}$ channel, and in each case this channel proves to be the least stable. Other channels are not particularly influenced by addition of water, or by nitrobenzene (NB), beyond the dilution effect. In each case the addition of a small amount of TNT causes a larger quenching effect.

The quenching of TNT on the **OMe**$_{608}$ channel is slightly reduced by the excess concentration of NB (abut 3 %Q), possibly due to NB interfering with the binding of TNT to the QD at low concentrations.

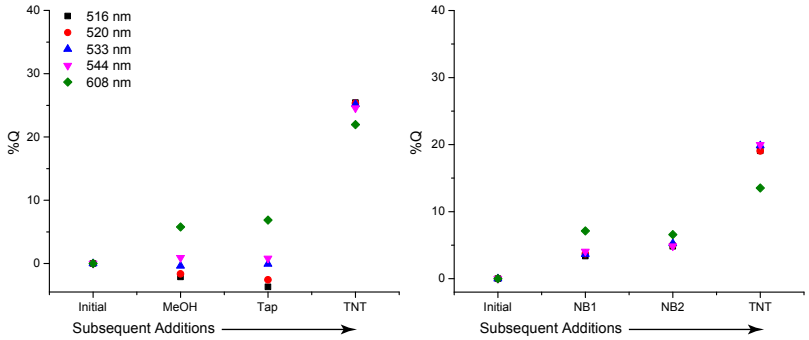

Figure 5.10: *Consecutive additions of different solvents and contaminants to the multichannel system. Each addition is and injection of 15 µL. NB1 and NB2 are subsequent additions of 1mM nitrobenzene. On the right hand plot, the final NB concentration was 30 µM. The final TNT concentration in each case was 14 µM.*

5.4 CONCLUSIONS

The QDs synthesised in Chapter 4 were successfully applied to array based detection of five explosives with machine learning analysis. Multichannel sensing was shown to be advantageous to single channel sensing, using three of the seven QDs to achieve the same classification power. LDA and SVM were used to classify the data, and LDA proved the more successful of the two, with a dataset of %Q (%Quenching) values. However SVM was more successful when applied to a dataset of Stern-Volmer values (SV). Because SVM is generally the more powerful of the two techniques, due to its less stringent data requirements and more powerful class separation technique (Section 5.1.2), these results are surprising. However the classifications achieved are comparable in accuracy, and thus the small differences may even be due to variation in the data handling (e.g. normalisation techniques) by the two different software packages used, or issues in optimising the SVM with the grid search technique, for example only finding a local maxima.

The LODs achieved by both the single channel and multichannel array for TNT were comparable or good enough for detection of Environmental Pro-

tection Agency mandated levels in drinking water (Section 1.1.2), however it would be preferable to work at an order of magnitude lower, to ensure reliability at these sub-ppm concentrations. In particular a focus on improving the sensing of the nitroaliphatics, such as PETN, would be profitable.

6

SENSOR IMMOBILISATION

6.1 RATIONALE

Once a working array is developed it must then be manufactured into a format or platform that can be used by a (potentially non-expert) practitioner, in the field, away from the laboratory. Thus solution based tests become more impractical and other support matrices for the sensing array must be created.

One simple method is simply to dry the array onto a test strip that can then have analyte applied and a result read out, either by eye, or by a device. Pioneers in this latter field are Ozcan *et al.* who have pushed forward mobile phone based diagnostics for disease and pollution, with simple fluorescent tests read off by the phone's camera.[115, 250] A similar device was produced using a novel, protein based, colorimetric test strip for viruses.[251] At a more complex level, a phone-based well-plate reader has been developed for an ELISA assay.[252]

Successful paper arrays for explosive detection have been created by Suslick *et al.* which can be read by a flat-bed scanner, but have not yet transitioned into a portable device.[253–257] However a similar technique has been made portable by Salles *et al.*[258]

Another interesting medium for immobilising a sensing element is imprinted porous Si,[259, 260] which has the benefit of being more durable than paper, and more readily directly functionalised with chemical moieties to control binding.[261]

A relatively unexplored area, that sits between solid (paper/dried) arrays and solutions, is the encapsulation of sensing elements in gels, inparticular organogels. Organogels have been used as a method for encapsulating nanomaterials with good spatial organisation and stability, leading

to the development of optical sensors, catalytic frameworks and new magnetic materials.[262–266]

Many organogel syntheses utilise complex or multi-component gelators, increasing their complexity. However, of particular interest was a new class of single component gels formed from a supramolecularly assembled low molecular weight organogelator (LMWO).[267–269] LMWOs are fascinating materials with a wide range of applications, being light-weight, optically clear, self-healing and and easily mouldable.[270] The LMWO material is dissolved in a suitable solvent at elevated temperature, and on cooling self assembles into a fibrous network, creating the gel. If functional nanomaterials are encapsulated, they can then be handled more simply than if in solution, but may not exhibit some of the problems of dried or solid materials, for example, aggregation-induced fluorescence quenching.

Here, two methods of sensing using non-solution phase QDs were designed and tested. The first uses the very sensitive red **OMe**$_{608}$ QDs on a paper test strip to detect TNT and tetryl in solution. The second is a gel based sensor for vapour phase nitrobenzene; a volatile organic compound (VOC) and explosive simulant. The latter was part of a wider investigation into nanomaterials in gel substrates, leading to the creation of a supramolecular gel - nanoparticle hybrid material with multifunctional properties; a so-called 'smart material'.

6.2 PAPER TEST STRIPS

Strips of Fisherbrand QL110 filter paper (∼1 cm x 5 cm) were cut, and to one end, two 5 μL drops of the as-synthesised **OMe**$_{608}$ was applied, with air drying between applications. This produced a circular sensor element, diameter ∼0.8 cm, which could be visualised under 365 nm light. Four of these strips were then exposed to 8 μL each of water, MeOH, tetryl in MeOH or TNT in MeOH respectively. The final amount of tetryl on the strip was 2.2 mg and the final amount of TNT was 0.9 mg. One strip was left unadulterated. The strips were imaged with a Canon G12 camera. Although the differences in fluorescence intensity between strips could be seen in these images, due to

the glow of the UV light on the filter paper, they were somewhat washed out compared to the effect visible by eye. For this reason, the images were post-processed in Adobe Photoshop with a levels filter to improve colour and contrast.

The images reveal that TNT and tetryl can be detected by the naked eye using these test strips, but fluorescence was largely unaffected by application of water or methanol by itself.

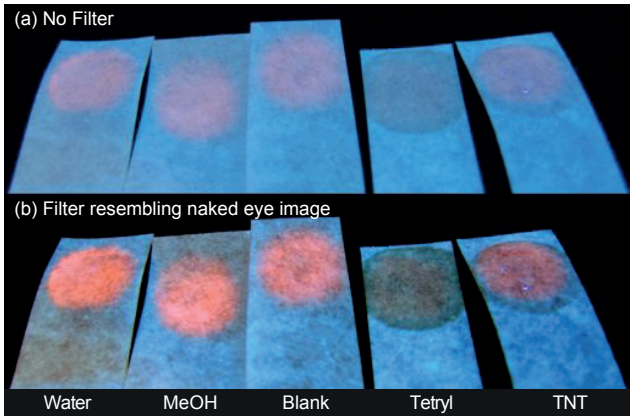

Figure 6.1: *Detection by eye. (a) Five test strips prepared with* $\mathbf{OMe}_{608}$ *on filter paper, exposed to drops of water, MeOH, Tetryl and TNT (detailed in SI). Quenching is observed for tetryl and TNT, although TNT still has some residual brightness in the centre. As the camera did not record the brightness of the QDs well under blacklight, post-processing was performed to improve contrast against background, to simulate what is seen by eye (b).*

6.3 SUPRAMOLECULAR GEL VEHICLE

An initial study into the feasibility of LMWO encapsulated nanoparticles was designed, including several types of nanomaterial to explore any differences or difficulties in their incorporation. The effect on the nanoparticle functional properties on the final gel was investigated. The LMWO itself is easy to synthesise on a large scale, with minimal workup and a long shelf life, giving it advantages over other peptide and dendrimer LMWOs, and requires only a single component, offering advantages over micellular systems.[267] Although gels using this material have previously been made with petrol and diesel fuel, octadec-1-ene (ODE) was trialled because it is a standard solvent of synthesis for many different nanomaterials, allowing

many different nanoparticles to be incorporated in the gel material, straight from the reactor.

Of particular relevance to the theme of this thesis was an attempt to use trioctylphosphine (TOP)/trioctylphosphine oxide (TOPO) capped CdSe@ZnS quantum dots as a gas sensor.

6.3.1 *Synthesis of multimodal gel/nanoparticle composites*

The gelator molecule **19** was synthesised *via* the formation of a di-acetal of D-mannitol with 1,1-dimethoxycyclohexane in DMF with acid catalysis (Scheme 6.1). No further work up was required beyond simple washing and drying.

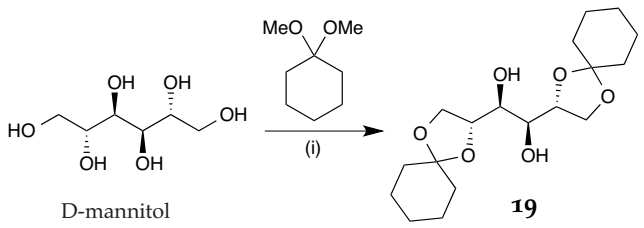

Scheme 6.1: *Scheme of gelator* **19** *synthesis. (i) DMF,* p-*TsOH, 60 °C, then TEA, 91%*

To create a typical gel, between 0.5 and 10 wt% (weight percent) of **19** was dissolved at 65 °C in 1 ml of ODE, containing the nanoparticles of interest. On cooling, gelation was tested by inversion. ODE solutions of TOP/TOPO capped CdSe/ZnS QDs, tetraoctylammonium bromide (TOAB) stabilised AuNPs, dodecanethiol (DDT) stabilised AuNPs, TOP stabilised Ni NPs, oleic acid (OA) stabilised Fe_3O_4 NPs, OA stabilised CoO NPs, and multiwall carbon nanotubes (MWCNTs) were all successfully converted into gels (stable to inversion) with 3 wt% or less of gelator.

6.3.2 *Characterisation and sensing results*

Physicochemical characterisation of all the gels was carried out, including TEM imaging of the distributions of nanomaterials within the fibrous network. In each case a small portion of the gel was cut with a scalpel and imaged. Fig. 6.3 shows a good dispersion of the NPs within the gel. The

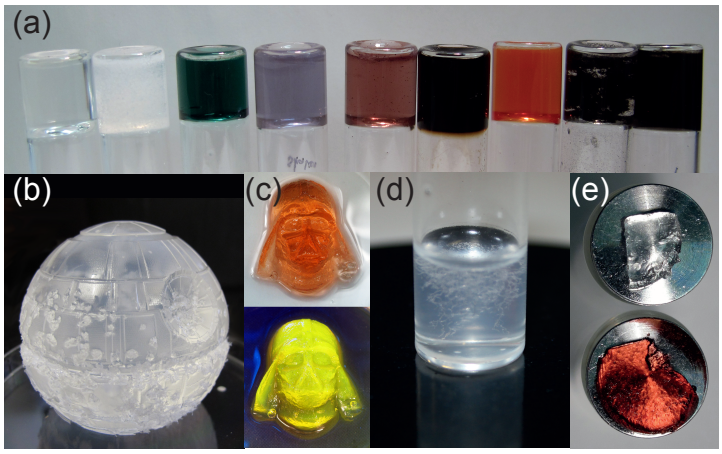

Figure 6.2: *(a) Images of different nanoparticle gels at 3 wt% loading unless noted, from left to right: Plain ODE gel, 10 wt% ODE gel, CoO NP gel, TOAB AuNP gel, DDT AuNP gel, Fe_3O_4 NP gel, CdSe/ZnS QD gel, virgin MWCNT gel and functionalised MWCNT gel. (b) Free standing 5% gel constructon (approximately 8 cm in diameter). (c) Free standing 4% QD gels under room and 365 nm light. (d) Growth of fibrous network during gelation of 10% ODE gel. (e) Samples of plain 4 wt% ODE gel before and after Au sputtering.*

melting point of the ODE gel was 65 °C, and the critical gelation concentration (CGC) was 0.357 wt%.

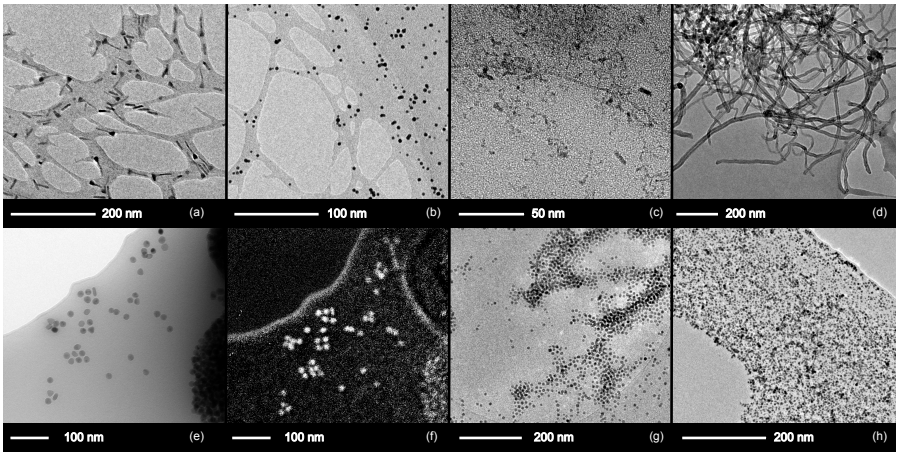

Figure 6.3: *TEM images of selected nanoparticle gels: (a) CoO NPs in gel matrix, (b) DDT stabilised AuNPs in gel matrix, (c) QDs in gel matrix, (d) functionalised MWCNTs in gel matrix, (e) Ni NPs in gel matrix, (f) elemental map of Ni in (e), (g) Fe_3O_4 NPs in gel matrix and (h) AuNPs as synthesised in a plain 4 wt% gel.*

Fluorescent gels were produced by the introduction of TOP/TOPO capped CdSe/ZnS quantum dots into the ODE solvent (Fig. 6.2a & c, 6.3c), and showed little shift in their emission peak, other than a slight reduction of fluorescence intensity, likely caused by the gel material scattering some of the incident and emissive light (Fig. 6.5a). There was also a corresponding change to the absorption spectrum with attenuation of the main absorption

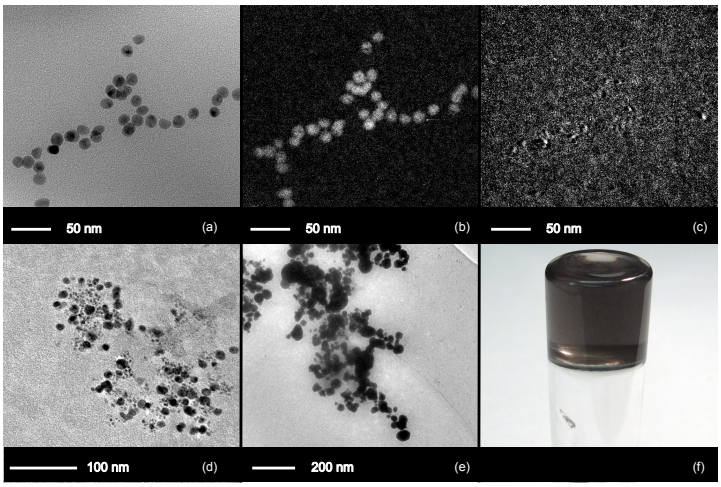

Figure 6.4: *(a) EFTEM of Ni NPs in gel matrix with zero loss (b) Ni Map TEM (c) O map TEM (d) TOAB-stabilised AuNPs in gel matrix (e) Ag NPs created by sputtering (f) Ni NP gel in glass vial.*

band at *ca.* 590 nm. These QD gels were applied to the sensing of nitrobenzene. A film of the QD gel cast on a glass slide, approximately 3 mm thick, was exposed to 197 ppm of nitrobenzene (natural vapour pressure at 25 °C) and fluorescence quenching was observed after 120 s (Fig. 6.5b). However the quenching effect was quite limited compared to the solution values reported (16 %Q compared to values in excess of 80 %Q).[125] This is likely due to low gas permeability of the gel, and could be improved by thinning the films (e. g. by spin coating them) or perhaps by adding targeting groups to the QD surface to improve binding to nitrobenzene.

Metal oxide NPs capped with oleylamine were easily incorporated in to the gels. Cobalt oxide nanostructures (wurtzite-golf-tee shapes, later published by Buck *et al*. [271] - Fig. 6.3a) were used to create an attractive green gel (Fig. 6.2a) and a magnetic gel was created from superparamagnetic ferrite NPs (Fe_3O_4) in ODE (Fig. 6.2a, Fig. 6.3g). A variety of strengths were created by varying the magnetic NP and gelator concentration and the resultant properties were probed by SQUID measurements (Fig. 6.5c - All SQUID measurements kindly performed by Dr Paul Southern). Although direct comparison between measured samples was difficult, data normalised against the maximum saturation magnetisation indicated that there was negligible impact of gelator concentration on magnetisation of a sample, suggesting that even high gelator concentrations create very stable

magnetic gels with little or no detrimental effect on the particle properties (for example no aggregation induced ripening).

Pure metal nanoparticles were also compatible with the gel, when coated with a range of oleophilic surfactants. AuNPs coated with TOAB or DDT were successfully incorporated, with the TOAB stabilised NPs remaining in a transparent gel long after the non-gelled solution had precipitated out (Fig. 6.2a, Fig. 6.3b). An interesting observation was mild aggregation of TOAB stabilised AuNPs in the gel, as evidenced by a red-shift in the absorption on gelling in comparison to the DDT stabilised material (Fig. 6.5d) and TEM (Fig. 6.4d). This suggests an ionic interaction between the charge stabilised NPs and the gelator, which is not exhibited by the DDT stabilised particles. Pure Ni nanoparticles were also successfully incorporated into the gel (Fig. 6.3e&f and Fig. 6.4f). Energy Filtered TEM (EFTEM) was used to illustrate the presence of Ni NPs in the gel as evidenced by the zero loss electron micrograph and Ni edge map in Fig. 6.3e&f. Oxygen edge mapping was also used to show that NiO was not present, indicating that no oxidation occurs to the NPs on gel formation (Fig. 6.4a-c). These Ni materials were tested as a supported catalyst for production of H_2 from aqueous NH_3BH_3 solution (0.4 M).[272, 273] Catalytic activity was observed at the phase boundary between hydrophobic gel and the solution, and 32 ml of H_2 was produced over 24 hours.

MWCNTs were incorporated into the gel *via* simple mixing, however as the gel cooled some clumping occurred (Fig. 6.2a). To reduce this phenomenon, the MWCNTs were coated with a pyrene conjugate *via* a literature procedure and thus became fully dispersible in ODE [274]. These could then be set into a long lasting and mechanically stable gel (Fig. 6.2a, Fig. 6.3d). Indeed shapes cast from these gels maintained their form for far longer than those cast from other nanomaterial gels, suggesting mechanical stabilisation of the matrix.

It was also discovered that noble metal nanoparticles could be generated *in-situ* within the gel matrix. Samples of gel were exposed to gold sputter (experimental details in Section 8.5.2) and remained clear after treatment with a few spots of gold. A strong red colour then developed after 24 hours (Fig. 6.2e). TEM confirmed the presence of remarkably uniform

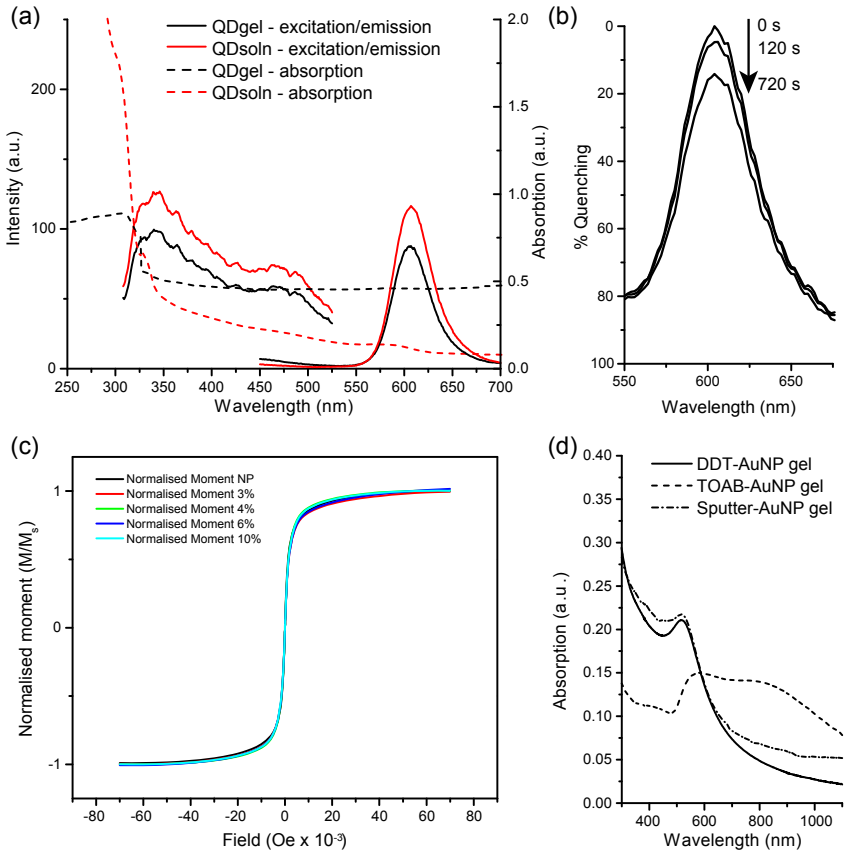

Figure 6.5: *(a) Fluorescence emission (ex:365 nm),excitation (em:605 nm), and absoprtion spectra (dashed) for the QD gel and ungelled solution. (b) Thin film of QD gel exposed to nitrobenzene vapour for varying time. (c) SQUID measurements show magnetic moment normalised against maximum moment for various wt% gels and the raw magnetic NPs. (d) Absorption of various AuNP gels created in different ways.*

AuNPs trapped in the gel matrix, in high concentration, without disrupting the structure of the gel (Fig. 6.3h), and the narrow SPR band indicated good monodispersity (Fig. 6.5d). The process was repeated with a silver sputter target and similar results were achieved (Fig. 6.4e). It is hoped in the future this material might be able to act as a SERS substrate, enhancing the Raman signal of analytes dropped onto, or mixed with the gel. However preliminary experiments in this direction suggested that it may suffer from the same problems as the system already discussed in Chapter 3, namely enhancement of the gelator material signals, with poor targeted binding to the analyte.

The recovery of nanoparticles from the gel was found to be straightforward, opening up potential applications as a stabilisation and storage medium for the particles, and an example is shown in Fig. 6.6. The gel-

nanoparticle composite was placed in a centrifuge tube with a small amount of ethanol and a drop of chloroform and vortexed to cause complete decomposition of the gel and emulsification of the ODE into the ethanol. This mixture was then centrifuged at 4000 rpm for 5 minutes to precipitate the nanoparticles.The supernatant containing the ODE and **19** in ethanol was decanted, and then the ethanol was removed under reduced pressure, leaving pristine ODE gel. The residual nanoparticles could be taken up in more ODE or other non-polar solvents.

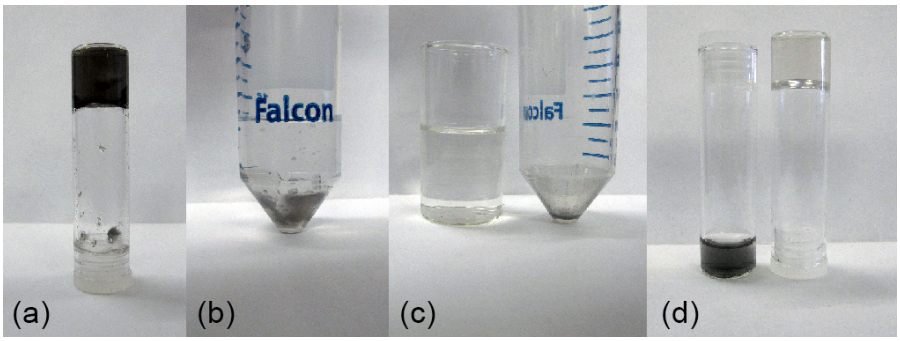

Figure 6.6: *Recovery of nanoparticles from the gel: (a) The Ni NPs in a gel matrix were freed by adding (b) a mixture of ethanol and chloroform to decompose the gel. After centrifugation (c) the supernatant was decanted to leave solid NPs in the tube and an ethanolic solution of the gel. (d) On removal of the ethanol the pristine gel was reformed and the NPs could be taken up in hexane.*

6.4 CONCLUSIONS

The immobilisation of QDs into media beyond the solution phase for sensing is a key requirement towards practical applications. Here two methods have been investigated, the first a simple deposition of QDs on to paper strips, for use as a solid state sensor for solution TNT and tetryl, and the second the formation of a nanoparticle containing gel.

The gel material was thoroughly investigated, and found to protect, encapsulate and act as a synthetic matrix for various nanomaterials. One particular sensing application, as a gas sensor for the toxic VOC and explosive-simulant nitrobenzene, was tested. However the sensor response was small, and this system would have to be optimised further, for example by refining the film thickness, or functionalising the surface of the QDs to drive a more favourable interaction.

7

CONCLUSIONS AND FUTURE WORK

7.1 CONCLUSIONS

The aim of this PhD project was to explore the potential of nanomaterials for the detection of explosives. In particular, methods with good sensitivity and specificity were sought, that might be easily reconfigurable to emerging threats. Two types of nanomaterials were experimented with - gold nanoparticles (AuNPs) and quantum dots (QDs), for the detection of explosives in solution phase, with some promising initial results for environmental monitoring applications.

A range of new AuNPs were created with a novel synthetic method. In particular this gave access to highly structured particles with pointed protrusions. These may prove useful for detection techniques that employ plasmon resonance to enhance Raman signals from an analyte physisorbed to a substrate, such as SERS. The mechanism behind the formation of the nanoparticles was investigated with TEM and spectroscopy, and a suggestion was made on the chemistry of particle formation and the shape control factors. The nanostars created were tested for SERS with an explosive taggant, DMDNB, but no Raman enhancement was observed, due to saturation of the surface of the particles by the capping ligand.

The focus then moved to creating a range of QD materials for building a solution-phase explosive detection array, potentially for analysis of waste-waters and run-off from testing ranges. Various colours of QD were synthesised with a range of different surface ligands. The different surface functionalities were created to employ non-specific binding of explosives *via* supramolecular binding principles, such as host-guest macrocyclic binding. A photo-ligation scheme was used to apply these functional moieties, on the end of a polyethylene glycol (PEG) spacer, to the QDs. The optical properties of the systems were characterised, and the length of the PEG spacer,

and the colour and constituent material of the QD were varied. It was determined that the shorter spacer and CdSe rather than InP QDs were preferable for the application at hand, due to better response towards explosives, and narrower emission peaks, which facilitate multichannel sensing.

A selection of these QDs were used to construct a sensory array, which was applied to the sensing of five nitro-explosives. In the first instance, the array was constructed in a single channel fashion, with one QD tested at a time. From this the best elements were selected to create a multichannel array, where three QDs were tested at a time, to give a fluorescence quenching pattern. These quenching patterns were then distinguished by two statistical machine-learning techniques, LDA and SVM, to explore the performance of the array. It was found that the multichannel array could classify explosives with more accuracy than the individual sensor elements by themselves, demonstrating the synergistic power of multichannel arrays, and limits of detection of < 1 ppm could be achieved.

Finally methods of immobilising QDs to move from solution-phase to gas-phase detection were investigated. The first method was simply drop-coating a sensor element onto a paper test strip, which was shown to quench (by naked eye) in the presence of TNT or tetryl, but not when common solvents were added. The second medium was a gel material that encapsulated nanoparticles straight from their solvent of synthesis. This hybrid organic-inorganic material was demonstrated with a range of different nanomaterials and shown to be an excellent passive medium for particle protection and even synthesis, whilst being recyclable. A film of the gel, containing fluorescent QDs, was explored as a sensor for explosive-simulant nitrobenzene. However, the quenching observed was slow to occur. Another novel AuNP synthesis within the gel matrix was also discovered, and considered for Raman sensing. However, a problem, similar to that observed with the nanostars created earlier, was encountered, where signals from the matrix/-capping ligands swamped those of any analyte.

It has been demonstrated that nanomaterials are sensors of interest for explosives, due to their interesting size-dependant properties. The QDs in solution proved easier to work with and more simple to implement in a sensing array than either of the attempted Raman substrates. Raman is a

viable system for explosive detection, but further work must go into developing the systems here for good results to be obtained. In particular, ways of isolating the particles from their synthetic or supporting matrix are needed to prevent the problems encountered. The QD system, although nominally successful in achieving the desired selectivity and reconfigurability, could have improved sensitivity, and is at a very early stage, utilising laboratory solvents and equipment. Now it must be developed into more robust technology that can be applied widely in the field. One unexpected success was the simple paper test strip, and a key conclusion is that "simpler is often better" when it comes to sensor systems, allowing for more rapid development and easier deployment.

7.2 FUTURE WORK

The work on AuNPs should now focus on the nanostars created with 1,3-cyclohexanedione. A study into the effect of concentration and ratio of gold to reductant are necessary to see if the concentration of surface bound ketone can be reduced, allowing for applications in SERS. Other options might be to maintain the synthesis as it is, but subsequently remove the excess surfactant with a physical or chemical cleaning step, such as exposure to an oxygen plasma. Once a clean, pointed gold surface is obtained, a substrate of the particles can be created and tests on the enhancement factor and limits of detection can be performed.

The QD array shows much promise, and the obvious next step is to trial the sensing under more challenging conditions, for example introducing pollutants and complex backgrounds into the sensing media. The ideal experiment would take TNT contaminated river/run-off water and use a solid-phase extraction device, eluted with methanol to prepare a sample. The TNT concentration in this sample would be quantified by LC-MS, and then tested with the QD sensor array to firstly test if quenching occurs, and then test if the observed quenching corresponds to the pre-determined calibration curve for TNT with the array.

There is also potential to optimise the array, experimenting with other surface functionality, larger cavitands or extending the array to a fourth element (ideally emitting at around 580 nm) to further improve discrimination. Another study of interest would be to probe the mechanics of the sensor response using photo-electrochemistry and techniques such as rapid pump-probe spectroscopy to follow the PET step. Modelling of the cavitands and their interaction with analytes would also add useful information on targeted ligand design, particularly in conjunction with host-guest binding studies using isothermal calorimetry or NMR.

Once a good working array is obtained, an interesting development would be the creation of a lateral flow sensor, that passes contaminated liquid over the array elements immobilised on a nitro-cellulose or similar support, then fluorescence can be measured with a simple UV-LED excitation source and camera based imaging tool. It is important at this stage to keep the sensor as simple as possible, thus lateral flow is preferred over a more complex microfluidic system.

Although the gels produced may not be the best sensors, they did demonstrate other interesting properties. Future work should seek to quantify the change in structural properties with integration of the MWCNTs, and potential for magnetic hyperthermia induced release of a substance encapsulated in the gel, by using magnetic nanoparticles as a heating mechanism to melt the capsule. For Raman based sensing purposes, other gel media could be explored for AuNP synthesis that may have a much lower Raman cross section, and therefore might prove more suitable for analyte detection.

8

MATERIALS AND METHODS

8.1 GENERAL METHODS AND MATERIALS

8.1.1 *Chemicals*

Unless stated otherwise, reagents were used as supplied from Sigma Aldrich or Alfa Aesar, without further purification. All water used was deionised (>15 MΩ), and room temperature (RT) was around 20 °C. Other solvents were HPLC grade and used as provided, with the exception of DMF, which was dried over 4 Å molecular sieves. Thin layer chromatography (TLC) was performed on Merck aluminium backed silica gel 60 F254 plates. Visualisation was achieved with UV light, iodine on silica or $KMnO_4$ in basic aqueous solution, depending on the compound. Transformations were carried out under an inert atmosphere of nitrogen or argon and Schlenk techniques were used where necessary for more sensitive procedures. Flash column chromatography was carried out on silica gel 60 under positive pressure. All solvent ratios are reported as volume/volume.

Copper on activated carbon was prepared by the method of Lipshutz *et al.*[216] The literature suggests a loading of $\sim$ 1 mmol/g of Cu, however this value may be lower in reality, as larger amounts than suggested were required for complete reaction in these preparations.

Explosive samples (TNT, tetryl, RDX and PETN) were purchased from AccuStandard as certified 1 mg/mL standards in either MeOH or MeOH/MeCN dependant on solubility. These were then diluted in spectrophotometric grade MeOH to the required 1 mM concentration.

8.1.2 *Instrumentation*

UV-visible absorption spectroscopy (UVVis) spectroscopy was performed with a Perkin-Elmer Lamda-25 instrument, scanning between 250 and 1100 nm at a typical rate of 960 nm/min with 1 nm resolution. Samples were measured in 10 mm path length quartz cuvettes, or PMMA semi-microcuvettes where necessary.

^{1}H NMR spectra were collected on a Brucker Avance III 600 with cryoprobe (600/150 MHz); or Avance 500 (500/125 MHz) spectrometer, in deuterated solvents. Where necessary, solvent suppression was used during data collection. Chemical shifts are given in ppm, relative to the residual protonated solvent. Coupling constants are measured in Hz, and quoted to 0.1 Hz, with an accuracy of $\pm$ 0.1 Hz due to digital resolution.

TEM samples were prepared by dropping 2 or 3 drops of undiluted suspension onto holey carbon-coated copper or gold grids and drying in air. TEM micrographs were collected using a Jeol 1010 microscope, fitted with a Gatan Orius digital camera at a beam acceleration of 80-100 kV or a high-resolution Jeol 2010 system operating at 200 kV. Image processing and particle counting were performed with Gatan DigitalMicrograph and ImageJ software. EDX was performed on TEM samples with an Oxford Instruments EDX spectrometer operating in either point-analysis or mapping (Scanning TEM) mode, and data analysed in the Aztec software package. Energy filtered TEM measurements were collected using a Philips CM200 FEG TEM with an ISIS EDX system and Gatan Imaging filter for EELS at the Leeds EPSRC Nanoscience and Nanotechnology Research Equipment Facility.

SEM images were collected from gold coated or uncoated samples, on a field emission Jeol 6700F FEG SEM operating at 5 kV and environmental Hitatchi S-3400N SEM operating at 10 kV.

X-ray Photoelectron Spectroscopy (XPS) measurements were performed with a Thermo monochromated aluminium k-alfa photoelectron spectrometer, using monochromic Al-Kα radiation. Data was analysed with CasaXPS software.

Normal and high resolution mass spectrometry (MS) data were collected under positive or negative Electrospray Ionisation (ESI) on a ThermoFisher

Scientific LTQ Velos or Waters LCT Premier XE. Molecular ions or other major peaks are reported.

FT-IR spectra were collected on a Bruker Alpha Platinum ATR unit between 400 and 4000 cm^{-1}

Centrifugation was performed with a Heraeus Megafuge 8 at 4500 rpm or less (3260×g or less) in 50 mL tubes or in a Eppendorf MiniSpin at 13400 rpm (12100×g) for ultracentrifugation in 2 mL eppendorfs.

Fluorescence spectra were collected on a Horiba FMax 4 instrument running FluorEssence software. Spectra were corrected for lamp and instrument response. Entrance and exit slit widths were typically 5 nm or less. Emission spectra were measured with fixed excitation wavelength and emission measured from $>$ 5 nm below this wavelength to a maximum of 700 nm. Excitation spectra were measured by fixing the emission monochromator at the spectral maxima of the sample, and varying excitation wavelength from 300 nm to $>$ 10 nm above the fixed point. Quantum yield (QY) measurements were performed with a built in integrating sphere unit, and liquid samples were measured in small cylindrical glass tubes. Neutral density filters of 2.5%, 1% or 0.5% were used to protect the detector during the measurements. The full QY procedure is described in Section 4.3.

Fluorescence lifetimes were collected on an Edinburgh Instruments LifeSpec-ps with 405 nm pulsed laser excitation and with a cooled (-18 °C) TCSPC detector. Fluorescence decays were measured over 100 ns pulses with 4096 collection channels, at the emission maximum of the sample. Exponential decays were then fitted with the FAST software package, using 1, 2 or 3 exponentials or a single stretched exponential. In each case the instrument response function was included (measured with an empty cuvette), and tail fitting was used to obtain the optimum fit, as measured by χ^2_R.

8.2 CHARACTERISATION TABLE

Compound short names (full systematic names given where possible in Section 8.3 and Section 8.4), and their reference number used in this thesis are given in Table 8.1, along with the characterisation methods applied. 'Other

NMR' referrers to 2D or advanced NMR techniques such as DOSY. 'MP' is melting point analysis. A dash (-) indicates data that could not be obtained, an NA that the method was not applicable, and an X that the data is presented below.

Table 8.1: *Characterisation table*

Compound Short Name	Reference	^{1}H	^{13}C	Other NMR	MS	MP
$N_3-PEG-N_3$	**1**	X				NA
$N_3-PEG-NH_2$	**2**	X				NA
LA−PEG−N_3	**3**	X	X	X	X	NA
LA−PEG−NH_2	**4**	X				NA
LA−PEG−OH	**5**	X				NA
LA−PEG−OMe	**OMe**	X	X			NA
$N_3-TEG-N_3$	**6**	X				NA
$N_3-TEG-NH_2$	**7**	X				NA
LA−TEG−N_3	**8**	X				NA
LA−TEG−OH	**OH**	X				NA
monopropargyl calix[4]arene	**9**	X	X	X	X	X
monotosyl-β-cyclodextrin	**10**	X	X	X		X
monotosyl-β-permethylcyclodextrin	**11**	X	X	X		-
monopropargyl-β-cyclodextrin	**12**	X	X	X	X	X
bis-imidazolium bromide	**BisIm**	X			X	X
glycoluril hexamer	**G6**	X			X	X
cucurbit[7]uril	**CB[7]**	X	X		X	X
cucurbit[7]uril-OH	**CB[7]monOH**	X	X		X	X
monopropargyl cucurbit[7]uril	**fCB[7]**	X	-	-	X	-
dopamine succinate	**13**	X	X	X		NA
LA-PEG-dopamine	**14**	X	X	X		-
monopropargyl naphthalene	**15**	X	X		X	X
LA-TEG-calixarene	**CX**	X	X	X	X	NA
LA-TEG-cyclodextrin	**CD**	X	X	X	X	NA
LA-TEG-naphthalene	**16**	X	X	X	X	NA
LA-PEG-calixarene	**17**	X	X	X		NA
LA-PEG-naphthalene	**18**	X	X	X		NA
LMWOrganogelator	**19**	X				X

8.3 NANOPARTICLE LIGAND SYNTHESES

8.3.1 *PEG linkers*

*O,O′-Bis(2-azidoethyl)polyethylene glycol (**1**)*

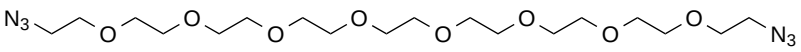

Based on a procedure from Susumu *et al.*[206] PEG400 (10 g, 24.15 mmol) and methane sulfonylchloride (MsCl) (4.1 mL, 53.1 mmol) were added to a flask with THF (30 mL) and cooled to 0 °C under argon. Triethylamine (8.1 mL, 57.97 mmol) was added dropwise whilst stirring over 15 mins. The reaction was allowed to warm to RT and stirred for 18 hrs. The mixture was diluted with water (30 mL) and $NaHCO_3$ (2.0 g, 24 mmol) was added.

Sodium azide (4.24 g, 65.2 mmol) was added to the biphasic mixture and the flask equipped with a still head. The THF was distilled off, and once only water remained, the reaction was heated at reflux for 18 hrs.

Once cooled the product was extracted into chloroform and dried over $MgSO_4$, before removing the solvent under reduced pressure to give a colourless liquid. This was purified by column chromatography with 20:1 chloroform/MeOH, and the appropriate fractions were combined and dried under high vacuum to give the colourless oily product (8.3 g, 74%). ^{1}H NMR (600 MHz $CDCl_3$) δ_H 3.62-3.69 (∼32H, m), 3.39 (4H, t, *J*=5.0, N_3CH_2).

*O-(2-Aminoethyl)-O′-(2-azidoethyl)polyethylene glycol (**2**)*

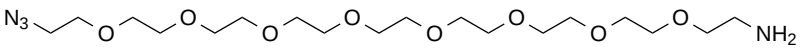

Based on a procedure from Susumu *et al.*[206] Compound **1** (6.0 g, 12.9 mmol) was charged to a flask with EtOAc (75 mL) and 1M HCl (30 mL). The biphasic mixture was stirred at 0 °C whilst triphenylphosphine (3.73 g, 14.2 mmol) in EtOAc (50 mL) was added dropwise from a dropping funnel over approx. 45 min. Once addition was complete, the reaction was allowed to warm to RT and stirred for 18 hrs.

The aqueous layer was seperated and washed with two portions of EtOAc (50 mL), then basified with KOH (15 g) added portion wise whilst cool-

ing the flask in ice. Once complete, the product was extracted with EtOAc (5×50 mL). The organic layers were combined and dried over $MgSO_4$ before solvent removal to yield a colourless oil (3.67 g, 64.9%). ^{1}H NMR (500 MHz $CDCl_3$) δ_H 3.70-3.60 (m), 3.56 (2H, t, *J*=5.2, O$CH_2$$CH_2$$NH_2$), 3.39 (2H, t, *J*=4.9, N_3CH_2), 2.90 (2H, t, *J*=5.0, $OCH_2CH_2NH_2$).

*O-(2-(N-5-(1,2-Dithiolan-3-yl)pentanamide)ethyl)-O′-(2-aziodethyl)polyethylene glycol (**3**)*

NMR numbering schemes are continuous for similar molecules, unless otherwise noted.

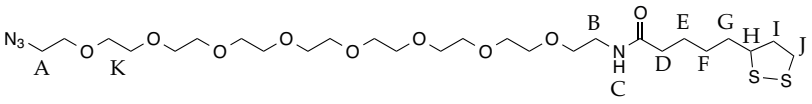

Based on a procedure from Susumu *et al.*[206] **2** (1 g, 2.36 mmol), DCC (0.49 g, 2.36 mmol), and 4-dimethylaminopyridine (DMAP) (57 mg, 0.47 mmol) were dissolved in DCM (15 mL) and cooled to 0 °C. Lipoic acid (0.49 g, 2.36 mmol) in DCM (9 mL) was added dropwise. The reaction was allowed to warm to RT and stirred for 18 hrs. The cloudy mixture was filtered through a celite plug and the solvent was removed under reduced pressure. The residue was dissolved in water (100 mL) and washed twice with hexane. The aqueous layer was then saturated with $NaHCO_3$ and extracted with DCM (3×50 mL). The organic layer was dried over $MgSO_4$ and the solvent was mostly removed. The residue purified by column chromatography with 20:1 chloroform/MeOH to give a yellow oil (1.44 g, 97%). ^{1}H NMR (600 MHz $CDCl_3$) δ_H 6.22 (1H, br.s, H_C), 3.60-3.50 (∼27H, m, H_K), 3.48 (1H, m, *J*=4.9, H_H), 3.37 (2H, t, *J*=5.0, H_B), 3.32 (2H, t, *J*=4.9, H_A), 3.15-3.02 (2H, m, H_J), 2.40 (1H, m, H_I), 2.12 (2H, t, *J*=7.7, H_D), 1.84 (1H, m, H_I), 1.61 (4H, m, $H_{E,G}$), 1.39 (2H, m, H_F). ^{13}C NMR (150 MHz $CDCl_3$) δ_C 172.9, 78.3, 70.6 (m), 51.7, 50.7, 41.2, 40.3, 39.2, 38.6, 37.7, 36.4, 35.6, 34.7, 33.9, 29.7, 29.0, 24.6. MS (ESI+) *m/z* 605-625 ([M]$^+$ $C_{26}H_{50}N_4O_9S_2$ calc. 626.3019).

*O-(2-(N-5-(1,2-Dithiolan-3-yl)pentanamide)ethyl)-O′-(2-aziodethyl)polyethylene glycol (**4**)*

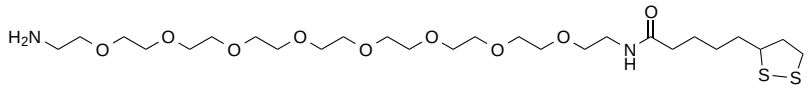

Based on a procedure from Susumu *et al.*[206] Compound **3** (0.25 g, 0.40 mmol) was charged to a flask with THF (5 mL). Triphenylphosphine (0.16 g, 0.60 mmol) was added and the mixture stirred at RT for 30 min. Water (0.1 mL) was added and the reaction was stirred overnight. The reaction was monitored by TLC, and extra triphenylphosphine (0.1 g) and water (0.1 mL) was added if necessary. All solvents were removed and the residue was redissolved in EtOAc (10 mL). 1M HCl (10 mL) was added slowly and the organic layer was removed and set aside. The aqueous layer was washed with EtOAc, and then basified to pH 9 with Na_2CO_3 and extracted with DCM. The DCM layer was dried over $MgSO_4$ and the solvent was removed under reduced pressure to yield a yellow oil (0.116 g, 50%). ^{1}H NMR (600 MHz $CDCl_3$) δ_H 3.70-3.60 (~32H, m, H_K), 3.60-3.50 (1H, m, $H_{H,K}$), 3.43 (2H, m, H_B), 3.13 (2H, m, H_J), 2.89 (2H, m, H_A), 2.44 (1H, m, H_I), 2.19 (2H, m, H_D), 1.89 (1H, m, H_I), 1.66 (4H, m, $H_{E,G}$), 1.45 (2H, m, H_F).

*O-(5-(1,2-Dithiolan-3-yl)pentanoate)polyethylene glycol (***5***)*

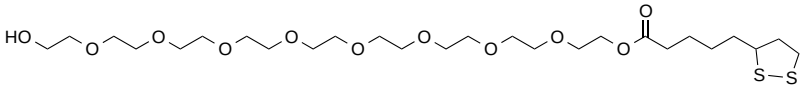

Based on a procedure from Uyeda *et al.*[275] PEG400 (10.0 g, 24.1 mmol), lipoic acid (0.50 g, 2.41 mmol) and DMAP (89 mg, 0.7 mmol) were dissolved in DCM (15 mL) and cooled to 0 °C under argon. DCC (0.50 g, 2.41 mmol) in DCM (3 mL) was added dropwise and the reaction was stirred for 1 hour before being warmed to RT. After stirring for a further 18 hrs, the mixture was filtered over a celite plug and the solvent was removed. The residue was mixed with saturated $NaHCO_3$ and the product extracted with EtOAc. The organic layers were combined and reduced in volume before purification with column chromatography in 15:1 chloroform/MeOH. (This had to be done quickly as the product tended to form an insoluble gel over time). The desired fractions were dried under vacuum to yield a yellow oil (0.90 g, 60%). ^{1}H NMR (600 MHz $CDCl_3$) δ_H 4.20 (2H, t, J=4.9, H_B), 3.70-3.60 (~29H, m, H_K), 3.58 (2H, t, J=4.5, H_A), 3.54 (1H, t, J=6.0, H_H), 3.13 (2H, m, H_J), 2.44 (1H, m, H_I), 2.33 (2H, t, J=7.5, H_D), 1.88 (1H, m, H_I), 1.65 (4H, m, $H_{E,G}$), 1.44 (2H, m, H_F).

O-*(5-(1,2-Dithiolan-3-yl)pentanoyl)*-O′*-methylpolyethylene glycol (***OMe***)*

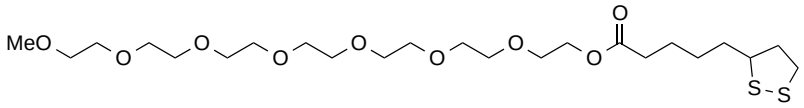

Based on a procedure adapted from Susumu *et al.*[206] Methoxypolyethylene glycol 350 (1.00 g, 2.86 mmol), lipoic acid (0.59 g, 2.86 mmol) and DMAP (96 mg, 0.86 mmol) were dissolved in DCM (25 mL) at 0 °C. DCC (0.59 g, 2.86 mmol) in DCM (5 mL) was added dropwise whilst stirring and cooling was maintained for one hour. After this time the reaction was allowed to return to RT and stirred for a further 18 hrs. The mixture was filtered over celite and the solvent was removed under reduced pressure. The crude was washed with water and 1M HCl and dried over $MgSO_4$. Solvent removal yielded a yellow oil (1.24 g, 82%). ^{1}H NMR (600 MHz $CDCl_3$) δ_H 4.19 (2H, t, J=4.9, H_B), 3.70-3.55 (∼28H, m, H_K), 3.51 (3H, m, J=4.9, $H_{H,K}$), 3.34 (3H, s, OMe), 3.12 (2H, m, H_J), 2.42 (1H, m, H_I), 2.32 (2H, t, J=7.5, H_D), 1.87 (1H, m, H_I), 1.65 (4H, m, $H_{E,G}$), 1.43 (2H, m, H_F).

8.3.2 *TEG linkers*

O,O′-*Bis(2-azidoethyl)ethylene glycol (**6**)*

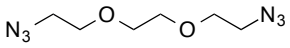

Based on a procedure from Susumu *et al.*[206] Triethylene glycol (5.0 g, 33.3 mmol) and methanesulfonyl chloride (5.6 mL, 72.3 mmol) were added to a flask with THF (30 mL) and cooled to 0 °C under argon. Triethylamine (11.1 mL, 79.6 mmol) was added dropwise whilst stirring over 15 mins. The reaction was allowed to warm to room temperature and stirred for 18 hrs. The mixture was diluted with water (30 mL) and $NaHCO_3$ (2.8 g, 33.3 mmol) was added. Sodium azide (4.24 g, 65.2 mmol) was added to the biphasic mixture and the flask equipped with a still head. The THF was distilled off, and once only water remained the reaction was heated at reflux for 18 hrs.

Once cooled the product was extracted into chloroform and dried over $MgSO_4$, before removing the solvent under reduced pressure to give a colourless liquid. Flash chromatography of the residue in 20:1 chloroform/MeOH, gave **6** as a colourless oil (6.1 g, 91%). ^{1}H NMR (600 MHz $CDCl_3$) δ_H 3.67 (8H, m), 3.36 (4H, t, *J*=4.9, N_3CH_2).

O-(2-*Aminoethyl*)-O′-*(2-azidoethyl)ethylene glycol (**7**)*

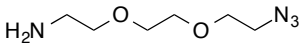

Based on a procedure from Susumu *et al.*[206] A flask was charged with compound **6** (7.0 g, 35.0 mmol), EtOAc (100 mL) and 1M HCl (77 mL). The biphasic mixture was stirred at 0 °C whilst triphenylphosphine (9.62 g, 36.7 mmol) in EtOAc (100 mL) was added dropwise from a dropping funnel over *ca.* 45 min. Once addition was complete, the reaction was allowed to warm to RT and stirred for 18 hrs.

The aqueous layer was separated and washed with two portions of EtOAc (75 mL), then basified with KOH (35 g) added portion-wise whilst cooling the flask in ice. Once complete, the product was extracted with EtOAc (5×50 mL). The organic layers were combined and dried over $MgSO_4$ be-

fore solvent removal to yield **7** as a colourless oil (3.75 g, 61%). ^{1}H NMR (600 MHz $CDCl_3$) δ_H 3.43 (8H, m), 3.31 (2H, t, *J*=4.9, N_3CH_2), 3.17 (2H, t, *J*=5.0, CH_2NH_2).

O-*(2-(*N-*5-(1,2-Dithiolan-3-yl)pentanamide)ethyl)*-O′-*(2-azidoethyl)ethylene glycol (**8**)*

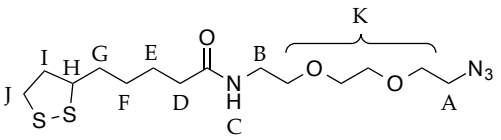

Based on a procedure from Susumu *et al.*[206] Compound **7** (1.0 g, 5.7 mmol), DCC (1.18 g, 5.7 mmol), and DMAP (140 mg, 1.15 mmol) were dissolved in DCM (15 mL) and cooled to 0 °C. Lipoic acid (1.18 g, 7.7 mmol) in DCM (10 mL) was added dropwise. The reaction was allowed to warm to RT and stirred for 18 hrs. The cloudy mixture was filtered through a celite plug and the solvent was removed under reduced pressure. The residue was dissolved in water (100 mL) and washed twice with hexane. The aqueous layer was then saturated with $NaHCO_3$ and extracted with DCM (3×50 mL). The organic layer was dried over $MgSO_4$ and the volume of solvent reduced. Flash chromatography of the residue in 20:1 chloroform/MeOH to give compound **8** as a yellow oil (1.55 g, 75%). ^{1}H NMR (600 MHz $CDCl_3$) δ_H 6.03 (1H, br.s, H_C), 3.66 (2H, t, *J*=4.9, H_K), 3.62 (4H, m, H_K), 3.52 (3H, m, $H_{K,H}$), 3.42 (2H, m, H_B), 3.37 (2H, t, *J*=4.9, H_A), 3.11 (2H, m, H_J), 2.42 (1H, m, H_I), 2.15 (2H, m, H_D), 1.88 (1H, m, H_I), 1.65 (4H, m, $H_{E,G}$), 1.42 (2H, m, H_F).

O-*(5-(1,2-Dithiolan-3-yl)pentanoyl)triethylene glycol (**OH**)*

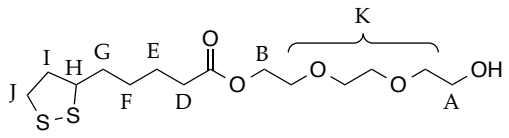

Based on a procedure from Uyeda *et al.*[275] Triethylene glycol (5.0 g, 33.3 mmol), lipoic acid (0.70 g, 3.39 mmol) and DMAP (120 mg, 0.98 mmol) were dissolved in DCM (40 mL) and cooled to 0 °C under argon. DCC (0.71 g, 3.44 mmol) in DCM (4 mL) was added dropwise and the reaction

was stirred for 1 hour before being warmed to room temperature. After stirring for a further 18 hrs, the mixture was filtered over a celite plug and the solvent was removed. The residue was mixed with saturated $NaHCO_3$ and the product extracted with EtOAc. The organic layers were combined and reduced in volume before flash chromatography in 15:1 chloroform/MeOH. The desired fractions were dried under vacuum to yield a yellow oil (0.80 g, 70%). ^{1}H NMR (600 MHz $CDCl_3$) δ_H 4.24 (2H, t, *J*=4.5, H_B), 3.87-3.39 (11H, m, $H_{K,A,H}$), 3.15 (2H, m, H_J), 2.45 (1H, m, H_I), 2.35 (2H, t, *J*=7.5, H_D), 1.90 (1H, m, H_I), 1.70 (4H, m, $H_{E,G}$), 1.45 (2H, m, H_F).

8.3.3 *Calixarane system*

5,11,17,23-tetra-tert-*butyl-28-propargylcalix[4]arene-25,26,27-triol (**9**)*

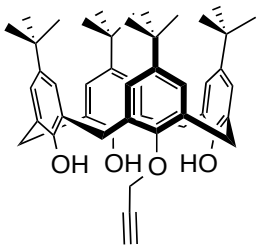

Two methods were attempted to produce calixarene **9**. The first used K_2CO_3 as the base,[208] and the second adapted a procedure that employed CsF.[209]

K_2CO_3 (19 g, 0.14 mmol), *p-tert*-butyl-calix[4]arene (100 mg, 0.15 mmol) and propargyl bromide (80% in toluene, 35 μL, 0.31 mmol) were stirred at reflux in acetone (15 mL) overnight.

The reaction mixture was then cooled to room temperature and filtered over celite. The celite plug was then washed with DCM. The filtrate was concentrated to dryness and purified by chromatography with 1:1 DCM/hexane. The relevant fractions were combined and solvents removed to give a white solid (25 mg, 24%). MP = 181 °C. ^{1}H NMR (600 MHz $CDCl_3$) δ_H 10.12 (1H, s, OH), 9.27 (1H, s, OH), 7.10 (2H, s, H_{Ar}), 7.05 (4H, m, H_{Ar}), 6.99 (2H, d, *J*=2.6, H_{Ar}), 4.93 (2H, d, *J*=2.4, CH_2CCH), 4.47 (2H, d, *J*=13.2, ArCH_2Ar), 4.28 (2H, d, *J*=13.5, ArCH_2Ar), 3.44 (4H, d, *J*=13.5, ArCH_2Ar), 2.73 (1H, t, *J*=2.3, CH_2C*CH*), 1.22 (9H, s, *t*-Bu), 1.21 (18H, s, *t*-Bu), 1.19 (9H, s, *t*-Bu). ^{13}C

NMR (150 MHz $CDCl_3$) δ_C 149.3, 148.7, 148.4, 147.9, 143.7, 143.4, 133.7, 128.2, 128.1, 127.8, 126.7, 125.9, 125.8, 125.7, 125.6, 78.05, 63.6, 53.6, 34.4, 34.0, 33.9, 33.1, 32.7, 31.6, 31.5, 31.3. MS (ESI+) *m/z* 687.4083 ($[M+H]^+$ $C_{47}H_{59}O_4$ calc. 687.4408).

In the second procedure: CsF (18 mg, 0.12 mmol) and *p-tert*-butyl-calix[4]-arene (65 mg, 0.1 mmol) were stirred in DMF (5 mL), and propargyl bromide (80% in toluene, 0.11 mL, 1 mmol) was added. The reaction was stirred at 40 °C for 24 hrs, before quenching with 2 M HCl and extracting into DCM (40 mL). The organic layer was washed with water, and dried over $MgSO_4$, before removing the solvent under reduced pressure. The residue was redissolved in 1:1 DCM/MeOH and the solid (unreacted started material) was filtered off. The filtrate was dried under reduced pressure to give the desired product, although contaminated with DMF. This was removed by dissolving the product in a small amount of DCM and washing with a large amount of water, before drying the organic layer over $MgSO_4$ and removing the solvent under reduced pressure to give a white solid (19 mg, 28%).

*Lipoic acid-triethyleneglycol-calix[4]arene (***CX***)*

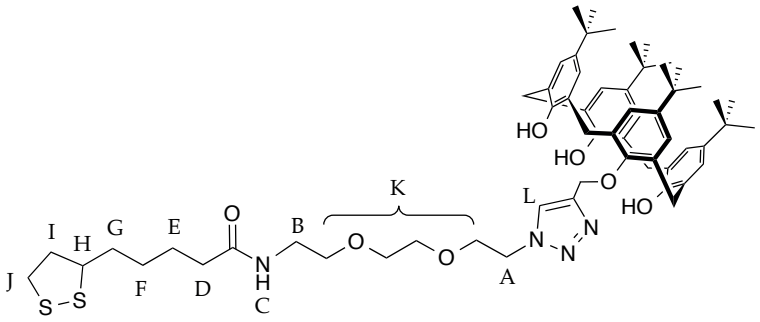

Compound **8** (33 mg, 0.093 mmol) was mixed with Cu on an activated carbon support (50 mg).[216] Monopropargyl calixarene **9** (64 mg, 0.093 mmol) was dissolved in 2 mL of dioxane and added followed by triethylamine (0.1 mmol, 14 μL). The reaction was heated at 70 °C, with stirring, for 3 days. The product was purified over a silica plug, and solvents removed to give a thick orange oil (96 mg, 98%). ^{1}H NMR (600 MHz $CDCl_3$) δ_H 10.07 (1H, s, OH), 9.31 (2H, s, OH), 8.40 (1H, s, H_L), 7.12 (2H, s, H_{Ar}), 7.05 (4H, m, H_{Ar}), 6.97 (2H, s, H_{Ar}), 6.15 (1H, br.s, H_C), 5.32 (2H, s, OCH_2C), 4.71 (2H, t, *J*=4.9, H_A), 4.42 (2H, d, *J*=13.2, ArCH_2Ar), 4.18 (2H, d, *J*=13.5, ArCH_2Ar), 4.01 (2H,

t, *J*=4.9, H_K) 3.71-3.40 (13H, m, ArCH_2Ar+$H_{K,B,H}$), 3.14 (2H, m, H_J), 2.45 (1H, m, H_I), 2.15 (2H, t, *J*=7.1,H_D), 1.90 (1H, m, H_I), 1.66 (4H, m, $H_{E,G}$), 1.42 (2H, m, H_F), 1.21 (9H, br s, *t*-Bu), 1.20 (27H, m, *t*-Bu). ^{13}C NMR (150 MHz $CDCl_3$) δ_C 173.1, 149.2, 148.8, 148.2, 147.7, 143.9, 143.5, 143.3, 133.7, 128.3, 128.2, 127.6, 126.7, 125.9, 125.0, 70.7, 70.4, 70.1, 70.0, 69.6, 67.2, 63.9, 56.6, 50.9, 50.7, 40.4, 39.3, 38.6, 36.4, 34.8, 34.4, 34.1, 34.0, 33.0, 32.4, 31.6, 31.3, 29.0, 25.5. HRMS (ESI+) *m/z* 1049.5801, 1071.5546 ($[M+H]^+$ $C_{61}H_{85}N_4O_7S_2$ calc. 1049.5860, $[M+Na]^+$ calc. 1071.5679).

*Lipoic acid-polyethyleneglycol-calix[4]arene (**17**)*

Compound **3** (79 mg, 0.13 mmol) was mixed with Cu on an activated carbon support (50 mg).[216] Monopropargyl calixarene **9** (86 mg, 0.13 mmol) was dissolved in 5 mL of dioxane and added followed by triethylamine (0.14 mmol, 19 μL). The reaction was heated at 70 °C, with stirring, for 3 days. The product was purified over a silica plug, and solvents removed to give a thick orange oil (162 mg, 98%). ^{1}H NMR (600 MHz $CDCl_3$) δ_H 10.06 (1H, s, OH), 9.30 (2H, s, OH), 8.33 (1H, s, H_L), 7.09 (2H, s, H_{Ar}), 7.02 (4H, m, H_{Ar}), 6.95, (2H, m, H_{Ar}), 6.22 (1H, br.s, H_C), 5.32 (2H, s, OCH_2C), 4.68 (2H, t, *J*=4.9, H_A), 4.39 (2H, d, *J*=13.0, ArCH_2Ar), 4.17 (2H, d, *J*=13.0, ArCH_2Ar), 3.96 (2H, t, *J*=4.9, H_K), 3.66-3.51 (∼30H, m, H_K, H_H), 3.42 (4H, d, *J*=13.0, ArCH_2Ar), 3.37 (2H, m, H_B), 3.19-3.07 (2H, m, H_J), 2.44 (1H, m, H_I), 2.18 (2H, t, *J*=7.1, H_D), 1.90 (1H, m, H_I), 1.66 (4H, m, $H_{E,G}$), 1.45 (2H, m, H_F), 1.18 (36H, m, *t*-Bu). ^{13}C NMR (150 MHz $CDCl_3$) δ_C 172.9, 161.2, 160.6, 149.2, 148.4, 147.8, 146.8, 143.7, 143.3, 143.1, 135.3, 133.7, 133.6, 128.3, 128.2, 127.8, 127.6, 127.0, 126.7, 126.0, 125.8, 125.1, 117.2, 70.8-70.5, 70.3, 70.0, 69.9, 69.7, 68.7, 65.6, 63.8, 63.5, 62.7, 61.3, 26.5, 25.5.

8.3.4 *Cyclodextrin system*

*Mono(6-O-*p*-toluenesulfonyl)-β-cyclodextrin (**10**)*

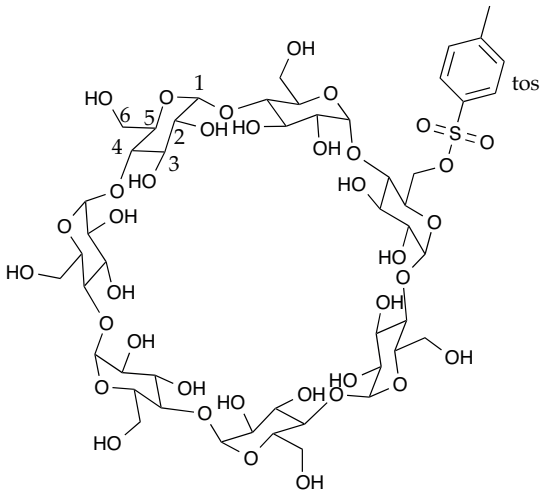

Synthesised from Byun *et al.*[211] β-cyclodextrin (2.5 g, 2.2 mmol) was dissolved in water (56 mL) at 60 °C, then cooled to RT with stirring. Finely powdered *p*-tosylimidazole (1.96 g, 8.8 mmol) was added in one portion and the reaction stirred 2 hours. NaOH (1.13 g, 28.0 mmol) in water (3.1 mL) was then added dropwise over 9 min, causing precipitation. Filtration with a glass frit removed unreacted starting material and the filtrate was mixed with ammonium chloride (3.0 g). The resulting solution was concentrated by evaporation with a stream of nitrogen and the white precipitate was collected, washed with water and acetone, and dried to give a white solid (0.35 g, 12%). MP = 203 °C (dec.) ^{1}H NMR (600 MHz d6-DMSO) δ_H 7.74 (2H, d, *J*=8.3, H_{tosAr}), 7.43 (2H, d, *J*=8.3, H_{tosAr}), 5.75 (14H, br.s, $OH_{2,3}$), 4.83 (5H, m, H_1), 4.76 (2H, s, H_1), 4.61-4.39 (6H, m, OH_6), 4.32-4.15 (2H, m, H_{6tos}), 3.70-3.20 (>45H, m, $H_{6,5,4,3,2}$ inc. HOD), 2.42 (3H, s, Me_{tos}). ^{13}C NMR (150 MHz d6-DMSO) δ_C 144.9, 132.6, 129.9, 127.6, 101.9 (m), 81.4 (m), 73.1, 72.0 (m), 59.9 (m), 21.1.

*Mono(6-O-*p*-toluenesulfonyl) permethylated β-cyclodextrin (**11**)*

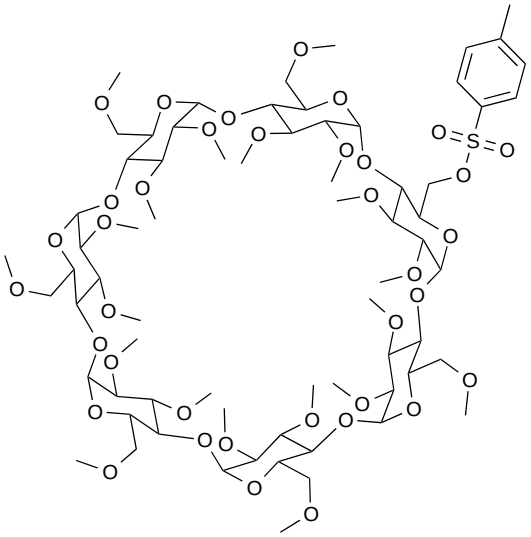

Prepared using a literature procedure.[210] Compound **10** (250 mg, 0.19 mmol) was dissolved in dry DMF and cooled to 0 °C. NaH (60% dispersion in mineral oil, 465 mg) was added carefully in portions and the reaction was stirred under argon at 0 °C for 1 hr and then at RT for 1 hr. The flask was again cooled to 0 °C and iodomethane (1.4 mL, 23.3 mmol) was added dropwise. The reaction was stirred for another hour, before being allowed to warm to RT, and stirred overnight.

The mixture was cooled again, and MeOH (2.5 mL) was added drop wise to quench excess NaH. The reaction mixture was poured into ice cold water and extracted with chloroform (3×50 mL). The organic layer was washed with 3% sodium thiosulfate solution (50 mL) and water (50 mL) before drying over $MgSO_4$ and removing the solvent. A yellowish oil was obtained containing the product and residual DMF and mineral oil. The material was purified by column chromatography with EtOAc containing 0.1% MeOH, which removed impurities and the mineral oil, however some DMF remained even after extensive washing (mass yield 871 mg, 70%, NMR of product suggested 44% yield). ^{1}H NMR (600 MHz $CDCl_3$) δ_H7.80 (2H, d, *J*=8.0, H_{tosAr}), 7.43 (2H, d, *J*=8.0, H_{tosAr}), 5.23-5.10 (7H, m, H_1), 5.06 (<2H, m, residual OH), 4.49-4.19 (2H, m, H_{6tos}), 4.00-3.30 (>100H, m, $H_{6,5,4,3,2}$, OMe, inc. MeOH), 2.50 (3H, s, Me_{tos}). ^{13}C NMR (150 MHz $CDCl_3$) δ_C 144.9, 133.2,

129.9, 127.8, 98.9 (m), 81.7 (m), 80.2 (m), 79.3, 70.9 (m), 61.5 (m), 58.9-58.5, 21.6.

*Mono(6-O-propargyl) permethylated β-cyclodextrin (**12**)*

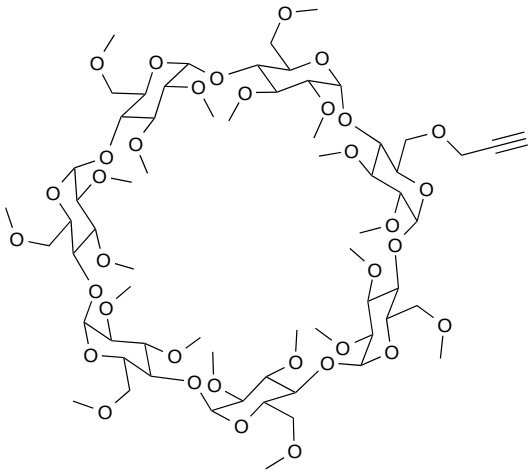

Prepared using a literature procedure.[210] NaH (60% dispersion in mineral oil, 443 mg) was added to dry DMF (10 mL) and propargyl alcohol (0.81 mL, 13.9 mmol) was added, before stirring at RT under nitrogen for 4 hrs. The reaction was cooled to 0 °C and cyclodextrin **11** was added in minimal DMF (870 mg, approximated to be 0.34 mmol). The reaction was allowed to warm to RT and stirred overnight at 50 °C, then 12 mL of water was added to quench the reaction. The solvents were removed under high-vacuum and the residue was dissolved in chloroform (50 mL). This was washed with water (3×100 mL) and the organic layer was dried over $MgSO_4$. Removal of solvents under reduced pressure to give an oily solid that was washed with hexane to remove the excess mineral oil. Column chromatography in EtOAc with 2.5% MeOH gave an off-white solid (370 mg, 75%). MP = 103 °C. ^{1}H NMR (600 MHz $CDCl_3$) δ_H 5.10 (7H, br s., H_1), 4.20 (2H, ABX, *J*=25, 15.7, 2.0, CH_2C≡CH), 3.89 (1H, dd, *J*=10.6, 3.1, H_5), 3.85-3.15 (101H, m), 2.43 (1H, t, *J*=2.0, C≡*CH*). ^{13}C NMR (150 MHz $CDCl_3$) δ_C 99.1 (m), 81.8 (m), 80.4 (m), 74.7, 71.0 (m), 68.9, 61.6 (m), 59.1, 58.6 (m). MS (ESI+) *m/z* 1451.71, 1475.70 ($[M]^+$ $C_{65}H_{112}O_{35}$ calc. 1452.6984, $[M+Na]^+$ calc. 1475.6876).

*Lipoic acid-triethyleneglycol-β-cyclodextrin (**CD**)*

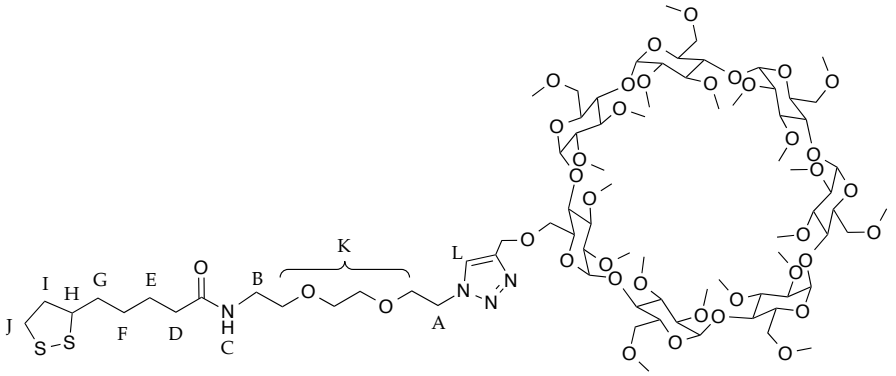

Compound **8** (12.3 mg, 0.034 mmol) was mixed with Cu on an activated carbon support (25 mg).[216] Monopropargyl permethyl-β-cyclodextrin **12** (50 mg, 0.034 mmol) was dissolved in 1 mL of dioxane and added followed by triethylamine (0.04 mmol, 5 μL). The reaction was heated at 70 °C, with stirring, for 3 days. The product was purified over a silica plug, and solvents removed to give a thick yellow oil (60 mg, 97%). ^{1}H NMR (600 MHz $CDCl_3$) δ_H 7.69 (1H, s, H_L), 6.03 (1H, br.s, H_C), 5.10 (7H, m, H1), 4.40 (2H, m, OCH_2C=C), 3.90-3.15 (116H, m, CD ring), 3.11 (2H, m, H_J), 2.45 (1H, m, H_I), 2.19 (2H, m, H_D), 1.91 (1H, m, H_I), 1.69 (4H, m, $H_{E,G}$), 1.47 (2H, m, H_F). ^{13}C NMR (150 MHz $CDCl_3$) δ_C 125.1 (triazole), 99.1, 82.2, 81.8, 80.4, 71.5, 71.0, 61.6, 61.5, 59.1, 58.7, 56.6, 50.7, 40.4, 39.2, 38.6, 34.8, 32.3, 29.8, 29.1, 26.5, 25.5, 23.6, 22.8. HRMS (ESI+) *m/z* 1815.8510 ($[M+H]^+$ $C_{79}H_{139}N_4O_{38}S_2$ calc. 1815.8509).

8.3.5 *Dopamine system*

*4-((3,4-dihydroxyphenylethyl)amino)-4-oxobutanoic acid (**13**)*

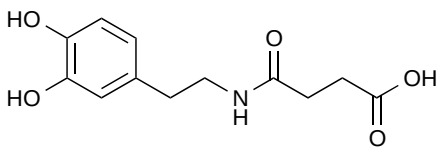

Procedure adapted from Bonina *et al.*[276] Dopamine hydrochloride (500 mg, 2.6 mmol) was dissolved in pyridine (25 mL) before succinic anhydride

(395 mg, 4.0 mmol) was added and the reaction was stirred at RT, under nitrogen overnight.

The solvent was removed under reduced pressure at 50 °C, then the residue was partitioned between acidified water and EtOAc. The organic layer was dried over $MgSO_4$ and the solvent was removed to give a white oily material (0.417 g, 63%). ^{1}H NMR (600 MHz CD_3CN) δ_H 6.72 (1H, d, J=7.9, Ar_5), 6.67 (1H, s, Ar_2), 6.55 (1H, dd, J=8.0, 2.0, Ar_6), 3.32 (2H, q, J=6.8, CH_2NH), 2.60 (2H, t, J=7.2, CH_2COOH), 2.51 (2H, t, J=7.2, CH_2CONH), 2.39 (2H, t, J=6.8, CH_2Ar). ^{13}C NMR (150 MHz CD_3CN) δ_C 174.2, 173,6, 145.3, 143.8, 132.4, 121.4, 116.7, 116.1, 41.8, 35.4, 30.9, 29.9.

*LA-PEG-Dopamine (**14**)*

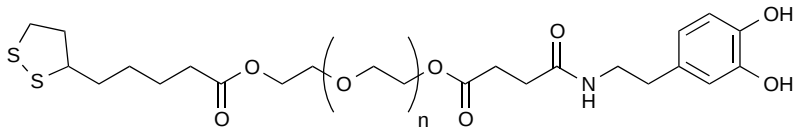

Dopamine succinamide (**13**) (50 mg, 0.20 mmol) and LA-PEG-OH (**5**) (124 mg, 0.2 mmol) were dissolved in MeCN (8 mL) and stirred at 0 °C under an Ar atmosphere. DCC (41 mg, 0.2 mmol) was dissolved in MeCN (2 mL) was added and the reaction was stirred at 0 °C for 45 minutes, then overnight at RT. The cloudy reaction mixture was filtered over celite to give a pale yellow filtrate which was dried under reduced pressure. At this point both the filtrate and the celite started to discolour to a dark red/brown colour. The residue was examined by NMR and MS, but both were inconclusive. ^{1}H and ^{13}C NMR showed a near 1:1 mixture of **5** and **13**, with some changes to the integrals, but the integral of H_A only increased from 2 to 2.7 protons, rather than the expected 4 protons. HMBC 2D NMR showed very little interaction between the terminal carboxylic acid carbon of **13** and the PEG protons H_A or H_K (Fig. 4.3). DOSY diffusion NMR appeared to show only one species, however as the starting molecular masses were similar and the error high, this was not proof alone.

8.3.6 *Cucurbituril system*

*Glycoluril hexamer (***G6***)*

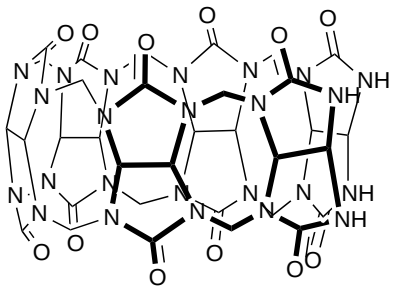

Prepared with an adapted literature procedure.[190] Glycoluril (1.00 g, 7.03 mmol), paraformaldehyde (356 mg, 11.75 mmol) and *p*-xylenediamine (pxda) (96 mg, 0.70 mmol) were added to a 5 mL flask with a stirrer bar, and stoppered with a fresh septum. The flask was shaken by hand for 2 min, before conc. HCl (37%, 1.41 mL, 5M with respect to glycoluril) was injected quickly, before a further 30 s of vigorous shaking.

The vessel was tightly sealed with the septum and heated at 58 °C for 5 days to give a cloudy yellow mixture. The mixture was cooled and centrifuged at 4000 rpm for 10 minutes to give a white precipitate and yellow supernatant. The white precipitate was reserved, and the yellow liquid was mixed with water washings from the flask before centrifuging again to give more white precipitate. The precipitates were collected and dried under vacuum.

50 mL of water was added to the remaining solid and the slurry was sonicated for 10 minutes before cooling to RT. The suspension was centrifuged and the supernatant was decanted. 5 M NaOH solution was added to the supernatant to cause a yellow precipitate to form in the solution, before the mixture was sonicated for 1 hour. After cooling to room temperature the precipitate was collected by centrifugation and washed with 0.1 M NaOH in MeOH (20 mL) and MeOH (20 mL) before drying under vacuum to give a off white solid (281 mg, 24%). MP $>$ 300 °C (dec.). ^{1}H NMR (600 MHz D_2O with added pxda) δ_H 5.84 (2H, d, *J*=15.4, H_{eq}), 5.70 (4H, d, *J*=15.4, H_{eq}), 5.65-5.60 (6H, m, H_{eq}), 5.57-5.50 (6H, m, H_{in}), 5.41 (2H, d, *J*=9.0, H_{in}), 5.37 (2H, d, *J*=9.0, H_{in}), 4.38 (2H, d, *J*=15.4, H_{ex}), 4.21 (4H, d, *J*=15.4, H_{ex}), 4.11

(4H, d, *J*=15.4, H_{ex}). MS (ESI+) *m/z* 638.2995 ([M+**BisIm**]$^{2+}$ $C_{52}H_{68}N_{28}O_{12}$ calc. 638.2780).

*3,3′-(octane-1,8-diyl)bis(1-ethyl-imidazolium) bromide (***BisIm***)*

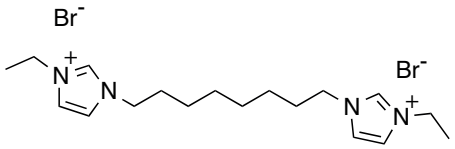

Based on a procedure from Zhao *et al.*[193] 1-ethylimidazole (5.5 mL, 50 mmol) and 1,8-dibromooctane (5.4 g, 20 mmol) were dissolved in toluene (50 mL) and heated at reflux for 18 hrs. The solvent was decanted and the remaining orange oil was triturated with ether (3×50 mL) and dried in a vacuum oven to give an off white, waxy solid (8.5 g, quantitative yield). MP = 70 °C. ^{1}H NMR (400 MHz D_2O) δ_H 8.72 (<2H, br.s, NC*H*$_2$N), 7.44 (2H, d, *J*=2.0, NC*H*$_2$CH$_2$N), 7.41 (2H, d, *J*=2.0, NCH$_2$C*H*$_2$N), 4.17 (4H, q, *J*=7.5, NC*H*$_2$CH$_3$), 4.12 (4H, t, *J*=7.3, NC*H*$_2$CH$_2$), 1.80 (4H, m, *J*=7.0, NCH$_2$C*H*$_2$), 1.44 (6H, t, *J*=7.3, NCH$_2$C*H*$_3$), 1.27-1.20 (8H, m, C_4H_8 core). MS (ESI+) *m/z* 383.1965 ([M]$^+$$C_{18}H_{32}N_4Br$ calc. 383.1805).

*Furan modified cucurbit[6]urils (***fCB[6]a** *&* **fCB[6]b***)*

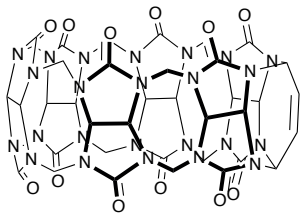

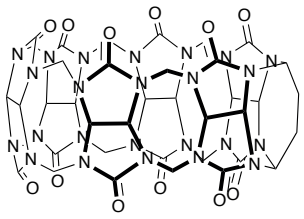

Gycoluril hexamer **G6** (25 mg, 26 μmol) and **BisIm** (12 mg, 26 μmol) were dissolved in either 10% HCl solution or glacial acetic acid (5 mL). 2,5-Dimethoxy-2,5-dihydrofuran (3.5 μL, 29 μmol) or 2,5-dimethoxytetrahydrofuran (4.0 μL, 29 μmol) were added and the reaction stirred at RT. After 60 hrs the yellow solutions were mixed with MeOH to give an orange precipitate, which was washed with copious MeOH. This highly insoluble material proved very difficult to characterise, but preliminary MS suggested that the bulk of the material was unreacted starting material. Representative MS

(ESI+) *m/z* 517.2601, 638.2995, 995.3259 ([**BisIm**+**G6**]$^{2+}$ $C_{52}H_{68}N_{28}O_{12}$; calc. 638.2780, [**G6**+Na]$^{+}$ calc. 995.2837, [**CB[6]**]$^{+}$ $C_{36}H_{36}N_{24}O_{12}$ calc. 996.2945).

*Purification of cucurbit[7]uril (***CB[7]***)*

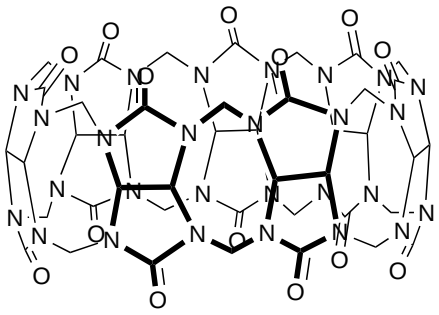

CB[5]/CB[7] solution in dilute HCl (1L) was prepared with the method described in Day *et al.*[184] and Jiao *et al.*[213] The liquid was stirred in a large conical flask at room temperature, and EtOH was added gradually until the mixture turned cloudy. Stirring was continued for an hour, and then halted to allow precipitation for one hour. The precipitate was removed by gravity filtration and collected and dried in a vacuum oven. The process was repeated a further 9 times. Each fraction was characterised by NMR once dry to assess purity. Fraction 1 contained mainly **CB[5]**, fractions 2-4 contained a mix of **CB[5]** and **CB[7]** in varying proportion, and fraction 5 onwards contained pure **CB[7]**. In total, ca. 3 g of pure material were isolated. MP > 300 °C (dec.). ^{1}H NMR (600 MHz D_2O/DCl) δ_H 5.73 (14H, d, *J*=15.3, H_{in}), 5.47 (14H, s, H_{eq}), 4.17 (14H, d, *J*=15.3, H_{ex}). ^{13}C NMR (150 MHz D_2O) δ_C 157.1, 69.8, 50.7. MS (ESI+) *m/z* 733.53 ([M+**BisIm**]$^{2+}$ $C_{60}H_{74}N_{32}O_{14}$ calc. 733.3026).

*Monohydroxy cucurbit[7]uril (***CB[7]monOH***)*

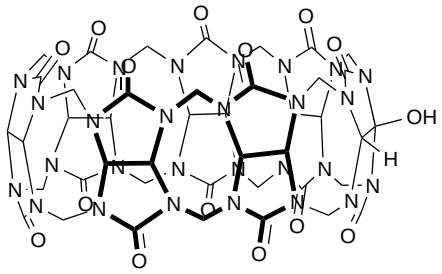

CB[7] (581 mg, 0.5 mmol) and **BisIm** (232 mg, 0.5 mmol) were dissolved in water (50 mL) and heated to 85 °C. Ammonium persulfate (114 mg, 0.5 mmol) was added and the reaction stirred at constant temperature over night.

The reaction mixture was cooled and reduced to 2 mL under reduced pressure at 50 °C. This residue was loaded onto a CHP20P MCI GEL column (bed volume 100 mL) and eluted with water. A 50 mL forecut was collected and then 10 mL fractions. The fractions were assessed for purity by ESI-MS. The column was regenerated for further use by washing with 100 mL 5% HCl and 200 mL water, then 100 mL 5% NaOH and water until neutral.

The collected fractions were dried to give 287 mg of pure **CB[7]** for recycling and 61 mg of **BisIm** $\subset$ **CB[7]monOH**. (7.5%)

71 mg of this material was synthesised and mixed with NH_4PF_6 (45 mg) and sonicated in 40 mL DCM then heated at reflux for 24 hrs. The solid was precipitated by centrifugation and washed with MeOH, before refluxing with more NH_4PF_6 (45 mg) for a further 72 hrs. This procedure was repeated once more to give pure (by MS) **CB[7] monOH** (22 mg, 45%). MP > 300 °C (dec.). ^{1}H NMR (400 MHz D_2O) δ_H 5.85-5.65 (2H + 10H, m, H_{ex}), 5.55-5.35 (14H, m, $H_{ex,eq}$), 5.22 (1H, s, CH_{eq}COH), 4.45 (2H, d, J=15.8, H_{ex} nr. OH), 4.20-4.13 (12H, m, H_{ex}). δ_C 157.1, 71.9, 53.2, 47.2. MS (ESI+) m/z 741.53, ([M+**BisIm**]$^{2+}$ $C_{60}H_{74}N_{32}O_{15}$ calc. 741.3000).

*Mono-O-propargyl cucurbit[7]uril (***fCB[7]***)*

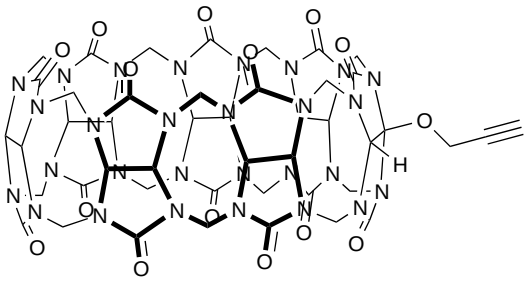

CB[7]monOH (10 mg, 8 μmol) and NaH (60% dispersion in mineral oil, 10 mg) were stirred under nitrogen in 1.5 mL of anhydrous DMSO. This slurry was stirred at RT for 15 mins before cooling to 0 °C. Propargyl bromide (80% in toluene, 0.3 mL, 2.7 mmol) was added and the reaction was stirred at room temperature for 18 hrs. The yellow/brown mixture was diluted with ether (50 mL), and filtered to remove the solid precipitate. This precipitate was then washed with MeOH (100 mL) before drying under vacuum to yield a yellow solid (9 mg, 92%, but NMR only demonstrated 50% propargylation). ^{1}H NMR (600 MHz D_2O) δ_H 5.85-5.65 (2H + 10H, m, H_{ex}), 5.59-5.34 (14H, m, $H_{ex,eq}$), 5.22 (< 1H, s, CH_{eq}COH), 4.81 (∼1H, m, *CH2*≡CH), 4.48-4.37 (2H, m, H_{ex} nr. OH), 4.27-4.10 (12H, m, H_{ex}), 2.62 (∼0.5H, s, C≡*CH*). MS (ESI+) *m/z* 761.47 ([M+**BisIm**]$^{2+}$ $C_{63}H_{76}N_{32}O_{15}$ calc. 760.3078).

8.3.7 *Naphthalene system*

*2-(prop-2-ynyloxy)naphthalene (**15**)*

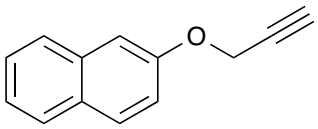

In a round bottom flask, 2-naphthol (144 mg, 1.0 mmol) was dissolved in 10 mL of dry acetone with stirring, and anhydrous K_2CO_3 (0.28 mg, 2.0 mmol) was added. After 30 mins, propargyl bromide (80% in toluene, 95 μL, 1.0 mmol) was added and the reaction was brought to reflux over night. The mixture was cooled and filtered, and the solvents of the filtrate removed. The residue was taken up in DCM and washed with water (30 mL $\times$ 2), then the organic layer was collected, dried and solvent was removed under reduced pressure to yield a yellow/orange, low melting point solid (108 mg, 60%). MP = 59 °C. ^{1}H NMR (600 MHz $CDCl_3$) δ_H 7.80-7.75 (3H, m, H_{Ar}), 7.47 (1H, d, *J*=7.2, H_{Ar}), 7.37 (1H, d, *J*=7.2, H_{Ar}), 7.25 (1H, d, *J*=2.6, H_{Ar}), 7.20 (1H, dd, *J*=8.9, 2.6, H_{Ar}), 4.83 (2H, d, *J*=2.3, O*CH*2C), 2.57 (1H, t, *J*=2.3, C≡*CH*). ^{13}C NMR (150 MHz $CDCl_3$) δ_C 155.6, 134.4, 129.7, 129.4, 127.8, 127.1, 126.6, 124.2, 118.9, 107.5, 56.0. MS (ESI+) 181.07, 153.07, 115.05, HRMS (ESI+) 182.0725 ([M]$^+$ $C_{13}H_{10}O$ calc. 182.0726).

*Lipoic acid-triethyleneglycol-naphthalene (**16**)*

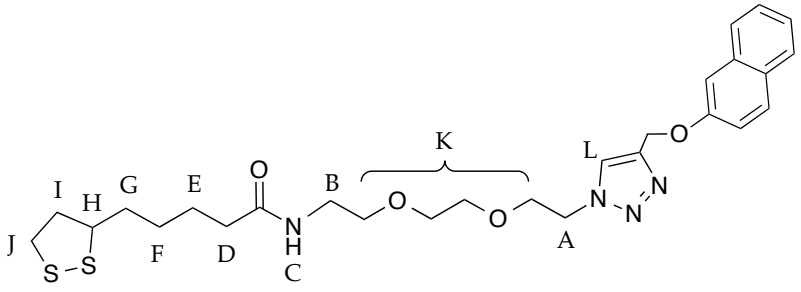

Compound **8** (50 mg, 0.14 mmol) was mixed with Cu on an activated carbon support (50 mg).[216] Monopropargyl naphthalene **15** (25 mg, 0.14 mmol) was dissolved in 2 mL of dioxane and added followed by triethylamine (0.15 mmol, 21 μL). The reaction was heated at 70 °C, with stirring, for 3

days. The product was purified over a silica plug, and solvents removed to give a thick orange oil (74 mg, 99%).^{1}H NMR (600 MHz $CDCl_3$) δ_H 7.83 (1H, s, H_L), 7.80-7.73 (3H, m, H_{Ar}), 7.45 (1H, m, H_{Ar}), 7.36 (1H, m, H_{Ar}), 7.28 (1H, m, H_{Ar}), 7.19 (1H, dd, *J*=9.2, 2.6, H_{Ar}), 5.90 (1H, br.s, H_C), 5.36 (2H, s, OC*H*2C), 4.57 (2H, t, *J*=4.9, H_A), 3.91 (2H, t, *J*=4.9, H_K), 3.60-3.37 (9H, m, $H_{K,H,B}$), 3.20-3.05 (2H, m, H_J), 2.43 (1H, m, H_I), 2.16 (2H, t, *J*=7.5, H_D), 1.87 (1H, m, H_I), 1.65 (4H, m, $H_{E,G}$), 1.42 (2H, m, H_F). ^{13}C NMR (125 MHz $CDCl_3$) δ_C 173.0, 156.2, 144.1, 134.5, 129.6, 129.2, 127.7, 127.0, 126.6, 124.0, 118.8, 107.4, 70.5, 70.2, 70.0, 69.4, 62.2, 56.5, 40.3, 39.2, 38.5, 36.4, 34.7, 28.9, 25.4. HRMS (ESI+) 545.2275, 567.2443 ($[M+H]^+$ $C_{27}H_{37}N_4O_4S_2$ 545.2256, $[M+Na]^+$ 567.2070).

*Lipoic acid-polyethyleneglycol-naphthalene (**18**)*

Compound **3** (86 mg, 0.14 mmol) was mixed with Cu on an activated carbon support (50 mg).[216] Monopropargyl naphthalene **15** (25 mg, 0.14 mmol) was dissolved in 2 mL of dioxane and added followed by triethylamine (0.15 mmol, 21 μL). The reaction was heated at 70 °C, with stirring, for 3 days. The product was purified over a silica plug, and solvents removed to give an orange oily solid (90 mg, 79%).^{1}H NMR (600 MHz $CDCl_3$) δ_H 7.88 (1H, br.s, H_L), 7.76 (3H, m, H_{Ar}), 7.45 (1H, dd, *J*=16.0, 7.8, H_{Ar}), 7.35 (1H, dd, *J*=16.0, 7.8, H_{Ar}), 7.27 (1H, m, H_{Ar}), 7.19 (1H, m, H_{Ar}), 6.23 (1H, br.s, H_C), 5.34 (2H, s, OC*H*2C), 4.57 (2H, t, *J*=4.9, H_A), 3.88 (2H, t, *J*=4.9, H_K), 3.68-3.50 (∼25H, m, $H_{K,H}$), 3.44 (2H, m, H_B), 3.20-3.05 (2H, m, H_J), 2.45 (1H, m, H_I), 2.18 (2H, t, *J*=6.5, H_D), 1.90 (1H, m, H_I), 1.68 (4H, m, $H_{E,G}$), 1.45 (2H, m, H_F). ^{13}C NMR (150 MHz $CDCl_3$) δ_C 172.9, 156.3, 144.0, 134.6, 129.7, 127.7, 127.0, 126.6, 124.0, 119.0, 107.4, 75.8, 70.7-69.6, 62.2, 56.6, 50.5, 40.3, 39.3, 38.6, 36.5, 34.8, 29.0, 25.5.

8.4 GELATOR SYNTHESIS

*1,2:5,6-di-O-cyclohexylidene-D-mannitol (**19**)*

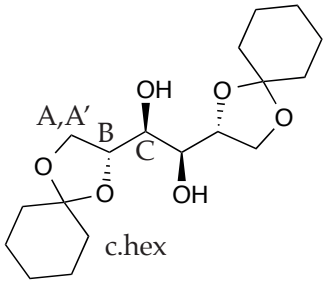

LMWO **19** was synthesised using the procedure described in Vidyasagar *et al.*,[267] however the product was used crude, without further purification. D-mannitol (8.0 g, 44 mmol) was suspended in dry DMF (200 mL), then 1,1-dimethylcyclohexane (12.0 g, 88 mmol) and *p*-tosylsulfonic acid (750 mg, 3.9 mmol) were added with stirring. The mixture was heated to 60 °C for 1 hour then cooled to RT, before triethylamine (4 mL) was added. The solvents were removed under reduced pressure, and the residue extracted with EtOAc (75 mL), then washed with water (5 × 75 mL). The organic layer was dried over $MgSO_4$ and the solvent removed to yield a white solid (13.62 g, 91%). MP = 81 °C. ^{1}H NMR (600 MHz $CDCl_3$) δ_H 4.19 (2H, dd, *J*=14.0, 6.4, H_A), 4.11 (2H, m, H_B), 3.96 (2H, dd, *J*=8.6, 5.6, $H_{A'}$), 3.74 (2H d, *J*=6.8, H_C), 1.65-1.50 (20H, m, c.hex).

8.5 NANOPARTICLE SYNTHESES

8.5.1 *Quantum Dots*

CdSe@ZnS Nanoparticles

CdSe@ZnS quantum dot synthesis adapted from literature.[50, 214, 277]

To form the QD cores, cadmium oxide (51 mg, 0.4 mmol), trioctylphosphine oxide (3.7 g, 9.6 mmol), hexadecylamine (1.93 g, 8 mmol) and 1-dodecylphosphonic acid (0.22 g, 0.88 mmol) were weighed into a 250 mL,

3-neck flask fitted with a condenser. This was evacuated and flushed with nitrogen five times, before heating to 320 °C and stirring for 1 hr.

Trioctylphosphine (TOP) containing selenium powder (8 mL, 0.5 M soln.), that had been previously freeze-pump-thaw degassed, was injected rapidly with the temperature lowered to 270 °C, and the reaction stirred for a timed period, depending on the size of QD required. After this time had elapsed the flask was cooled rapidly to 100 °C in boiling water. The times used were 30 s, 5 min and 10 min to create blue, green and red QDs respectively, and care was taken to ensure that the temperature of the reaction did not rise significantly above 270 °C during the growth phase.

After cooling to room temperature, chloroform (10 mL) was added and the QDs were precipitated with EtOH, and centrifuged at 4000 rpm. The supernatant was removed and the QDs were resuspended in hexane (10 mL).

To create the CdSe@ZnS core shell particles, the cores in hexane were mixed with zinc diethyldithiocarbamate (0.5 g, 1.4 mmol), oleylamine (3 mL, 9.12 mmol), octadecene (10 mL) and TOP (3 mL, 6.73 mmol). The mixture was heated slowly (around 3 °C/min) under partial vacuum to 70 °C, to remove the hexane, and then on to 120 °C under a flow of nitrogen. After 2 hours, the reaction was cooled, and the QDs were precipitated with EtOH and isolated with centrifugation at 4000 rpm. The QD slurry was dried in air, and suspended in minimal hexane, before centrifuging again to remove any insoluble impurities. These solutions were stored at 4 °C for further use.

InP@ZnS Nanoparticles

InP cores were synthesised with the method of Xu *et al.* with assistance of Dr Joseph Bear.[278]

Stearic acid (28.5 mg, 0.1 mmol), zinc undecylenate (86 mg, 0.2 mmol), indium(III) chloride (22 mg, 0.1 mmol), and hexadecylamine (48 g, 0.2 mmol) were added to a nitrogen-purged Schlenk flask. To this, 1-octadecene (2 mL) was added, and the mixture vacuum/back filled with nitrogen three times before heating to 270 °C. On reaching 270 °C, a solution of tris(trimethylsilyl)-phosphine (1 mL, 0.1 M) in 1-octadecene was rapidly injected, and the solution heated at 240 °C for 20 min to allow the QDs to grow. The flask was then quenched in hot water to cool to room temperature, before addition

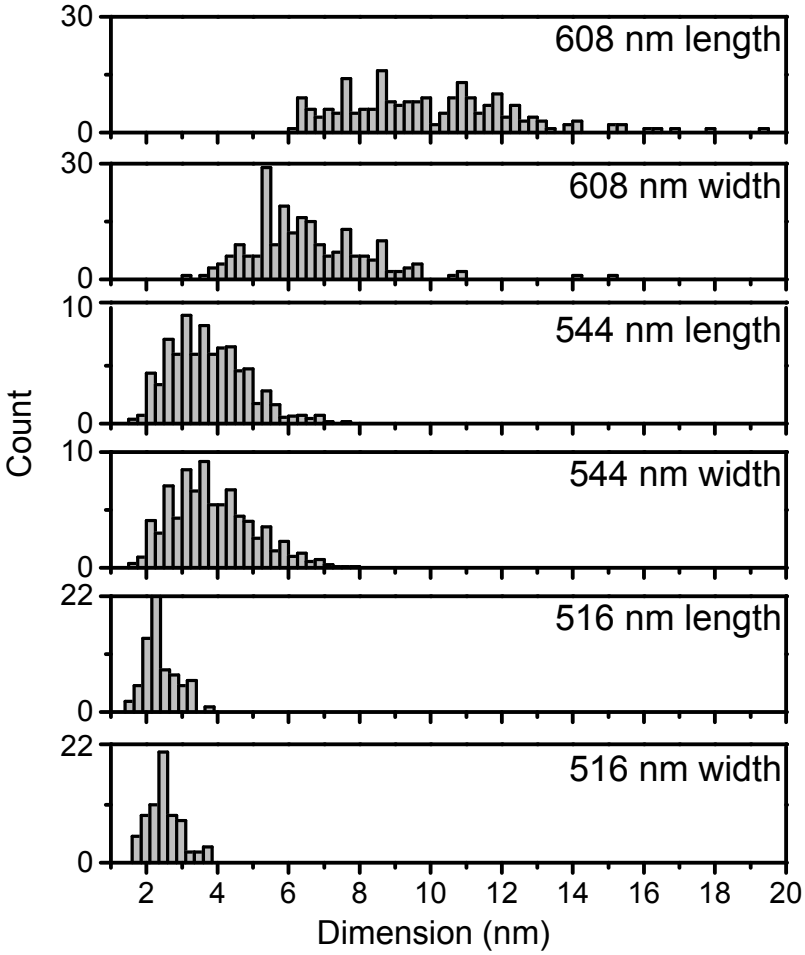

Figure 8.1: *Histograms of measured particle sizes by TEM for the em. = 516, 544 and 608 nm CdSe@ZnS samples in hexane. Particles were fitted with ellipses in ImageJ, and so two dimensions are given for each sample. Values were binned in 0.25 nm increments. n = 70, 924 and 214 respectively.*

of toluene (4 mL). InP QDs were precipitated with ethanol (80 mL) and isolated with centifugation (5 min at 4000 rpm). The QDs were washed twice with ethanol (2 × 60 mL) to remove any unbound surfactants, and dispersed in n-hexane (10 mL).

Shelling with ZnS was performed in an identical method to the CdSe@ZnS particles above.

Ligand exchange

To create the QD-ligand conjugates, a protocol based on Palui *et al.* was used.[207] 30 μL of an as-synthesised quantum dot solution was added to 710 μL *n*-hexane in a glass vial. Methanolic tetramethylammonium hydroxide solution (20 mM, 100 μL) and 250 μL of 100 mM methanolic ligand

solution were added to form a biphasic mixture. A stirrer bar was added and the atmosphere switched to nitrogen, before the vial was capped and stirred under 5 × 18 W 365 nm UV-bulbs (Phillips TL-D). The progress of the reaction was monitored by observing the fluorescence in the methanolic layer, and once the transfer was complete (typically after 3 hrs) the QDs were mixed with 1 mL 10:1 ethanol/chloroform and 9 mL hexane, to precipitate, before separation and washing *via* centrifugation three times (4500 rpm, 5 mins). The precipitated QDs were resuspended in 1 mL MeOH and stored at 4 °C for further use.

8.5.2 *Gold Nanoparticles*

Turkevich AuNP synthesis

Chloroauric acid (24 mg, 0.06 mmol) was dissolved in 50 mL of water and brought to reflux. Trisodium citrate (50 mg, 0.19 mmol) in 5 mL water was added and reflux continued for 1 hr. The colour changed to dark red, indicating the formation of AuNPs.[279]

Brust AuNP synthesis

A solution of chloroauric acid (30mM, 6 mL) was mixed with a solution of TOAB in toluene (50mM, 16 mL) and shaken to effect phase transfer of the gold salt. Dodecane thiol (40 uL, 0.17 mmol) was added with further stirring, then freshly prepared $NaBH_4$ solution in water (0.40 M, 5 mL) was added slowly with vigorous stirring. The solution darkened and was stirred for a further 3 hrs. The organic layer was separated, dried and then concentrated under reduced pressure to a volume of 1-2 ml. Ethanol was added (50 mL) and the mixture stored at -18 °C for 12 hours to precipitate out a crude product. This product was filtered off, redissolved in 2 mL toluene the process repeated. This yielded red-brown crystalline material for further characterisation.[151]

Xie AuNS synthesis

A stock solution of HEPES buffer in water was prepared (100 mM) and the pH adjusted to 7.4 with 1M NaOH. 2 mL of this solution was mixed with 3 mL water and 50 uL of chloroauric acid solution (20 mM). This mixture was swirled then left to stand at RT. After $\sim$ 30 min. a blue colour developed, indicating the formation of the AuNS solution.[155]

Production of AuNPs with ketones

Ketone derived AuNPs were synthesised as described in Section 3.2.[91] An 6 mM aqueous chloroauric acid ($HAuCl_4$) stock solution (50 mL) was made from anhydrous $HAuCl_4$ (102 mg, 0.3 mmol). The colloidal suspensions were synthesised by mixing a ketone: cyclohexanone (0.5 mL, 4.8 mmol); cyclopentanone (0.5 mL, 5.7 mmol); cycloheptanone (0.5 mL, 4.2 mmol); 1,4-cyclohexanedione (0.5 g, 4.4 mmol); 1,3-cyclohexanedione (0.5 g, 4.4 mmol); 3-hexanone (0.5 mL, 4.1 mmol); acetone (0.5 mL, 6.8 mmol); acetylacetone (0.5 mL, 4.8 mmol) or 2,5-hexanediketone (0.5 mL, 4.3 mmol) with water (9.5 mL) in clean glass vials. Where a biphasic suspension was formed, the mixture was emulsified with vigorous shaking for a minute. $HAuCl_4$ stock solution (0.44 mL, 2.6 μmol) was then rapidly injected and the vial shaken briefly by hand. The reactions were left to stand at room temperature and the colour changes were observed, with a developing red or purple/orange colour indicated the formation of gold colloid. This was used as produced for further characterisation.

Production of AuNPs in-situ *with sputter coating*

A portion of 4 wt% gel containing no nanoparticles, approximately 5 mm thick was placed on a metal stub in the chamber of a Quorum Q150R ES sputter coater with gold target. A 20 mA current was set, and the sample was sputtered under Argon atmosphere for 60 s. Initially the colouration of the sample was highly localised in three areas, but after 24 hours had dif-

fused throughout the material. The process was also repeated with a silver target, to obtain a grey/yellow gel 24 hours after sputtering.

8.5.3 *Other Metal and Metal Oxides (Ni, Fe3O4, CoO)*

Fe_3O_4 and CoO nanoparticles were synthesised by decomposition of the metal oleate in oleic acid and 1-octadecene (ODE). Ni nanoparticles were synthesised from decomposition of Ni(II)acac in oleylamine and trioctyl phosphine (TOP). All procedures are as described in Crick *et al.* [272].

8.5.4 *MWCNTs*

Pyrene modified MWCNTs were produced as described, by mixing MWCNTs with a oleyl-functionalised pyrene.[274].

BIBLIOGRAPHY

[1] Lehn, J.-M. Supramolecular chemistry—scope and perspectives molecules, supermolecules, and molecular devices (Nobel Lecture). *Angew. Chem. Int. Ed.* **27**, 89–112 (1988).

[2] Marshall, M. & Oxley, J. C. (eds.) *Aspects of Explosives Detection* (Elsevier B.V., Oxford, 2008).

[3] Hazarika, P. & Russell, D. A. Advances in Fingerprint Analysis. *Angew. Chem. Int. Ed.* **51**, 3524–3531 (2012).

[4] Smith, R. G., D'Souza, N. & Nicklin, S. A review of biosensors and biologically-inspired systems for explosives detection. *Analyst* **133**, 571–584 (2008).

[5] Pamula, V. K. Detection of Explosives. In *Handbook of Machine Olfaction*, 547–560 (Wiley-VCH Verlag GmbH & Co. KGaA, Weinheim, 2004).

[6] icasualties Casualty Count. URL `http://icasualties.org`. Accessed: Jun 2015.

[7] Cullum, H. E., McGavigan, C., Uttley, C. Z., Stroud, M. A. M. & Warren, D. C. A Second Survey of High Explosives Traces in Public Places. *J Forensic Sci* **49**, 1–7 (2004).

[8] Swedish Defence Research Agency. EMPHASIS. URL `http://www.foi.se/en/Customer--Partners/Projects/EMPHASIS/EMPHASIS/`. Accessed: Jun 2015.

[9] Burrows, E. P., Rosenblatt, D. H., Mitchell, W. R. & Parmer, D. L. Organic Explosives and Related Compounds: Environmental and Health Considerations. Tech. Rep., US Army Biomedical Research and Development Laboratory (1989). URL `http://www.dtic.mil/dtic/tr/fulltext/u2/a210554.pdf`.

[10] Ochsenbein, U., Zeh, M. & Berset, J.-D. Comparing solid phase extraction and direct injection for the analysis of ultra-trace levels of relevant explosives in lake water and tributaries using liquid chromatography–electrospray tandem mass spectrometry. *Chemosphere* **72**, 974–980 (2008).

[11] Allan, I. *et al.* Strategic monitoring for the European Water Framework Directive. *TrAC* **25**, 704–715 (2006).

[12] Douglas, T. A., Johnson, L., Walsh, M. & Collins, C. A time series investigation of the stability of nitramine and nitroaromatic explosives in surface water samples at ambient temperature. *Chemosphere* **76**, 1–8 (2009).

[13] Technical Fact Sheet - 2,4,6-trinitrotoluene (TNT). Tech. Rep., United States Environmental Protection Agency (2014). URL `http://www2.epa.gov/sites/production/files/2014-03/documents/ffrrofactsheet_contaminant_tnt_january2014_final.pdf`.

[14] Caygill, J. S., Davis, F. & Higson, S. P. J. Current trends in explosive detection techniques. *Talanta* **88**, 14–29 (2012).

[15] Harper, R. J., Almirall, J. R. & Furton, K. G. Identification of dominant odor chemicals emanating from explosives for use in developing optimal training aid combinations and mimics for canine detection. *Talanta* **67**, 313–327 (2005).

[16] Furton, K. G. & Myers, L. J. The scientific foundation and efficacy of the use of canines as chemical detectors for explosives. *Talanta* **54**, 487–500 (2001).

[17] Furton, K. G. & Heller, D. P. Advances in the Reliable Location of Forensic Specimens through Research and Consensus: Best Practice Guidelines for Dog and Orthogonal Instrumental Detectors. *Canadian J. Police and Security Services* **3**, 97 (2005).

[18] de la Rica, R. & Stevens, M. M. Plasmonic ELISA for the ultrasensitive detection of disease biomarkers with the naked eye. *Nat. Nanotechnol.* **7**, 821–824 (2012).

[19] Albert, K. J. *et al.* Cross-reactive chemical sensor arrays. *Chem. Rev.* **100**, 2595–2626 (2000).

[20] Bishop, C. M. Sparse Kernel Machines. In *Pattern recognition and machine learning*, 325–344 (Springer, New York, 2006).

[21] Peveler, W. J., Binions, R., Hailes, S. M. V. & Parkin, I. P. Detection of explosive markers using zeolite modified gas sensors. *J. Mater. Chem. A* **1**, 2613–2620 (2013).

[22] Rana, S. *et al.* A multichannel nanosensor for instantaneous readout of cancer drug mechanisms. *Nat. Nanotechnol.* **10**, 65–69 (2014).

[23] Kasera, S., Herrmann, L. O., Barrio, J. d., Baumberg, J. J. & Scherman, O. A. Quantitative multiplexing with nano-self-assemblies in SERS. *Sci Rep* **4**, 6785 (2014).

[24] Stewart, S., Ivy, M. A. & Anslyn, E. V. The use of principal component analysis and discriminant analysis in differential sensing routines. *Chem. Soc. Rev.* **43**, 70–84 (2014).

[25] Abdul-Karim, N., Blackman, C. S., Gill, P. P., Wingstedt, E. M. M. & Reif, B. A. P. Post-blast explosive residue – a review of formation and dispersion theories and experimental research. *RSC Adv.* **4**, 54354–54371 (2014).

[26] Reid Asbury, G., Klasmeier, J. & Hill Jr, H. H. Analysis of explosives using electrospray ionization/ion mobility spectrometry (ESI/IMS). *Talanta* **50**, 1291–1298 (2000).

[27] Eiceman, G. A. & Schmidt, H. Advances in Ion Mobility Spectrometry of Explosives. In Marshall, M. & Oxley, J. C. (eds.) *Aspects of Explosives Detection*, 171–202 (Elsevier, Oxford, 2009).

[28] Eiceman, G. A. & Stone, J. A. Peer Reviewed: Ion Mobility Spectrometers in National Defense. *Anal. Chem.* **76**, 390 A–397 A (2004).

[29] Andrew, T. L. & Swager, T. M. A Fluorescence Turn-On Mechanism to Detect High Explosives RDX and PETN. *J. Am. Chem. Soc.* **129**, 7254–7255 (2007).

[30] Fido Explosives Detectors Technical Overview. Tech. Rep., ICX Technologies (2011). URL `http://gs.flir.com/uploads/file/products/brochures/fidotechnicaloverview.pdf`.

[31] Rose, A., Zhu, Z., Madigan, C. F., Swager, T. M. & Bulović, V. Sensitivity gains in chemosensing by lasing action in organic polymers. *Nature* **434**, 876–879 (2005).

[32] Thomas III, S. W., Amara, J. P., Bjork, R. E. & Swager, T. M. Amplifying fluorescent polymer sensors for the explosives taggant 2,3-dimethyl-2,3-dinitrobutane (DMNB). *Chem. Commun.* 4572–4574 (2005).

[33] Germain, M. E. & Knapp, M. J. Optical explosives detection: from color changes to fluorescence turn-on. *Chem. Soc. Rev.* **38**, 2543–2555 (2009).

[34] Feng, H.-T., Wang, J.-H. & Zheng, Y.-S. CH_3–π Interaction of Explosives with Cavity of a TPE Macrocycle: The Key Cause for Highly Selective Detection of TNT. *ACS Appl. Mater. Interfaces* **6**, 20067–20074 (2014).

[35] Hou, X.-G. *et al.* A cationic iridium(iii) complex with aggregation-induced emission (AIE) properties for highly selective detection of explosives. *Chem. Commun.* **50**, 6031–6034 (2014).

[36] Venkatramaiah, N., Firmino, A. D. G., Almeida Paz, F. A. & Tomé, J. P. C. Fast detection of nitroaromatics using phosphonate pyrene motifs as dual chemosensors. *Chem. Commun.* **50**, 9683–9686 (2014).

[37] Xu, M. *et al.* Fluorescence Ratiometric Sensor for Trace Vapor Detection of Hydrogen Peroxide. *ACS Appl. Mater. Interfaces* **6**, 8708–8714 (2014).

[38] Jurcic, M. *et al.* The vapour phase detection of explosive markers and derivatives using two fluorescent metal–organic frameworks. *J. Mater. Chem. A* **3**, 6351–6359 (2015).

[39] Lan, A. *et al.* A Luminescent Microporous Metal–Organic Framework for the Fast and Reversible Detection of High Explosives. *Angew. Chem. Int. Ed.* **48**, 2334–2338 (2009).

[40] Banerjee, D., Hu, Z. & Li, J. Luminescent metal-organic frameworks as explosive sensors. *Dalton Trans.* **43**, 10668–10685 (2014).

[41] Hu, Z., Deibert, B. J. & Li, J. Luminescent metal-organic frameworks for chemical sensing and explosive detection. *Chem. Soc. Rev.* (2014).

[42] Wang, J. Electrochemical Sensing of Explosives. *Electroanalysis* **19**, 415–423 (2007).

[43] Wei, L. *et al.* Highly sensitive detection of trinitrotoluene in water by chemiresistive sensor based on noncovalently amino functionalized single-walled carbon nanotube. *Sens. Actuator B Chem.* **190**, 529–534 (2014).

[44] Evans, G. P., Buckley, D. J., Skipper, N. T. & Parkin, I. P. Single-walled carbon nanotube composite inks for printed gas sensors: enhanced detection of NO2, NH3, EtOH and acetone. *RSC Adv.* **4**, 51395–51403 (2014).

[45] Marín, S. & Merkoçi, A. Nanomaterials Based Electrochemical Sensing Applications for Safety and Security. *Electroanalysis* **24**, 459–469 (2012).

[46] Tiwari, J. N., Tiwari, R. N. & Kim, K. S. Zero-dimensional, one-dimensional, two-dimensional and three-dimensional nanostructured materials for advanced electrochemical energy devices. *Progress in Materials Science* **57**, 724–803 (2012).

[47] Burda, C., Chen, X., Narayanan, R. & El-Sayed, M. A. Chemistry and Properties of Nanocrystals of Different Shapes. *Chem. Rev.* **105**, 1025–1102 (2005).

[48] LaMer, V. K. & Dinegar, R. H. Theory, Production and Mechanism of Formation of Monodispersed Hydrosols. *J. Am. Chem. Soc.* **72**, 4847–4854 (1950).

[49] Uppal, M. A., Kafizas, A., Lim, T. H. & Parkin, I. P. The extended time evolution size decrease of gold nanoparticles formed by the Turkevich method. *New J. Chem.* **34**, 1401–1407 (2010).

[50] Bear, J. C. *et al.* Doping Group IIB Metal Ions into Quantum Dot Shells via the One-Pot Decomposition of Metal-Dithiocarbamates. *Adv. Opt. Mater.* **3**, 704–712 (2015).

[51] Morris-Cohen, A. J., Malicki, M., Peterson, M. D., Slavin, J. W. J. & Weiss, E. A. Chemical, Structural, and Quantitative Analysis of the Ligand Shells of Colloidal Quantum Dots. *Chem. Mater.* **25**, 1155–1165 (2013).

[52] Kamaly, N., Xiao, Z., Valencia, P. M., Radovic-Moreno, A. F. & Farokhzad, O. C. Targeted polymeric therapeutic nanoparticles: design, development and clinical translation. *Chem. Soc. Rev.* **41**, 2971–3010 (2012).

[53] Petryayeva, E., Algar, W. R. & Medintz, I. L. Quantum Dots in Bioanalysis: A Review of Applications Across Various Platforms for Fluorescence Spectroscopy and Imaging. *Applied Spectroscopy* **67**, 215–252 (2013).

[54] Green, M. The nature of quantum dot capping ligands. *J. Mater. Chem.* **20**, 5797–5809 (2010).

[55] Jenkins, T. F. & Walsh, M. E. Development of field screening methods for TNT, 2,4-DNT and RDX in soil. *Talanta* **39**, 419–428 (1992).

[56] Dasary, S. S. R. *et al.* Ultrasensitive and Highly Selective Detection of TNT From Environmental Sample Using Two-Photon Scattering Properties of Aminothiophenol-Modified Gold Nanoparticle. *IEEE Trans. Nanotechnology* **10**, 1083–1088 (2011).

[57] Chen, Y. *et al.* L-cysteine-capped CdTe QD-based sensor for simple and selective detection of trinitrotoluene. *Nanotechnology* **21**, 125502 (2010).

[58] Dasary, S. S. R. *et al.* Highly Sensitive and Selective Dynamic Light-Scattering Assay for TNT Detection Using p-ATP Attached Gold Nanoparticle. *ACS Appl. Mater. Interfaces* **2**, 3455–3460 (2010).

[59] Lin, D. *et al.* Ultrasensitive optical detection of trinitrotoluene by ethylenediamine-capped gold nanoparticles. *Anal. Chim. Acta* **744**, 92–98 (2012).

[60] Gao, D. *et al.* Resonance Energy Transfer-Amplifying Fluorescence Quenching at the Surface of Silica Nanoparticles toward Ultrasensitive Detection of TNT. *Anal. Chem.* **80**, 8545–8553 (2008).

[61] Wang, Y., La, A., Brückner, C. & Lei, Y. FRET- and PET-based sensing in a single material: expanding the dynamic range of an ultra-sensitive nitroaromatic explosives assay. *Chem. Commun.* **48**, 9903–9905 (2012).

[62] Lou, Z., Cui, Y., Yang, M. & Chen, J. The mechanism of 2,4,6-trinitrotoluene detection with amino acid-capped quantum dots: a density functional theory study. *RSC Adv.* **5**, 48406–48412 (2015).

[63] Stringer, R. C., Gangopadhyay, S. & Grant, S. A. Detection of Nitroaromatic Explosives Using a Fluorescent-Labeled Imprinted Polymer. *Anal. Chem.* **82**, 4015–4019 (2010).

[64] Li, J., Kendig, C. E. & Nesterov, E. E. Chemosensory Performance of Molecularly Imprinted Fluorescent Conjugated Polymer Materials. *J. Am. Chem. Soc.* **129**, 15911–15918 (2007).

[65] Zhu, W. *et al.* Hierarchically Imprinted Porous Films for Rapid and Selective Detection of Explosives. *Langmuir* **27**, 8451–8457 (2011).

[66] Riskin, M., Tel-Vered, R., Lioubashevski, O. & Willner, I. Ultrasensitive Surface Plasmon Resonance Detection of Trinitrotoluene by a Bis-aniline-Cross-Linked Au Nanoparticles Composite. *J. Am. Chem. Soc.* **131**, 7368–7378 (2009).

[67] Riskin, M., Tel-Vered, R. & Willner, I. Imprinted Au-Nanoparticle Composites for the Ultrasensitive Surface Plasmon Resonance Detection of Hexahydro-1,3,5-trinitro-1,3,5-triazine (RDX). *Adv. Mater.* **22**, 1387–1391 (2010).

[68] Anderson, G. P. *et al.* TNT Detection Using Multiplexed Liquid Array Displacement Immunoassays. *Anal. Chem.* **78**, 2279–2285 (2013).

[69] Kawaguchi, T. *et al.* Surface plasmon resonance immunosensor using Au nanoparticle for detection of TNT. *Sens. Actuator B Chem.* **133**, 467–472 (2008).

[70] Wilson, R., Spiller, D. G., Prior, I. A., Bhatt, R. & Hutchinson, A. Magnetic microspheres encoded with photoluminescent quantum dots for multiplexed detection. *J. Mater. Chem.* **17**, 4400–4406 (2007).

[71] Goldman, E. R. *et al.* A Hybrid Quantum Dot-Antibody Fragment Fluorescence Resonance Energy Transfer-Based TNT Sensor. *J. Am. Chem. Soc.* **127**, 6744–6751 (2005).

[72] Demirel, G. B., Daglar, B. & Bayindir, M. Extremely fast and highly selective detection of nitroaromatic explosive vapours using fluorescent polymer thin films. *Chem. Commun.* **49**, 6140–6142 (2013).

[73] Chaudhari, A. K., Nagarkar, S. S., Joarder, B. & Ghosh, S. K. A Continuous π-Stacked Starfish Array of Two-Dimensional Luminescent MOF for Detection of Nitro Explosives. *Cryst. Growth Des.* **13**, 3716–3721 (2013).

[74] Li, X., Zhang, Z. & Tao, L. A novel array of chemiluminescence sensors for sensitive, rapid and high-throughput detection of explosive triacetone triperoxide at the scene. *Biosens. Bioelectron.* **47**, 356–360 (2013).

[75] Wolfbeis, O. S. Probes, Sensors, and Labels: Why is Real Progress Slow? *Angew. Chem. Int. Ed.* **52**, 9864–9865 (2013).

[76] Saha, K., Agasti, S. S., Kim, C., Li, X. & Rotello, V. M. Gold Nanoparticles in Chemical and Biological Sensing. *Chem. Rev.* **112**, 2739–2779 (2012).

[77] Guerrini, L. & Graham, D. Molecularly-mediated assemblies of plasmonic nanoparticles for Surface-Enhanced Raman Spectroscopy applications. *Chem. Soc. Rev.* **41**, 7085–7107 (2012).

[78] Ghosh, S. K. & Pal, T. Interparticle Coupling Effect on the Surface Plasmon Resonance of Gold Nanoparticles: From Theory to Applications. *Chem. Rev.* **107**, 4797–4862 (2007).

[79] Abdelsalam, M. E., Mahajan, S., Bartlett, P. N., Baumberg, J. J. & Russell, A. E. SERS at Structured Palladium and Platinum Surfaces. *J. Am. Chem. Soc.* **129**, 7399–7406 (2007).

[80] Wang, X., Shi, W., She, G. & Mu, L. Surface-Enhanced Raman Scattering (SERS) on transition metal and semiconductor nanostructures. *Phys. Chem. Chem. Phys.* **14**, 5891–5901 (2012).

[81] Cecchini, M. P., Turek, V. A., Paget, J., Kornyshev, A. A. & Edel, J. B. Self-assembled nanoparticle arrays for multiphase trace analyte detection. *Nat. Mater.* **12**, 165–171 (2013).

[82] Kasera, S., Biedermann, F., Baumberg, J. J., Scherman, O. A. & Mahajan, S. Quantitative SERS Using the Sequestration of Small Molecules Inside Precise Plasmonic Nanoconstructs. *Nano Lett.* **12**, 5924–5928 (2012).

[83] Taylor, R. W. *et al.* Precise Subnanometer Plasmonic Junctions for SERS within Gold Nanoparticle Assemblies Using Cucurbit[n]uril "Glue". *ACS Nano* **5**, 3878–3887 (2011).

[84] Kundu, S. A new route for the formation of Au nanowires and application of shape-selective Au nanoparticles in SERS studies. *J. Mater. Chem. C* **1**, 831–842 (2013).

[85] Guo, S. & Wang, E. Noble metal nanomaterials: Controllable synthesis and application in fuel cells and analytical sensors. *Nano Today* **6**, 240–264 (2011).

[86] Liu, Z. *et al.* Gold mesoparticles with precisely controlled surface topographies for single-particle surface-enhanced Raman spectroscopy. *J. Mater. Chem. C* **1**, 5567–5576 (2013).

[87] Tiwari, V. S. *et al.* Non-resonance SERS effects of silver colloids with different shapes. *Chem. Phys. Lett.* **446**, 77–82 (2007).

[88] Kedia, A. & Kumar, P. S. Controlled reshaping and plasmon tuning mechanism of gold nanostars. *J. Mater. Chem. C* **1**, 4540 (2013).

[89] Lee, J. *et al.* Tailoring surface plasmons of high-density gold nanostar assemblies on metal films for surface-enhanced Raman spectroscopy. *Nanoscale* **6**, 616–623 (2014).

[90] Senthil Kumar, P., Pastoriza-Santos, I., Rodríguez-González, B., Javier García de Abajo, F. & Liz-Marzan, L. M. High-yield synthesis and optical response of gold nanostars. *Nanotechnology* **19**, 015606–015611 (2007).

[91] Peveler, W. J. & Parkin, I. P. Rapid synthesis of gold nanostructures with cyclic and linear ketones. *RSC Adv.* **3**, 21919–21927 (2013).

[92] Dasary, S. S. R. *et al.* Gold nanoparticle based surface enhanced fluorescence for detection of organophosphorus agents. *Chem. Phys. Lett.* **460**, 187–190 (2008).

[93] Jerez-Rozo, J. I., Primera-Pedrozo, O. M., Barreto-Caban, M. A. & Hernandez-Rivera, S. P. Enhanced Raman Scattering of 2,4,6-TNT Using Metallic Colloids. *IEEE Sensors J.* **8**, 974–982 (2008).

[94] Primera-Pedrozo, O. M. *et al.* Nanotechnology-Based Detection of Explosives and Biological Agents Simulants. *IEEE Sensors J.* **8**, 963–973 (2008).

[95] Xu, Z. *et al.* Surface-Enhanced Raman Scattering Spectroscopy of Explosive 2,4-Dinitroanisole using Modified Silver Nanoparticles. *Langmuir* **27**, 13773–13779 (2011).

[96] Dasary, S. S. R., Singh, A. K., Senapati, D., Yu, H. & Ray, P. C. Gold Nanoparticle Based Label-Free SERS Probe for Ultrasensitive and Selective Detection of Trinitrotoluene. *J. Am. Chem. Soc.* **131**, 13806–13812 (2009).

[97] Xu, J. Y. *et al.* SERS detection of explosive agent by macrocyclic compound functionalized triangular gold nanoprisms. *J. Raman Spectrosc.* **42**, 1728–1735 (2011).

[98] Hatab, N. A., Eres, G., Hatzinger, P. B. & Gu, B. Detection and analysis of cyclotrimethylenetrinitramine (RDX) in environmental samples by surface-enhanced Raman spectroscopy. *J. Raman Spectrosc.* **41**, 1131–1136 (2010).

[99] Brus, L. Electronic wave functions in semiconductor clusters: experiment and theory. *J. Phys. Chem.* **90**, 2555–2560 (1986).

[100] Bawendi, M. G., Steigerwald, M. L. & Brus, L. E. The Quantum-Mechanics of Larger Semiconductor Clusters (Quantum Dots). *Annu. Rev. Phys. Chem.* **41**, 477–496 (1990).

[101] Ekimov, A. I. & Onushchenko, A. A. Quantum size effect in three-dimensional microscopic semiconductor crystals. *JETP Letters* **34**, 345–348 (1981).

[102] Efros, A. L. *et al.* Band-edge exciton in quantum dots of semiconductors with a degenerate valence band: Dark and bright exciton states. *Phys. Rev. B* **54**, 4843–4856 (1996).

[103] Michalet, X. *et al.* Quantum dots for live cells, in vivo imaging, and diagnostics. *Science* **307**, 538–544 (2005).

[104] Murcia, M. J. *et al.* Facile Sonochemical Synthesis of Highly Luminescent ZnS–Shelled CdSe Quantum Dots. *Chem. Mater.* **18**, 2219–2225 (2006).

[105] Tsuzuki, T. & McCormick, P. G. Synthesis of CdS quantum dots by mechanochemical reaction. *Appl. Phys. A Mater. Sci.* **65**, 607–609 (1997).

[106] Stürzenbaum, S. R. *et al.* Biosynthesis of luminescent quantum dots in an earthworm. *Nat. Nanotechnol.* **8**, 57–60 (2013).

[107] Torchynska, T. & Vorobiev, Y. Semiconductor II-VI Quantum Dots with Interface States and Their Biomedical Applications. In *Advanced Biomedical Engineering* (InTech, Rijeka, 2011).

[108] Kim, S., Fisher, B., Eisler, H.-J. & Bawendi, M. Type-II Quantum Dots: CdTe/CdSe(Core/Shell) and CdSe/ZnTe(Core/Shell) Heterostructures. *J. Am. Chem. Soc.* **125**, 11466–11467 (2003).

[109] Williams, R. M. Introduction to Electron Transfer (2007). URL http://www.uva.nl/over-de-uva/organisatie/medewerkers/content/w/i/r.m.williams/r.m.williams.html.

[110] Freeman, R. & Willner, I. Optical molecular sensing with semiconductor quantum dots (QDs). *Chem. Soc. Rev.* **41**, 4067–4085 (2012).

[111] Algar, W. R., Stewart, M. H., Scott, A. M., Moon, W. J. & Medintz, I. L. Quantum dots as platforms for charge transfer-based biosensing: challenges and opportunities. *J. Mater. Chem. B* **2**, 7816–7827 (2014).

[112] Sun, X., Wang, Y. & Lei, Y. Fluorescence based explosive detection: from mechanisms to sensory materials. *Chem. Soc. Rev.* (2015). DOI: 10.1039/c5cs00496a.

[113] Hezinger, A. F. E., Teßmar, J. & Göpferich, A. Polymer coating of quantum dots – A powerful tool toward diagnostics and sensorics. *Eur. J. Pharm. Biopharm.* **68**, 138–152 (2008).

[114] Ganiga, M. & Cyriac, J. Detection of PETN and RDX using a FRET-based fluorescence sensor system. *Anal. Methods* **7**, 5412–5418 (2015).

[115] Zhu, H., Sikora, U. & Ozcan, A. Quantum dot enabled detection of Escherichia coli using a cell-phone. *Analyst* **137**, 2541–2544 (2012).

[116] Goldman, E. R. *et al.* Multiplexed Toxin Analysis Using Four Colors of Quantum Dot Fluororeagents. *Anal. Chem.* **76**, 684–688 (2004).

[117] Medintz, I. L. *et al.* Quantum-dot/dopamine bioconjugates function as redox coupled assemblies for in vitro and intracellular pH sensing. *Nat. Mater.* **9**, 676–684 (2010).

[118] Tomasulo, M., Yildiz, I., Kaanumalle, S. L. & Raymo, F. M. pH-Sensitive Ligand for Luminescent Quantum Dots. *Langmuir* **22**, 10284–10290 (2013).

[119] Mu, Q., Li, Y., Ma, Y. & Zhong, X. Visual detection of biological thiols based on lightening quantum dot–TiO_2 composites. *Analyst* **139**, 996–999 (2014).

[120] Tang, B. *et al.* A New Nanobiosensor for Glucose with High Sensitivity and Selectivity in Serum Based on Fluorescence Resonance Energy Transfer (FRET) between CdTe Quantum Dots and Au Nanoparticles. *Chem. Eur. J.* **14**, 3637–3644 (2008).

[121] Liu, Q. *et al.* Differentiation of cancer cell type and phenotype using quantum dot-gold nanoparticle sensor arrays. *Cancer Lett.* **334**, 196–201 (2013).

[122] Wadhavane, P. D., Izquierdo, M. A., Galindo, F., Burguete, M. I. & Luis, S. V. Organogel–quantum dots hybrid materials displaying fluorescence sensitivity and structural stability towards nitric oxide. *Soft Matter* **8**, 4373–4381 (2012).

[123] Lou, Y., Zhao, Y., Chen, J. & Zhu, J.-J. Metal ions optical sensing by semiconductor quantum dots. *J. Mater. Chem. C* **2**, 595–613 (2014).

[124] Freeman, R., Finder, T. & Willner, I. Multiplexed Analysis of Hg 2+and Ag +Ions by Nucleic Acid Functionalized CdSe/ZnS Quantum Dots and Their Use for Logic Gate Operations. *Angew. Chem. Int. Ed.* **48**, 7818–7821 (2009).

[125] Shi, G. H., Shang, Z. B., Wang, Y., Jin, W. J. & Zhang, T. C. Fluorescence quenching of CdSe quantum dots by nitroaromatic explosives and their relative compounds. *Spectrochim. Acta Mol. Biomol. Spectrosc.* **70**, 247–252 (2008).

[126] Bai, M., Huang, S., Xu, S., Hu, G. & Wang, L. Fluorescent Nanosensors via Photoinduced Polymerization of Hydrophobic Inorganic Quantum Dots for the Sensitive and Selective Detection of Nitroaromatics. *Anal. Chem.* **87**, 2383–2388 (2015).

[127] Carrillo-Carrión, C., Simonet, B. M. & Valcárcel, M. Determination of TNT explosive based on its selectively interaction with creatinine-capped CdSe/ZnS quantum dots. *Anal. Chim. Acta* **792**, 93–100 (2013).

[128] Pazhanivel, T. *et al.* Improved sensing performance from methionine capped CdTe and CdTe/ZnS quantum dots for the detection of trace amounts of explosive chemicals in liquid media. *Anal. Methods* **5**, 910–916 (2013).

[129] Singh, K., Chaudhary, G. R., Singh, S. & Mehta, S. K. Synthesis of highly luminescent water stable ZnO quantum dots as photoluminescent sensor for picric acid. *Journal of Luminescence* **154**, 148–154 (2014).

[130] Tian, X. *et al.* Hybrid Cadmium Tellurium Quantum Dots for Rapid Visualization of Trace-Level Nitroaromatic Explosives. *Anal. Lett.* **47**, 2035–2047 (2014).

[131] Wang, Y.-q. & Zou, W.-s. 3-Aminopropyltriethoxysilane-functionalized manganese doped ZnS quantum dots for room-temperature phosphorescence sensing ultratrace 2,4,6-trinitrotoluene in aqueous solution. *Talanta* **85**, 469–475 (2011).

[132] Freeman, R. & Willner, I. NAD +/NADH-Sensitive Quantum Dots: Applications To Probe NAD +-Dependent Enzymes and To Sense the RDX Explosive. *Nano Lett.* **9**, 322–326 (2009).

[133] Freeman, R., Finder, T., Bahshi, L., Gill, R. & Willner, I. Functionalized CdSe/ZnS QDs for the Detection of Nitroaromatic or RDX Explosives. *Adv. Mater.* **24**, 6416–6421 (2012).

[134] Algarra, M., Campos, B. B., Miranda, M. S. & da Silva, J. C. G. E. CdSe quantum dots capped PAMAM dendrimer nanocomposites for sensing nitroaromatic compounds. *Talanta* **83**, 1335–1340 (2011).

[135] Liu, B. *et al.* Water-Soluble Polymer Functionalized CdTe/ZnS Quantum Dots: A Facile Ratiometric Fluorescent Probe for Sensitive and Selective Detection of Nitroaromatic Explosives. *Chem. Eur. J.* **20**, 2132–2137 (2014).

[136] Schnee, V. P., Woodka, M. D. & Pinkham, D. Quantum dot material for the detection of explosive-related chemicals. In Broach, J. T. & Holloway, J. H. (eds.) *SPIE Defense, Security, and Sensing*, 83571J–1–83571J–7 (SPIE, 2012).

[137] Aguilera-Sigalat, J. *et al.* Quantum dot/cyclodextrin supramolecular systems based on efficient molecular recognition and their use for sensing. *Chem. Commun.* **48**, 2573–2575 (2012).

[138] Freeman, R., Finder, T., Bahshi, L. & Willner, I. Beta-Cyclodextrin-Modified CdSe/ZnS Quantum Dots for Sensing and Chiroselective Analysis. *Nano Lett.* **9**, 2073–2076 (2009).

[139] Qu, F. & Li, H. Selective molecular recognition of polycyclic aromatic hydrocarbons using CdTe quantum dots with cyclodextrin as supramolecular nano-sensitizers in water. *Sens. Actuator B Chem.* **135**, 499–505 (2009).

[140] Carrillo-Carrión, C., Lendl, B., Simonet, B. M. & Valcárcel, M. Calix[8]arene Coated CdSe/ZnS Quantum Dots as C_{60}-Nanosensor. *Anal. Chem.* **83**, 8093–8100 (2013).

[141] Jin, T., Fujii, F., Sakata, H., Tamura, M. & Kinjo, M. Calixarene-coated water-soluble CdSe–ZnS semiconductor quantum dots that are highly fluorescent and stable in aqueous solution. *Chem. Commun.* 2829–2831 (2005).

[142] Joshi, K. V., Joshi, B. K., Pandya, A., Sutariya, P. G. & Menon, S. K. Calixarene capped ZnS quantum dots as an optical nanoprobe for detection and determination of menadione. *Analyst* **137**, 4647–4650 (2012).

[143] Li, H., Zhang, Y., Wang, X., Xiong, D. & Bai, Y. Calixarene capped quantum dots as luminescent probes for Hg2+ ions. *Materials Letters* **61**, 1474–1477 (2007).

[144] Oszajca, M. *et al.* Supramolecular assemblies of semiconductor quantum dots and a bis(bipyridinium) derivative: luminescence quenching and aggregation phenomena. *RSC Adv.* **4**, 29847–29854 (2014).

[145] Qu, F., Zhou, X., Xu, J., Li, H. & Xie, G. Luminescence switching of CdTe quantum dots in presence of p-sulfonatocalix[4]arene to detect pesticides in aqueous solution. *Talanta* **78**, 1359–1363 (2009).

[146] Swarnkar, A., Shanker, G. S. & Nag, A. Organic-free colloidal semiconductor nanocrystals as luminescent sensors for metal ions and nitroaromatic explosives. *Chem. Commun.* **50**, 4743–4746 (2014).

[147] Faraday, M. The Bakerian Lecture: Experimental Relations of Gold (and Other Metals) to Light. *Philosophical Transactions of the Royal Society of London* **147**, 145–181 (1857).

[148] Kimling, J. *et al.* Turkevich Method for Gold Nanoparticle Synthesis Revisited. *J. Phys. Chem. B* **110**, 15700–15707 (2006).

[149] Turkevich, J., Stevenson, P. C. & Hillier, J. A study of the nucleation and growth processes in the synthesis of colloidal gold. *Discuss Faraday Soc* **11**, 55–75 (1951).

[150] Frens, G. Controlled Nucleation for the Regulation of the Particle Size in Monodisperse Gold Suspensions. *Nature* **241**, 20–22 (1973).

[151] Brust, M., Walker, M., Bethell, D., Schiffrin, D. J. & Whyman, R. Synthesis of thiol-derivatised gold nanoparticles in a two-phase liquid–liquid system. *J. Chem. Soc., Chem. Commun.* 801–802 (1994).

[152] Ojea-Jiménez, I. & Campanera, J. M. Molecular Modeling of the Reduction Mechanism in the Citrate-Mediated Synthesis of Gold Nanoparticles. *J. Phys. Chem. C* **116**, 23682–23691 (2012).

[153] Polte, J. *et al.* Mechanism of Gold Nanoparticle Formation in the Classical Citrate Synthesis Method Derived from Coupled In Situ XANES and SAXS Evaluation. *J. Am. Chem. Soc.* **132**, 1296–1301 (2013).

[154] Pong, B.-K. *et al.* New Insights on the Nanoparticle Growth Mechanism in the Citrate Reduction of Gold(III) Salt: Formation of the Au Nanowire Intermediate and Its Nonlinear Optical Properties. *J. Phys. Chem. C* **111**, 6281–6287 (2013).

[155] Xie, J., Lee, J.-Y. & Wang, D. I. C. Seedless, Surfactantless, High-Yield Synthesis of Branched Gold Nanocrystals in HEPES Buffer Solution. *Chem. Mater.* **19**, 2823–2830 (2007).

[156] Weisbecker, C. S., Merritt, M. V. & Whitesides, G. M. Molecular Self-Assembly of Aliphatic Thiols on Gold Colloids. *Langmuir* **12**, 3763–3772 (1996).

[157] Goldys, E. M. & Sobhan, M. A. Fluorescence of Colloidal Gold Nanoparticles is Controlled by the Surface Adsorbate. *Adv. Funct. Mater.* **22**, 1906–1913 (2012).

[158] Guan, G. *et al.* Convenient purification of gold clusters by co-precipitation for improved sensing of hydrogen peroxide, mercury ions and pesticides. *Chem. Commun.* **50**, 5703–5705 (2014).

[159] Udayabhaskararao, T. & Pradeep, T. New Protocols for the Synthesis of Stable Ag and Au Nanocluster Molecules. *J. Phys. Chem. Lett.* **4**, 1553–1564 (2013).

[160] Yuan, X. *et al.* Synthesis of highly fluorescent metal (Ag, Au, Pt, and Cu) nanoclusters by electrostatically induced reversible phase transfer. *ACS Nano* **5**, 8800–8808 (2011).

[161] Luo, Z. *et al.* From Aggregation-Induced Emission of Au(I)–Thiolate Complexes to Ultrabright Au(0)@Au(I)–Thiolate Core–Shell Nanoclusters. *J. Am. Chem. Soc.* **134**, 16662–16670 (2012).

[162] Enkin, N., Sharon, E., Golub, E. & Willner, I. Ag Nanocluster/DNA Hybrids: Functional Modules for the Detection of Nitroaromatic and RDX Explosives. *Nano Lett.* **14**, 4918–4922 (2014).

[163] Yang, X. *et al.* Fluorescent detection of TNT and 4-nitrophenol by BSA Au nanoclusters. *Dalton Trans.* **43**, 10057–10063 (2014).

[164] Senthamizhan, A., Celebioglu, A. & Uyar, T. Ultrafast on-site selective visual detection of TNT at sub-ppt level using fluorescent gold cluster incorporated single nanofiber. *Chem. Commun.* **51**, 5590–5593 (2015).

[165] Goulet, P. J. G. & Lennox, R. B. New Insights into Brust–Schiffrin Metal Nanoparticle Synthesis. *J. Am. Chem. Soc.* **132**, 9582–9584 (2010).

[166] Rana, S. *et al.* Array-Based Sensing of Metastatic Cells and Tissues Using Nanoparticle–Fluorescent Protein Conjugates. *ACS Nano* **6**, 8233–8240 (2012).

[167] Kundu, S. *et al.* A New Route to Obtain Shape-Controlled Gold Nanoparticles from Au(III)-β-diketonates. *Inorg. Chem.* **43**, 5489–5491 (2004).

[168] Mukherjee, S. *et al.* Green chemistry approach for the synthesis and stabilization of biocompatible gold nanoparticles and their potential applications in cancer therapy. *Nanotechnology* **23**, 455103 (2012).

[169] Shankar, S. S. *et al.* Biological synthesis of triangular gold nanoprisms. *Nat. Mater.* **3**, 482–488 (2004).

[170] Dauthal, P. & Mukhopadhyay, M. Prunus domestica Fruit Extract-Mediated Synthesis of Gold Nanoparticles and Its Catalytic Activity for 4-Nitrophenol Reduction. *Ind. Eng. Chem. Res.* **51**, 13014–13020 (2012).

[171] Sheny, D. S., Mathew, J. & Philip, D. Synthesis characterization and catalytic action of hexagonal gold nanoparticles using essential oils extracted from Anacardium occidentale. *Spectrochim. Acta Mol. Biomol. Spectrosc.* **97**, 306–310 (2012).

[172] Philip, D. Rapid green synthesis of spherical gold nanoparticles using Mangifera indica leaf. *Spectrochim. Acta Mol. Biomol. Spectrosc.* **77**, 807–810 (2010).

[173] Philip, D., Unni, C., Aromal, S. A. & Vidhu, V. K. Murraya Koenigii leaf-assisted rapid green synthesis of silver and gold nanoparticles. *Spectrochim. Acta Mol. Biomol. Spectrosc.* **78**, 899–904 (2011).

[174] Kumar, C. G., Mamidyala, S. K., Sreedhar, B. & Reddy, B. V. S. Synthesis and characterization of gold glyconanoparticles functionalized with sugars of sweet Sorghum syrup. *Biotechnol. Prog.* **27**, 1455–1463 (2011).

[175] Uppal, M. A., Kafizas, A., Ewing, M. B. & Parkin, I. P. The room temperature formation of gold nanoparticles from the reaction of cyclohexanone and auric acid; a transition from dendritic particles to compact shapes and nanoplates. *J. Mater. Chem. A* **1**, 7351–7359 (2013).

[176] Keeffe, J. R., Kresge, A. J. & Schepp, N. P. Keto-enol equilibrium constants of simple monofunctional aldehydes and ketones in aqueous solution. *J. Am. Chem. Soc.* **112**, 4862–4868 (1990).

[177] Lissel, M., Neumann, B. & Schmidt, S. Ein einfaches Verfahren zur vollständigen Methylierung der α-Positionen einiger Ketone. *Liebigs Ann. Chem.* **1987**, 263–264 (1987).

[178] Ogoshi, T. & Harada, A. Chemical Sensors Based on Cyclodextrin Derivatives. *Sensors* **8**, 4961–4982 (2008).

[179] Hawari, J., Paquet, L., Zhou, E., Halasz, A. & Zilber, B. Enhanced Recovery of the Explosive Hexahydro-1, 3, 5-Trinitro-1, 3, 5-Triazine (RDX) From Soil: cyclodextrin versus anionic surfactants. *Chemosphere* **32**, 1929–1936 (1996).

[180] Zhang, M. *et al.* Using molecular recognition of β-cyclodextrin to determine molecular weights of low-molecular-weight explosives by MALDI-TOF mass spectrometry. *J. Am. Soc. Mass. Spectrom.* **17**, 189–193 (2006).

[181] Ponnu, A. & Anslyn, E. V. A fluorescence-based cyclodextrin sensor to detect nitroaromatic explosives. *Supramolecular Chemistry* **22**, 65–71 (2010).

[182] Ponnu, A., Edwards, N. Y. & Anslyn, E. V. Pattern recognition based identification of nitrated explosives. *New J. Chem.* **32**, 848–855 (2008).

[183] Freeman, W. A., Mock, W. L. & Shih, N. Y. Cucurbituril. *J. Am. Chem. Soc.* **103**, 7367–7368 (1981).

[184] Day, A., Arnold, A. P., Blanch, R. J. & Snushall, B. Controlling factors in the synthesis of cucurbituril and its homologues. *J. Org. Chem.* **66**, 8094–8100 (2001).

[185] Kim, J. *et al.* New Cucurbituril Homologues: Syntheses, Isolation, Characterization, and X-ray Crystal Structures of Cucurbit[n]uril (n = 5, 7, and 8). *J. Am. Chem. Soc.* **122**, 540–541 (2000).

[186] Walker, S., Oun, R., McInnes, F. J. & Wheate, N. J. The Potential of Cucurbit[n]urils in Drug Delivery. *Isr. J. Chem.* **51**, 616–624 (2011).

[187] Masson, E., Ling, X., Joseph, R., Kyeremeh-Mensah, L. & Lu, X. Cucurbituril chemistry: a tale of supramolecular success. *RSC Adv.* **2**, 1213 (2012).

[188] Burnett, C. A. *et al.* Preparation of glycoluril monomers for expanded cucurbit[n]uril synthesis. *Tetrahedron* **59**, 1961–1970 (2003).

[189] Vinciguerra, B. *et al.* Synthesis and Self-Assembly Processes of Monofunctionalized Cucurbit[7]uril. *J. Am. Chem. Soc.* **134**, 13133–13140 (2012).

[190] Lucas, D. *et al.* Templated Synthesis of Glycoluril Hexamer and Monofunctionalized Cucurbit[6]uril Derivatives. *J. Am. Chem. Soc.* **133**, 17966–17976 (2011).

[191] Cao, L. & Isaacs, L. Daisy Chain Assembly Formed from a Cucurbit[6]uril Derivative. *Org. Lett.* **14**, 3072–3075 (2012).

[192] Jon, S. Y. *et al.* Facile Synthesis of Cucurbit[n]uril Derivatives via Direct Functionalization: Expanding Utilization of Cucurbit[n]uril. *J. Am. Chem. Soc.* **125**, 10186–10187 (2003).

[193] Zhao, N., Lloyd, G. O. & Scherman, O. A. Monofunctionalised cucurbit[6]uril synthesis using imidazolium host-guest complexation. *Chem. Commun.* **48**, 3070–3072 (2012).

[194] Kim, K. *et al.* Functionalized cucurbiturils and their applications. *Chem. Soc. Rev.* **36**, 267–279 (2007).

[195] Cui, S.-C., Tachikawa, T., Fujitsuka, M. & Majima, T. Photoinduced Electron Transfer in a Quantum Dot-Cucurbituril Supramolecular Complex. *J. Phys. Chem. C* **115**, 1824–1830 (2011).

[196] Zhu, W. *et al.* A new strategy for selective detection of nitrated explosives based on a confinement effect of nanocavity. *J. Mater. Chem. A* **1**, 11741–11747 (2013).

[197] Zhu, W. *et al.* CB[8]-based rotaxane as a useful platform for sensitive detection and discrimination of explosives. *Chem. Sci.* **4**, 3583–3590 (2013).

[198] Jin, T., Fujii, F., Sakata, H., Tamura, M. & Kinjo, M. Amphiphilic p-sulfonatocalix[4]arene-coated CdSe/ZnS quantum dots for the optical detection of the neurotransmitter acetylcholine. *Chem. Commun.* 4300–4302 (2005).

[199] Wang, X., Wu, J., Li, F. & Li, H. Synthesis of water-soluble CdSe quantum dots by ligand exchange with p-sulfonatocalix(n)arene (n = 4, 6) as fluorescent probes for amino acids. *Nanotechnology* **19**, 205501–205508 (2008).

[200] Lee, Y. H. *et al.* Dipyrenylcalix[4]arene—A Fluorescence-Based Chemosensor for Trinitroaromatic Explosives. *Chem. Eur. J.* **16**, 5895–5901 (2010).

[201] Del Valle, E. M. M. Cyclodextrins and their uses: a review. *Process Biochemistry* **39**, 1033–1046 (2004).

[202] Lee, J. W., Samal, S., Selvapalam, N., Kim, H.-J. & Kim, K. Cucurbituril Homologues and Derivatives: New Opportunities in Supramolecular Chemistry. *Acc. Chem. Res.* **36**, 621–630 (2003).

[203] Gutsche, C. D. In Stoddart, J. F. (ed.) *Calixarenes*, Monographs in Supramolecular Chemistry (Royal Society of Chemistry, 1989).

[204] Susumu, K. *et al.* Enhancing the Stability and Biological Functionalities of Quantum Dots via Compact Multifunctional Ligands. *J. Am. Chem. Soc.* **129**, 13987–13996 (2007).

[205] Mei, B. C. *et al.* Modular poly(ethylene glycol) ligands for biocompatible semiconductor and gold nanocrystals with extended pH and ionic stability. *J. Mater. Chem.* **18**, 4949–4958 (2008).

[206] Susumu, K., Mei, B. C. & Mattoussi, H. Multifunctional ligands based on dihydrolipoic acid and polyethylene glycol to promote biocompatibility of quantum dots. *Nat. Protoc.* **4**, 424–436 (2009).

[207] Palui, G. *et al.* Photoinduced Phase Transfer of Luminescent Quantum Dots to Polar and Aqueous Media. *J. Am. Chem. Soc.* **134**, 16370–16378 (2012).

[208] Chetcuti, M. J. *et al.* Synthesis of mono-, di- and tetra-alkyne functionalized calix[4]arenes: Reactions of these multipodal ligands with dicobalt octacarbonyl to give complexes which contain up to eight cobalt atoms. *Dalton Trans.* 2999–3008 (2009).

[209] Groenen, L. C. *et al.* Synthesis of monoalkylated calix[4]arenes via direct alkylation. *Tetrahedron* **47**, 8379–8384 (1991).

[210] Faiz, J. A., Spencer, N. & Pikramenou, Z. Acetylenic cyclodextrins for multireceptor architectures: cups with sticky ends for the formation of extension wires and junctions. *Org. Biomol. Chem.* **3**, 4239–4245 (2005).

[211] Byun, H.-S., Zhong, N. & Bittman, R. 6-O-*p*-Toluenesulfonyl-beta-Cyclodextrin. *Org. Synth.* **77**, 225 (2000).

[212] Lolya, D. *et al.* Protolytic cleavage of derivatives of 2,5-dimethoxy-2,5-dihydrofuran. *Chem. Heterocycl. Compd.* **33**, 164–170 (1997).

[213] Jiao, D. & Scherman, O. A. Isolation of cucurbit[n]uril homologues with imidazolium salts in a recyclable manner. *Green Chemistry* **14**, 2445–2449 (2012).

[214] Dethlefsen, J. R. & Døssing, A. Preparation of a ZnS Shell on CdSe Quantum Dots Using a Single-Molecular ZnS Precursor. *Nano Lett.* **11**, 1964–1969 (2011).

[215] Bear, J. C. *et al.* Copper-Doped CdSe/ZnS Quantum Dots: Controllable Photoactivated Copper(I) Cation Storage and Release Vectors for Catalysis. *Angew. Chem. Int. Ed.* **53**, 1598–1601 (2013).

[216] Lipshutz, B. H. & Taft, B. R. Heterogeneous Copper-in-Charcoal-Catalyzed Click Chemistry. *Angew. Chem. Int. Ed.* **45**, 8235–8238 (2006).

[217] Zhan, N. *et al.* Combining ligand design with photoligation to provide compact, colloidally stable, and easy to conjugate quantum dots. *ACS Appl. Mater. Interfaces* **5**, 2861–2869 (2013).

[218] Aldeek, F. *et al.* UV and Sunlight Driven Photoligation of Quantum Dots: Understanding the Photochemical Transformation of the Ligands. *J. Am. Chem. Soc.* **137**, 2704–2714 (2015).

[219] Zhan, N., Palui, G., Merkl, J.-P. & Mattoussi, H. Quantifying the density of surface capping ligands on semiconductor quantum dots. In Parak, W. J., Osinski, M. & Liang, X.-J. (eds.) *Colloidal Nanoparticles for Biomedical Applications X*, 93381A–93381A–11 (2015).

[220] van Sark, W. G. J. H. M., Frederix, P. L. T. M., Bol, A. A., Gerritsen, H. C. & Meijerink, A. Blueing, Bleaching, and Blinking of Single CdSe/ZnS Quantum Dots. *ChemPhysChem* **3**, 871–879 (2002).

[221] van Driel, A. F. *et al.* Statistical analysis of time-resolved emission from ensembles of semiconductor quantum dots: Interpretation of exponential decay models. *Phys. Rev. B* **75**, 035329 (2007).

[222] Jeong, S. *et al.* Effect of the Thiol–Thiolate Equilibrium on the Photophysical Properties of Aqueous CdSe/ZnS Nanocrystal Quantum Dots. *J. Am. Chem. Soc.* **127**, 10126–10127 (2005).

[223] Sanchez, J. C., DiPasquale, A. G., Rheingold, A. L. & Trogler, W. C. Synthesis, Luminescence Properties, and Explosives Sensing with 1,1-Tetraphenylsilole- and 1,1-Silafluorene-vinylene Polymers. *Chem. Mater.* **19**, 6459–6470 (2007).

[224] Qasim, M. *et al.* Application of quantum-chemical approximations to environmental problems: Prediction of physical and chemical properties of TNT and related species. *Chemosphere* **69**, 1144–1150 (2007).

[225] Jasieniak, J., Califano, M. & Watkins, S. E. Size-Dependent Valence and Conduction Band-Edge Energies of Semiconductor Nanocrystals. *ACS Nano* **5**, 5888–5902 (2011).

[226] Tvrdy, K., Frantsuzov, P. A. & Kamat, P. V. Photoinduced electron transfer from semiconductor quantum dots to metal oxide nanoparticles. *Proc. Natl. Acad. Sci. U.S.A.* **108**, 29–34 (2011).

[227] Lavigne, J. J. & Anslyn, E. V. Sensing A Paradigm Shift in the Field of Molecular Recognition: From Selective to Differential Receptors. *Angew. Chem. Int. Ed.* **40**, 3118–3130 (2001).

[228] Lichtenstein, A. *et al.* Supersensitive fingerprinting of explosives by chemically modified nanosensors arrays. *Nat. Commun.* **5** (2014).

[229] Berliner, A. *et al.* A patterned colorimetric sensor array for rapid detection of TNT at ppt level. *RSC Adv.* **4**, 10672–10675 (2014).

[230] Askim, J. R., Mahmoudi, M. & Suslick, K. S. Optical sensor arrays for chemical sensing: the optoelectronic nose. *Chem. Soc. Rev.* **42**, 8649–8682 (2013).

[231] Hughes, A. D., Glenn, I. C., Patrick, A. D., Ellington, A. & Anslyn, E. V. A pattern recognition based fluorescence quenching assay for the detection and identification of nitrated explosive analytes. *Chem. Eur. J.* **14**, 1822–1827 (2008).

[232] Ivy, M. A., Gallagher, L. T., Ellington, A. D. & Anslyn, E. V. Exploration of plasticizer and plastic explosive detection and differentiation with serum albumin cross-reactive arrays. *Chem. Sci.* **3**, 1773–1779 (2012).

[233] Zhu, W. *et al.* A Rapid and Efficient Way to Dynamic Creation of Cross-Reactive Sensor Arrays Based on Ionic Liquids. *Chem. Eur. J.* **19**, 11603–11612 (2013).

[234] Latendresse, C. A., Fernandes, S. C., You, S., Zhang, H. Q. & Euler, W. B. A fluorometric sensing array for the detection of military explosives and IED materials. *Anal. Methods* **5**, 5457–5463 (2013).

[235] Diehl, K. L. & Anslyn, E. V. Array sensing using optical methods for detection of chemical and biological hazards. *Chem. Soc. Rev.* **42**, 8596–8611 (2013).

[236] Bajaj, A. *et al.* Detection and differentiation of normal, cancerous, and metastatic cells using nanoparticle-polymer sensor arrays. *Proc. Natl. Acad. Sci. U.S.A.* **106**, 10912–10916 (2009).

[237] Elci, S. G. *et al.* Recognition of glycosaminoglycan chemical patterns using an unbiased sensor array. *Chem. Sci.* **4**, 2076–2080 (2013).

[238] Petryayeva, E. & Algar, W. R. Multiplexed Homogeneous Assays of Proteolytic Activity Using a Smartphone and Quantum Dots. *Anal. Chem.* **86**, 3195–3202 (2014).

[239] Rao, C. R. The Utilization of Multiple Measurements in Problems of Biological Classification. *J. R. Stat. Soc. Ser. B Stat. Methodol.* **10**, 159–203 (1948).

[240] Martinez, A. M. & Kak, A. C. PCA versus LDA. *TPAMI* **23**, 228–233 (2001).

[241] Boser, B. E., Guyon, I. M. & Vapnik, V. A training algorithm for optimum margin classifiers. In *Proceedings of the fifth annual workshop on computational learning theory* (ACM, 1992).

[242] Hsu, C.-W. & Lin, C.-J. A comparison of methods for multiclass support vector machines. *Neural Networks, IEEE Transactions on* **13**, 415–425 (2002).

[243] Gokcen, I. & Peng, J. Comparing Linear Discriminant Analysis and Support Vector Machines. In Yakhno, T. (ed.) *Lecture Notes in Computer Science*, 104–113 (Springer Berlin Heidelberg, Berlin, Heidelberg, 2002).

[244] Armbruster, D. A. & Pry, T. Limit of blank, limit of detection and limit of quantitation. *Clin Biochem Rev* **29 Suppl 1**, S49–52 (2008).

[245] El-Manzalawy, Y. & Honavar, V. WLSVM: Integrating libsvm into WEKA environment (2005). URL `https://weka.wikispaces.com/LibSVM`. Accessed: Jun 2015.

[246] Chang, C.-C. & Lin, C.-J. LIBSVM: A library for support vector machines. *ACM Transactions on Intelligent Systems and Technology* **2**, 27:1–27:27 (2011).

[247] Cahill, S. & Bulusu, S. Molecular complexes of explosives with cyclodextrins I. Characterization of complexes with the nitramines RDX, HMX and TNAZ in solution by 1H NMR spin-lattice relaxation time measurements. *Mag. Reson. Chem.* **31**, 731–735 (1993).

[248] Takeuchi, H., Omogo, B. & Heyes, C. D. Are Bidentate Ligands Really Better than Monodentate Ligands For Nanoparticles? *Nano Lett.* **13**, 4746–4752 (2013).

[249] Afzaal, M., Malik, M. A. & O'Brien, P. Preparation of zinc containing materials. *New J. Chem.* **31**, 2029–2040 (2007).

[250] Wei, Q. *et al.* Fluorescent imaging of single nanoparticles and viruses on a smart phone. *ACS Nano* **7**, 9147–9155 (2013).

[251] Oh, J.-W. *et al.* Biomimetic virus-based colourimetric sensors. *Nat. Commun.* **5**, 3043 (2014).

[252] Berg, B. *et al.* Cellphone-Based Hand-Held Microplate Reader for Point-of-Care Testing of Enzyme-Linked Immunosorbent Assays. *ACS Nano* **9**, 7857–7866 (2015).

[253] Feng, L., Musto, C. J. & Suslick, K. S. A Simple and Highly Sensitive Colorimetric Detection Method for Gaseous Formaldehyde. *J. Am. Chem. Soc.* **132**, 4046–4047 (2010).

[254] Lim, S. H., Feng, L., Kemling, J. W., Musto, C. J. & Suslick, K. S. An optoelectronic nose for the detection of toxic gases. *Nat. Chem.* **1**, 562–567 (2009).

[255] Lin, H. & Suslick, K. S. A Colorimetric Sensor Array for Detection of Triacetone Triperoxide Vapor. *J. Am. Chem. Soc.* **132**, 15519–15521 (2010).

[256] Rakow, N. A. & Suslick, K. S. A colorimetric sensor array for odour visualization. *Nature* **406**, 710–713 (2000).

[257] Lonsdale, C. L. *et al.* The Use of Colorimetric Sensor Arrays to Discriminate between Pathogenic Bacteria. *PLoS ONE* **8**, e62726 (2013).

[258] Salles, M. O., Meloni, G. N., de Araujo, W. R. & Paixão, T. R. L. C. Explosive colorimetric discrimination using a smartphone, paper device and chemometrical approach. *Anal. Methods* **6**, 2047–2052 (2014).

[259] Kim, Y., Jeon, J. B. & Chang, J. Y. CdSe quantum dot-encapsulated molecularly imprinted mesoporous silica particles for fluorescent sensing of bisphenol A. *J. Mater. Chem.* **22**, 24075–24080 (2012).

[260] Nguyen, T.-D., Hamad, W. Y. & MacLachlan, M. J. CdS Quantum Dots Encapsulated in Chiral Nematic Mesoporous Silica: New Iridescent and Luminescent Materials. *Adv. Funct. Mater.* **24**, 777–783 (2014).

[261] Salinas, Y. *et al.* Chromo-Fluorogenic Detection of Nitroaromatic Explosives by Using Silica Mesoporous Supports Gated with Tetrathiafulvalene Derivatives. *Chem. Eur. J.* **20**, 855–866 (2013).

[262] Wadhavane, P. D. *et al.* Photoluminescence Enhancement of CdSe Quantum Dots: A Case of Organogel–Nanoparticle Symbiosis. *J. Am. Chem. Soc.* **134**, 20554–20563 (2012).

[263] Trickett, K. *et al.* Microemulsion-based organogels containing inorganic nanoparticles. *Soft Matter* **6**, 1291–1296 (2010).

[264] Le Renard, P.-E. *et al.* The in vivo performance of magnetic particle-loaded injectable, in situ gelling, carriers for the delivery of local hyperthermia. *Biomaterials* **31**, 691–705 (2010).

[265] Taboada, E. *et al.* Nanocomposites combining conducting and superparamagnetic components prepared via an organogel. *Soft Matter* **7**, 2755–2761 (2011).

[266] Samanta, S. K., Pal, A., Bhattacharya, S. & Rao, C. N. R. Carbon nanotube reinforced supramolecular gels with electrically conducting, viscoelastic and near-infrared sensitive properties. *J. Mater. Chem.* **20**, 6881–6890 (2010).

[267] Vidyasagar, A., Handore, K. & Sureshan, K. M. Soft Optical Devices from Self-Healing Gels Formed by Oil and Sugar-Based Organogelators. *Angew. Chem. Int. Ed.* **50**, 8021–8024 (2011).

[268] Prathap, A. & Sureshan, K. M. A mannitol based phase selective supergelator offers a simple, viable and greener method to combat marine oil spills. *Chem. Commun.* **48**, 5250–5252 (2012).

[269] Peveler, W. J., Bear, J. C., Southern, P. & Parkin, I. P. Organic–inorganic hybrid materials: nanoparticle containing organogels with myriad applications. *Chem. Commun.* **50**, 14418–14420 (2014).

[270] Cametti, M. & Džolić, Z. New frontiers in hybrid materials: noble metal nanoparticles - supramolecular gel systems. *Chem. Commun.* **50**, 8273–8286 (2014).

[271] Buck, M. R., Biacchi, A. J. & Schaak, R. E. Insights into the Thermal Decomposition of Co(II) Oleate for the Shape-Controlled Synthesis of Wurtzite-Type CoO Nanocrystals. *Chem. Mater.* **26**, 1492–1499 (2014).

[272] Crick, C. R., Bear, J. C., Southern, P. & Parkin, I. P. A general method for the incorporation of nanoparticles into superhydrophobic films by aerosol assisted chemical vapour deposition. *J. Mater. Chem. A* **1**, 4336 (2013).

[273] Li, P.-Z., Aijaz, A. & Xu, Q. Highly Dispersed Surfactant-Free Nickel Nanoparticles and Their Remarkable Catalytic Activity in the Hydrolysis of Ammonia Borane for Hydrogen Generation. *Angew. Chem. Int. Ed.* **51**, 6753–6756 (2012).

[274] Colchester, R. J. *et al.* Laser-generated ultrasound with optical fibres using functionalised carbon nanotube composite coatings. *Appl. Phys. Lett.* **104**, 173502 (2014).

[275] Uyeda, H. T., Medintz, I. L., Jaiswal, J. K., Simon, S. M. & Mattoussi, H. Synthesis of Compact Multidentate Ligands to Prepare Stable Hydrophilic Quantum Dot Fluorophores. *J. Am. Chem. Soc.* **127**, 3870–3878 (2005).

[276] Bonina, F. *et al.* Glycosyl Derivatives of Dopamine and l-dopa as Anti-Parkinson Prodrugs: Synthesis, Pharmacological Activity and In Vitro Stability Studies. *J. Drug Target.* **11**, 25–36 (2003).

[277] Peng, Z. A. & Peng, X. Formation of High-Quality CdTe, CdSe, and CdS Nanocrystals Using CdO as Precursor. *J. Am. Chem. Soc.* **123**, 183–184 (2001).

[278] Xu, S., Kumar, S. & Nann, T. Rapid Synthesis of High-Quality InP Nanocrystals. *J. Am. Chem. Soc.* **128**, 1054–1055 (2006).

[279] Lee, P. C. & Meisel, D. Adsorption and surface-enhanced Raman of dyes on silver and gold sols. *J. Phys. Chem.* **86**, 3391–3395 (1982).

[280] Bear, J. C. *et al.* Nanoparticle-sulphur "inverse vulcanisation" polymer composites. *Chem. Commun.* **51**, 10467–10470 (2015).

[281] Crick, C. R. *et al.* Advanced analysis of nanoparticle composites - a means toward increasing the efficiency of functional materials. *RSC Adv.* **5**, 53789–53795 (2015).

[282] Bovis, M. J. *et al.* Photosensitisation studies of silicone polymer doped with methylene blue and nanogold for antimicrobial applications. *RSC Adv.* **5**, 54830–54842 (2015).

[283] Sehmi, S. K. *et al.* Lethal photosensitisation of Staphylococcus aureus and Escherichia coli using crystal violet and zinc oxide-encapsulated polyurethane. *J. Mater. Chem. B* **3**, 6490–6500 (2015).

[284] Kresse, G. & Hafner, J. Ab initio molecular dynamics for liquid metals. *Phys. Rev. B* **47**, 558 (1993).

[285] Kresse, G. & Furthmüller, J. Efficiency of ab-initio total energy calculations for metals and semiconductors using a plane-wave basis set. *Comput. Mat. Sci.* **6**, 15 (1996).

[286] Csonka, G. I. *et al.* Assessing the performance of recent density functionals for bulk solids. *Phys. Rev. B* **79**, 155107 (2009).

[287] Mermin, N. D. Thermal properties of the inhomogeneous electron gas. *Physical Review* **137**, A1441–A1443 (1965).

[288] Monkhorst, H. J. & Pack, J. D. Special Points for Brillouin-Zone Integrations. *Phys. Rev. B* **13**, 5188–5192 (1976).

[289] Xu, Y.-N. & Ching, W. Y. Electronic, optical, and structural properties of some wurtzite crystals. *Phys. Rev. B* **48**, 4335–4351 (1993).

[290] Henkelman, G., Arnaldsson, A. & Jonsson, H. A fast and robust algorithm for Bader decomposition of charge density. *Comput. Mater. Sci.* **36**, 354–360 (2006).

[291] Moreira, I. D. R., Illas, F. & Martin, R. L. Effect of Fock exchange on the electronic structure and magnetic coupling in NiO. *Phys. Rev. B* **65**, 155102 (2002).

[292] Anisimov, V. I., Korotin, M. A., Zaanen, J. & Andersen, O. K. Spin Bags, Polarons, and Impurity Potentials in $La_{2-x}Sr_xCuO_4$ from First Principles. *Phys. Rev. Lett.* **68**, 345–348 (1992).

[293] Dudarev, S. L., Botton, G. A., Savrasov, S. Y., Humphreys, C. J. & Sutton, A. P. Electron-energy-loss spectra and the structural stability of nickel oxide: An LSDA+U study. *Phys. Rev. B* **57**, 1505–1509 (1998).

[294] Heyd, J., Scuseria, G. E. & Ernzerhof, M. Hybrid functionals based on a screened Coulomb potential. *J. Chem. Phys.* **118**, 8207–8215 (2003).

[295] Heyd, J., Scuseria, G. E. & Ernzerhof, M. Erratum: "Hybrid functionals based on a screened Coulomb potential" [J. Chem. Phys. 118, 8207 (2003)]. *J. Chem. Phys.* **124**, 219906 (2006).

[296] Krukau, A. V., Vydrov, O. A., Izmaylov, A. F. & Scuseria, G. E. Influence of the exchange screening parameter on the performance of screened hybrid functionals. *J. Chem. Phys.* **125**, 224106 (2006).

[297] Henderson, T. M., Paier, J. & Scuseria, G. E. Accurate treatment of solids with the HSE screened hybrid. *Phys. Status Solidi B* **248**, 767–774 (2011).

[298] Perdew, J. P., Burke, K. & Ernzerhof, M. Generalized Gradient Approximation Made Simple. *Phys. Rev. Lett.* **77**, 3865–3868 (1996).

[299] Perdew, J. P., Burke, K. & Ernzerhof, M. Generalized Gradient Approximation Made Simple [Phys. Rev. Lett. 77, 3865 (1996)]. *Phys. Rev. Lett.* **78**, 1396–1396 (1997).

[300] Perdew, J. P., Ernzerhof, M. & Burke, K. Rationale for mixing exact exchange with density functional approximations. *J. Chem. Phys.* **105**, 9982–9985 (1996).

[301] Watson, G. W., Kelsey, E. T., deLeeuw, N. H., Harris, D. J. & Parker, S. C. Atomistic simulation of dislocations, surfaces and interfaces in MgO. *J. Chem. Soc., Faraday Transactions* **92**, 433–438 (1996).

[302] Tasker, P. W. Stability of Ionic-Crystal Surfaces. *J. Phys. C Solid State* **12**, 4977–4984 (1979).

A

PUBLISHED PAPERS

The work in this thesis, and additional related work not discussed, has been published in several peer reviewed papers:

- Peveler, W. J., Binions, R., Hailes, S. M. V. & Parkin, I. P. Detection of explosive markers using zeolite modified gas sensors. *J. Mater. Chem. A* **1**, 2613–2620 (2013).
- Peveler, W. J. & Parkin, I. P. Rapid synthesis of gold nanostructures with cyclic and linear ketones. *RSC Adv.* **3**, 21919–21927 (2013).
- Peveler, W. J., Bear, J. C., Southern, P. & Parkin, I. P. Organic–inorganic hybrid materials: nanoparticle containing organogels with myriad applications. *Chem. Commun.* **50**, 14418–14420 (2014).
- Jurcic, M. *et al.* The vapour phase detection of explosive markers and derivatives using two fluorescent metal–organic frameworks. *J. Mater. Chem. A* **3**, 6351–6359 (2015).
- Bear, J. C. *et al.* Nanoparticle-sulphur "inverse vulcanisation" polymer composites. *Chem. Commun.* **51**, 10467–10470 (2015).
- Crick, C. R. *et al.* Advanced analysis of nanoparticle composites - a means toward increasing the efficiency of functional materials. *RSC Adv.* **5**, 53789–53795 (2015).
- Bovis, M. J. *et al.* Photosensitisation studies of silicone polymer doped with methylene blue and nanogold for antimicrobial applications. *RSC Adv.* **5**, 54830–54842 (2015).
- Sehmi, S. K. *et al.* Lethal photosensitisation of Staphylococcus aureus and Escherichia coli using crystal violet and zinc oxide-encapsulated polyurethane. *J. Mater. Chem. B* **3**, 6490–6500 (2015).

B

COMPUTATIONAL DETAILS

Computation was performed by Dr Alberto Roldan, using the ARCHER computing facility.

ZnS systems were studied using density functional methods as implemented in the Vienna *Ab-initio* Software Package.[284, 285] The ion-electron interactions were represented by the projector-augmented wave (PAW) method and the exchange-correlation by the generalized gradient approximation (GGA) with the Perdew-Burke-Ernzerhof revised for solids (PBEsol).[286] The spin was found to be negligible. The Kohn-Sham valence states were expanded in a plane-waves basis set with a cut off at 500 eV for the kinetic energy.[287] This high value for the cut off energy ensured that no Pulay stresses occurred within the cell during relaxations.

The wurtzite ZnS bulk structure was described by a Monkhorst-Pack 13x13x13 grid,[288] and optimised in the conjugate-gradient algorithm framework. It was considered converged when the force on each ion dropped below 0.01 eV/Å and the energy threshold defining self-consistency of the electron density was set to 10^{-5} eV. In order to improve the convergence of the Brillouin-zone integrations, the partial occupancies were determined using the tetrahedron method with Blöchl corrections, with a set smearing width for all calculations of 0.1 eV. The optimised lattice parameter are within 0.02 Å variation of the experimental values for ZnS[289](Table B.1).

Accuracy was increased up to 10^{-7} eV for the self-consistency electron density convergence within an accurate regime to derive the electronic characteristics such as band gap (E_g) and atomic charges (q) as integrated over the Bader volume of the atom in question as implemented in the Henkelman algorithm.[290] Despite of this, we used more computationally demanding hybrid functionals to improve the electronic structure characterisation (k-points = 3x3x3), where standard local-density approximation and GGA (generalised gradient approximation) functionals fail[291] and the Hubbard

approximation does not make a significant improvement on Mott insulator materials.[292, 293] Therefore Heyd-Scuseria-Ernzerhof (HSE06) was employed, [294–296] which provides electronic structures of better quality than semilocal functionals.[297] HSE06 is made from the Perdew-Burke-Ernzerhof functional (PBE) exchange,[298, 299] and correlation components mixed with 25% of short-range Hartree-Fock (HF) exchange.[296] The Coulomb potential exchange is replaced by a screened potential (with screening parameter ω = 0.207 $Å^{-1}$) in order to define the separation between the short- and long-range components of the HF exchange.[296] While the amount of short-range HF is a constant determined by perturbation theory, making HSE06 an adiabatic connection functional in this part of the potential,[300] its screening parameter is a reasonable system-averaged value across a wide variety of systems, giving better agreement with experiments in the case of semiconductors than for metals or insulators.[297]

Table B.1: *Summary of computed bulk material properties*

	a /Å	a/c	E_g/eV	E_g(HSE06)/eV
PBESol	3.80	1.63	2.18	2.22

The *p(2×2)* (110) surfaces were prepared by cutting the bulk structures using the METADISE code[301] and creating slab models. This code provides the different stacking of atomic layers resulting in a null dipole moment perpendicular to the surface plane.[302] The thickness of the slab and perpendicular vacuum, were tested to provide a reliable model. A total of eight atomic layers is enough to obtain bulk behaviour in the centre of the slab, nevertheless we kept the bulk structure frozen at the base. Energy convergence was obtained when the two uppermost layers were relaxed until each ion force dropped below 0.03 eV/Å, and further layer relaxation leads to energy changes below 1 meV. A vacuum width of 14 Å is large enough to avoid perpendicular interaction. All surface calculations were carried out described with a k-points grid of 3x3x1 and same electron density self-consistency convergence as the bulk calculations. Isolated adsorbent molecules were placed in the centre of a 20x21x22 $Å^3$ simulation cell, avoiding lateral interactions and using the same criteria of convergence as for the surface slabs.

This document was typeset using the `classicthesis` package developed by André Miede in LaTeX. The style was inspired by Robert Bringhurst's seminal book on typography *"The Elements of Typographic Style"*.

`http://code.google.com/p/classicthesis/`

Hermann Zapf's *Palatino* (10 pt) and *Euler* type faces (Type 1 PostScript fonts *URW Palladio L* and *FPL*) are used for the main text. Figures and schemes additionally use Monotype's *Arial*.

Spelling mistakes were painstakingly located by Gemma Beale, but any remaining spelling, grammatical or typographic errors are my own fault.

" . . . it's good for the soul"

— MCG